Statement of Disclaimer

Senior Project Final Design Report:
Magnetic Bearing for Bently Nevada RK4 Rotor Kits

Sponsor: Dr. Julia Wu

Design By:
Sean Fowler
sefowler@calpoly.edu

Garrett Olson
golson@calpoly.edu

Table of Contents

ATTENTION READER:

Since you are reading this, you are likely the inheritor of the hardware associated with this senior project. As such, it is paramount that you understand the following for your own safety:

1. This magnetic bearing system is not a trivial piece of equipment. It uses high voltage, high current electronics, which have the potential to expose the user to deadly electric shock if the device is misused.
2. Never operate the device without first reading and understanding the full operating procedures of this report.
3. All electrical components and wires must be physically avoided during operation. When adjusting electrical components outside of the lockable black box, all input signals must be turned off and the power supply plug disconnected. After this is done, energy must also be allowed to leave the system; there is about a 30 second delay that must be waited between when the input signal is set to zero and the output control current in the actuator coils also falls to zero. This current should always be monitored during use.
4. The lockable black box should remain locked at all times to prevent accidental exposure to electric shock and remind users of the danger.
5. When opening the lockable black box, the system should always be powered down and unplugged with the one exception being when adjusting the servo drive potentiometers or switches. A minimum of **one hour** must be waited after disconnecting the power supply and turning off input signals before opening the box. This is to allow the large blue capacitor to fully discharge. (4RC = time for full capacitor discharge. A 30 kOhm bleed resistor across the power supply rectifier = R. The capacitance is 0.024 F. 4 x 30,000 x 0.024 = 2,880 sec = 48 mins for full discharge. Rounded up to one hour for safety.) When adjusting servo drive potentiometers and switches, great care must be taken so as not to expose oneself to electric shock by bumping any other components in the box.
6. The rotor kit motor is capable of rotating the shaft at 10,000 RPM. At this speed, debris or untightened screws can result in serious user injury, particularly to unprotected eyes.
7. While safety measures have been put into place, we do not pretend to have created a foolproof device by any means. As such, great care, forethought, and critical awareness are vital to operating the device safely and effectively.

These are the most crucial safety precautions that must be taken when operating the device. Please consider this section as a stern warning of the unique dangers associated with this project.

1. Introduction

Active Magnetic Bearings (AMB) are contact free bearings that support loads by magnetic levitation. This is accomplished by generating magnetic forces with electric current through a series of electromagnets surrounding a suspended rotor mass. Along with a set of electromagnets, an AMB assembly also consists of power amplifiers for each electromagnet, a controller, and proximity sensors. The proximity sensors provide rotor position feedback to the control system, which modulates power to the amplifiers [4].

Magnetic bearings are used in several industrial applications today, including but not limited to compressors, turbines, pumps, motors, and generators. Advantages of their utility include very low to no friction, longer life than bearings with lubrication (no wear), high operation speeds, environmental friendliness (oil and contamination free), and the ability to accommodate irregularities in the mass distribution automatically. Disadvantages include complexity, little to no damping, difficulty to control, and high cost. Magnetic bearings are finding increasing use as the technology progresses and components becomes less expensive.
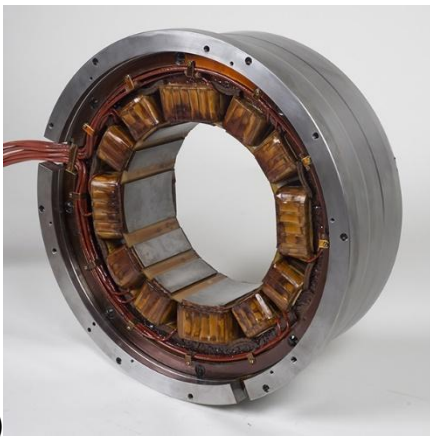
(a)   (b)

Figure 1.1. (a) Industrial full-size radial magnetic bearing. (b) SKF AMB assembly in an industrial water pump.

2. Objective

For the purpose of this project, an AMB was to be sized and retrofitted to a Bently Nevada RK4 rotor kit used in the vibrations and mechanical controls labs. These kits are used for undergraduate and graduate courses as teaching and research tools in the areas of rotor-dynamics and active machine control. The production of this AMB is the first step in a conceived series of projects that will look to continue to improve the efficiency, size, and performance of this technology. A number of companies and research labs also stand to

benefit from such a product, as SKF is currently the only company which sells magnetic bearings compatible with the rotor kits.

The specific goal of this senior project was to manufacture one magnetic bearing and integrate it with the necessary electronics hardware so that it would be capable of sending and receiving control data to and from MATLAB. The system was to be designed for future use by students as a teaching and research aid. This complements the Cal Poly Engineering Department's creed of "Learn by Doing" and will provide students with the opportunity to learn unique skills in the fields of mechatronics, rotor dynamics, and controls.

3. Background

There have been a few universities and independent parties that have successfully designed and manufactured a small scale AMB, however the technology is still relatively new with much room for improvement. University of Patras, Greece [1] designed an AMB for the same model rotor kit (the RK4) as used at Cal Poly (Figure 3.1). The bearing controller utilizes the PID control method, implemented using MATLAB software. This method provides good robustness and stability as long as the operating point is inside the linear performance range of the AMB. PID control requires linearization, therefore the non-linear equations of motion of the rotor were linearized with coupled x-y equations of motion. PID gains were derived through numerous simulations and the resulting control resulted in satisfactory damping and stiffness of the overall system. The rotor itself was modeled as rigid with one mass balance plane located near the AMB housing.
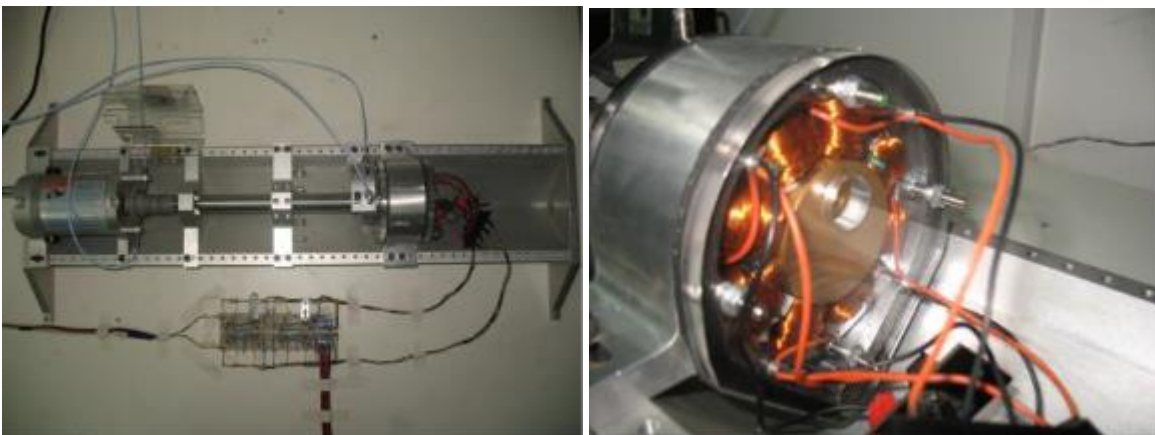
Figure 3.1. AMB designed by the Machine Design Laboratory of the Department of Mechanical Engineering and Aeronautics, University of Patras, Greece.

An independent group from the Republic of Korea [3] provides a successful roadmap for the analysis and design phases of the AMB. The "probable flux paths method" is introduced,

offering fundamental insight for electromagnet development. This general method assumes: 1) linear behavior between magnetic flux and current, 2) average magnetic flux passes through the centroid of the cross-section, and 3) varying cross-section sizes are treated as separate pieces in series or parallel. Analysis begins with determining the mass of the levitating object or the effective mass of the rotor. The electromagnet core and coils are then sized to achieve the attractive force required to lift the shaft and provide feedback. The next steps include electronics hardware and control system design.

Schweitzer [2] provides a complete roadmap of the AMB design process, providing extensive information on rotor system modeling, necessary hardware components, actuator design, potential losses in the AMB, and active control techniques. Rotor system modeling consists of accurately determining the characteristic equation of the rotor system and predicting the vibratory response induced by a disturbance force (mass imbalance during rotation). Load capacity is determined from the maximum static and dynamic loads experienced by the rotor and is then used to size the iron core of the AMB (magnetic force ranges). Apart from the iron core, additional components with guidelines for sizing are introduced. Parasitic losses from eddy currents, hysteresis, and induced heating effects are considered when determining geometry and selecting materials. Active control techniques vary in complexity and include the PID method, H-infinity, and mu-synthesis. The proper method is chosen based on the degrees-of-freedom of the AMB and how many inputs/outputs are being controlled simultaneously.

Due to an AMB's complexity and precision, proper safety guidelines must be established and followed for the design and implementation of an AMB. Failures can occur mechanically, electronically, and in the software. Schweitzer [2] offers insight in regards to safety practice and proper procedures. Standardized procedures as described in the ISO 9000 series are highly recommended. A company or establishment following these procedures can be recognized as a certified institution with a defined quality level. Furthermore, the ISO 14839 1-4 series should be followed as it lays out design guidelines pertaining to mechanical vibrations in rotating machinery equipped with AMB's.

4. Design Requirements

Discussions with the sponsor, Dr. Wu, resulted in a list of design requirements for meeting the goal and scope of the project. The size and function of the RK4 rotor kit was already established, providing constraints that had to be considered while designing the AMB. With the inboard end of the rotor fixed axially by the motor, a 2 degree-of-freedom AMB was the logical choice. This constrained the control methodology to SISO (single-input/single-output) as opposed to MIMO (multiple-input/multiple-output). MIMO is more commonly implemented for multiple AMB systems with more degrees-of-freedom. The design

requirements were divided into customer requirements with corresponding engineering requirements (**Table 4.1**).

Table 4.1. Customer requirements with corresponding engineering requirements.

Customer Requirements	Engineering Requirements
1. Has to work with existing rotor kits	-One magnetic bearing to support one shaft end -Can maintain controlled levitation up to max speed that the vibes lab rotor kits run at (0-3,000 rpm typically, *Max 10,000 rpm*) -Stator outer diameter cannot exceed 12 cm
2. Designed for eventual manufacture of multiple units	-Minimize number and complexity of parts -Design parts for manual machining where possible -Establish repeatable manufacturing processes
3. Controlled via MATLAB	-MATLAB compatible control board
4. Backup system for safe operation during a control failure	-Touchdown bearing included in mechanical assembly
5. Safe for use by students	-No touchable component should exceed 100°F (below the 111°F threshold for 1st degree burns) [6] -Appropriately sized guards shall prevent the user from touching the AMB during operation -Minimize voltages wherever possible -Adhere to electrical safety guidelines presented in class
6. Responsive, but simple controls	-2 DOF system -PID controlled using Simulink -Keep within linear range of stator and rotor material's B-H curve -5 kHz minimum sampling speed for position inputs
7. Capable of supporting shaft with two balancing disks	-Design EM force of 77 N -Safety factor of 3 on EM force required [3]

5. Management Plan

Due to the small size of the project group, each of the members were intimately involved with each aspect of the project. However, some of the tasks were distributed according to the unique strengths of each member. Sean led the manufacturing effort due to his prior project experience producing various machined parts. He saw to the final design and implementation of the AMB stator, rotor mass, and casing as well as the touchdown bearing. Sean was also responsible for the coils windings and their installation on the AMB stator. Garrett led the FEA electromagnetics and rotordynamics analyses used for determining the design specifications of the AMB. He performed the controls analyses in MATLAB and ADAMS. Finally, Garrett saw to the design and implementation of the power electronics that included the wiring and enclosure. A third and very important addition to the group, Cameron Naugle (who was a graduate student working for Dr. Wu), saw to the selection and implementation of the NI cRIO-9063 FPGA controller and LabVIEW real-time control program that took the place of the originally conceived Simulink compatible controller mentioned in the customer requirements.

The senior project design process flow chart for the year is included below in **Figure 5.1** to provide an outline of when various tasks were performed. We worked with a slightly accelerated schedule, in that our detailed design work for the bearing assembly was performed in the fall. Design work for the electronics systems and controls was the primary focus during winter quarter.
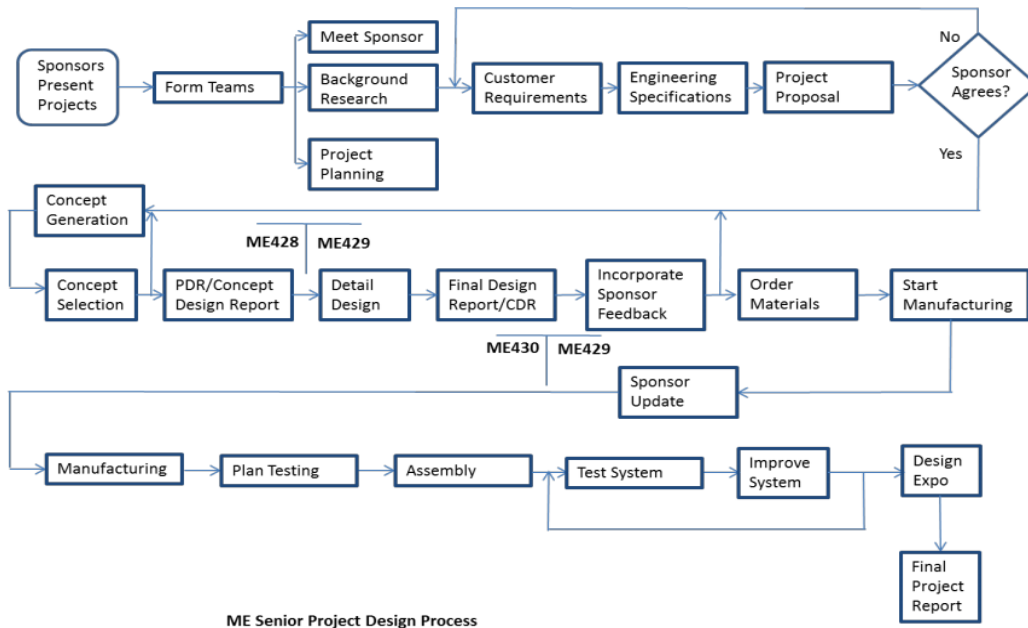
Figure 5.1. Senior project design process flowchart.

6. Design Analysis
6.1. Static and Dynamic Load Capacity

The first step in designing the AMB was to determine the magnetic force that the bearing had to produce to levitate the rotor. This involved an analysis of a two-plane mass rotor system suspended between two bushings. A theoretical model in MATLAB was developed and tuned to match the experimental results. The rotor model consisted of two similar masses suspended on a shaft at different lengths from each end of the rotor at L1 and L3 **(Figure 6.1a)**.

Experiments were also conducted using ADRE 408 for data-acquisition. The rotor was attached to an inboard motor with a maximum operable speed of 10,000 rpm. The rotor was operated at speeds ranging from 245 rpm (slow roll) to 7,000 rpm with a ramp rate of 5.24 rad/sec^2.
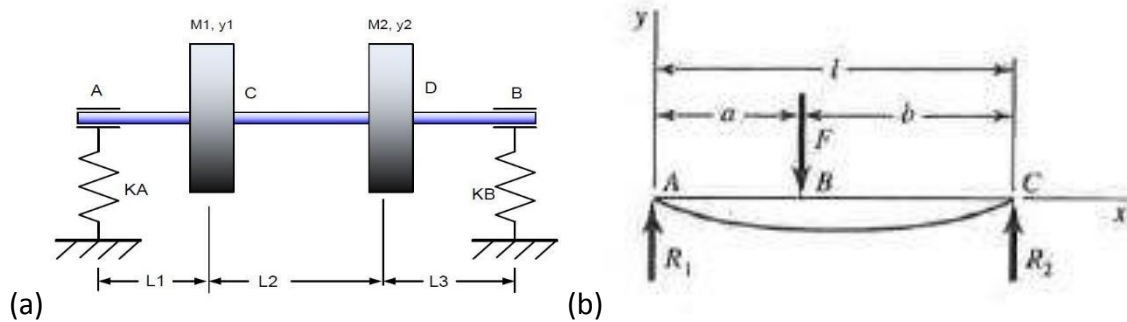
Figure 6.1. (a) **Case 1:** Rigid shaft, flexible bearings. (b) **Case 2:** Rigid bearings, flexible shaft.

A theoretical model was developed to validate the experimental results utilizing the Superposition Method [Notes: Rotordynamics, Wu] where the shaft stiffness matrix was determined. Spring stiffness values for two cases, 1) a rigid shaft with flexible bearings and 2) a flexible shaft with rigid bearings **(Figure 6.1)** were determined and combined in parallel to produce an equivalent system stiffness matrix. The equations used to develop these matrices are as follows:

1) Rigid Shaft with Flexible Bearings

$$C_b = \frac{1}{L^2} \begin{bmatrix} \dfrac{L_1{}^2}{K_b} + \dfrac{(L_2 + L_3)^2}{K_a} & \dfrac{L_1(L_1 + L_2)}{K_b} + \dfrac{L_3(L_2 + L_3)}{K_a} \\ \dfrac{L_1(L_1 + L_2)}{K_b} + \dfrac{L_3(L_2 + L_3)}{K_a} & \dfrac{(L_1 + L_2)^2}{K_b} + \dfrac{L_3{}^2}{K_a} \end{bmatrix}$$

10

2) Flexible Shaft with Rigid Bearings

$$C_s = \begin{bmatrix} \dfrac{L_1{}^2(L_2 + L_3)^2}{3EIL} & \dfrac{L_1 L_3 (L^2 - L_1{}^2 - L_3{}^2)}{6EIL} \\ \dfrac{L_1 L_3 (L^2 - L_1{}^2 - L_3{}^2)}{6EIL} & \dfrac{L_3{}^2(L_1 + L_2)^2}{3EIL} \end{bmatrix}$$

3) Total Stiffness

$$K = \frac{1}{(C_b + C_s)}$$

The K_a and K_b values represent the estimated stiffness of the inboard and outboard bushings, respectively, and were set at 290,000 N/m. Damping was estimated at 0.0003*K. The masses included in the mass matrix were those of the disks, each having the same value of 0.5 kg. The mass, stiffness, and damping values were implemented in matrix format:

$$\mathbf{M\ddot{y} + D\dot{y} + Ky = F(t)} \qquad \text{where } \mathbf{y} = \begin{Bmatrix} y_1 \\ y_2 \end{Bmatrix}$$

An expanded format of this equation was created in an ODE45, MATLAB function file that was used to generate the displacement amplitude of each disk over a specified length of time:

$$M_1\ddot{y}_1 + c_{y11}\dot{y}_1 + c_{y12}\dot{y}_2 + k_{y11}y_1 + k_{y12}y_2 = M_1 a_1 \omega^2 \sin\left(\omega t + \varphi_{y1}\right) + M_1 a_1 \alpha \cos\left(\omega t + \varphi_{y1}\right)$$

$$M_2\ddot{y}_2 + c_{y21}\dot{y}_1 + c_{22}\dot{y}_2 + k_{y21}y_1 + k_{y22}y_2 = M_2 a_2 \omega^2 \sin\left(\omega t + \varphi_{y2}\right) + M_2 a_2 \alpha \cos\left(\omega t + \varphi_{y2}\right)$$

An eccentricity of 3 mils and a phase of 0 rad and π/8 rad were used for disks 1 and 2, respectively. These values, along with the estimated stiffness of the inboard and outboard bushings, were tuned until the theoretical and experimental responses matched. **Figure 6.2** shows the responses of each disk ranging from 0 to 4,000 rpm and 0 to 10,000 rpm. Both the experimental and theoretical models indicate a first natural response at 1,100 rpm and have similar response profiles.

Once validated by the experimental results, the theoretical model simulation was extended to 10,000 rpm to view potential responses occurring at the operating limit of the RK4 system. It should be noted that experimental data was cut off above 50 mils (peak to peak) which is the maximum expected displacement during safe rotor use. In this case, the shaft's deflection was physically limited by impacting the proximity sensors. The amplitude response of the theoretical model predicted the extended measurable response of the actual model.
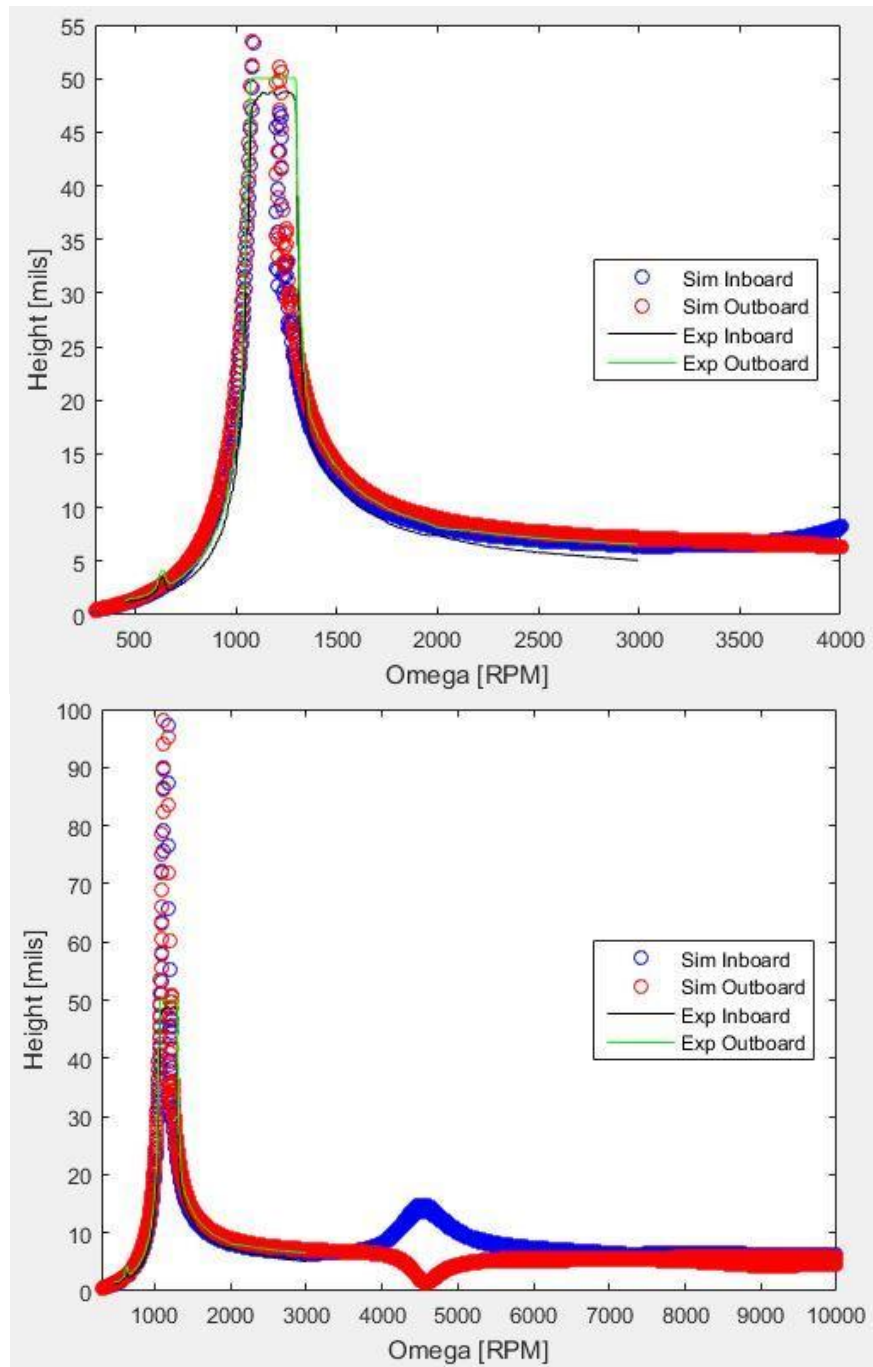
Figure 6.2. *Top:* MATLAB and Experimental results with matching natural frequencies and amplitude widths. *Bottom:* Extended MATLAB model between 0-10,000 rpm with amplitude response approaching 100 mils.

The displacement amplitudes of both masses were used to find the maximum dynamic forces experienced by the rotor. **Figure 6.3** shows the dynamic forces experienced by each bushing with speed ranging from 0-10,000 rpm. Both the static and dynamic forces of each disk at their respective locations were combined, and the moments experienced by the inboard and outboard locations were used with the shaft length to determine the loads at each fixed end.
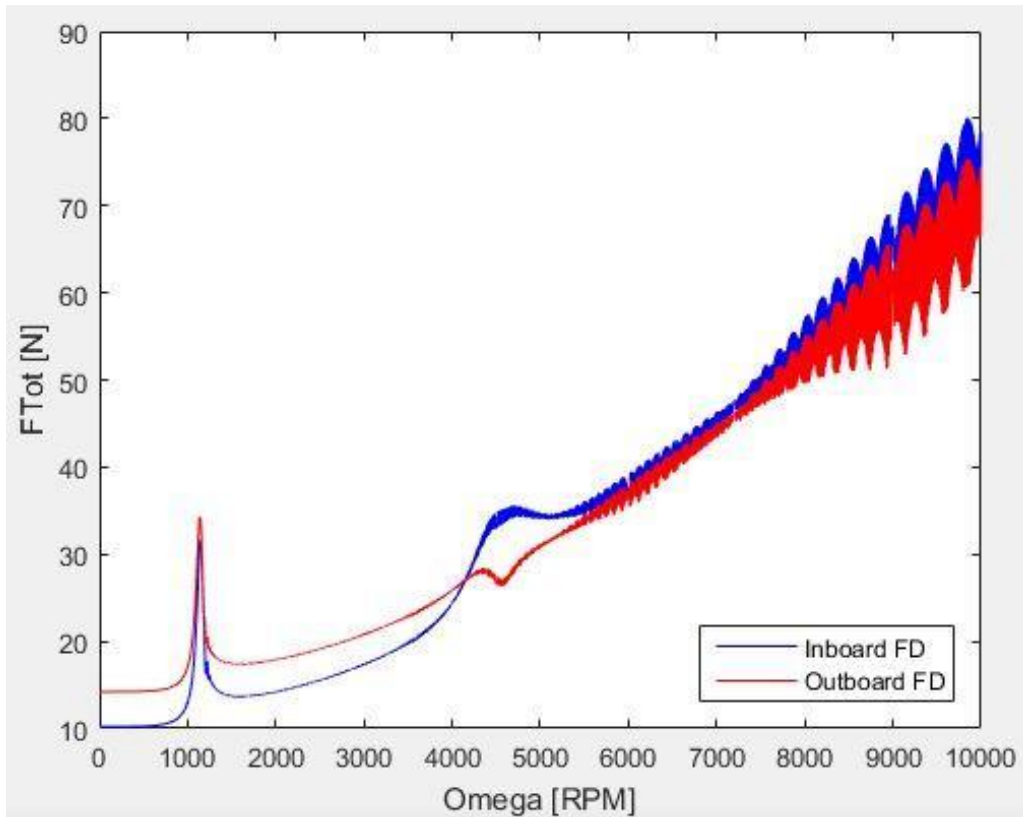
Figure 6.3. Total force reactions at the inboard and outboard bushings.

These calculated load capacities are a high estimation of what may be experienced during typical rotor kit use. **Appendix C** provides the MATLAB code used in the load capacity analysis and may be tuned for different rotor system setups. The bushing in the place of the AMB provides a good initial estimate of rotor performance and bearing stiffness values that may be used to size the AMB. Once built, stiffness in the AMB may be adjusted by adjusting the bias current of each actuator pair, as described in the following sections.

Table 6.1. RK4 system parameters and expected load capacities experienced at the outboard location.

L1 (m)	0.197
L3 (m)	0.2
Total Length (m)	0.53
Mass of Disk (kg)	0.8 per disk
Rotor Mass (kg)	0.5
Omega (RPM)	300-3000
Static Load Capacity (N)	14.3
Dynamic Load Capacity (N)	62.4
Total Load Capacity (N)	76.7

6.2. Actuator Generated Magnetic Force

With the maximum force required for stable operation calculated, the next step was the mechanical design and sizing of the AMB. The analysis performed follows the models developed in [3] and Chapter 3 of both [2] and [7]. These begin with the force produced by a single magnetic actuator, and then develop into models for two magnetic actuators acting in opposition to each other. This is what is found on 2-axis AMB's. One pair of actuators must be used to balance the rotor mass for each axis because magnetic actuators can only provide an attractive force. The total force on the rotor provided by the opposing electromagnets is linearized to include a current "stiffness" and displacement stiffness. The analysis assumes that the cross-sectional area of the back iron **(Figure 6.4)** is equal to that of the poles and rotor iron such that a uniform cross-sectional area is maintained throughout the entire magnetic circuit. It is also assumed that the air gap between the stator and rotor is small compared to the stator and rotor dimensions.
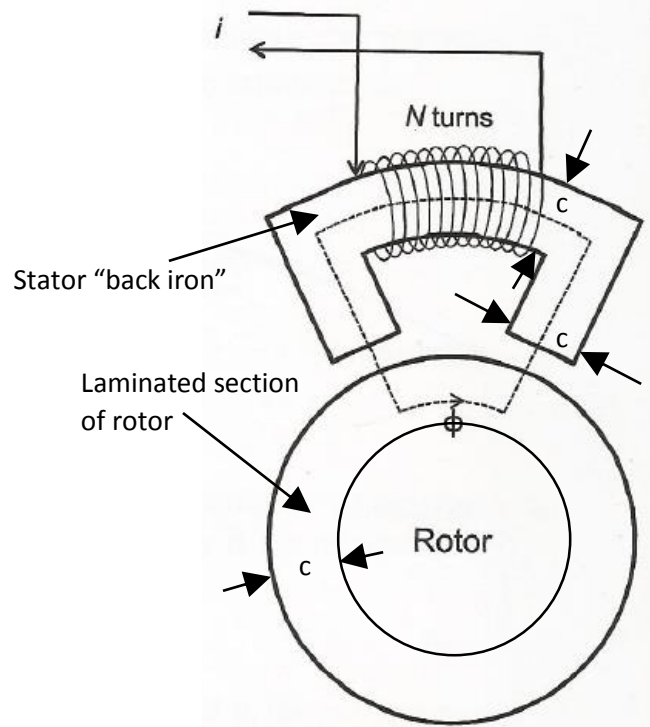
Figure 6.4. Single magnetic actuator model. Modified from [7].

The magnetic actuator can then be modeled as a magnetic circuit **(Figure 6.5)** with magnetic flux (Φ) as the analog for current, total reluctance (R_t) for resistance, and magnetomotive force (MMF) as voltage, such that

$$MMF = \Phi R_t.$$
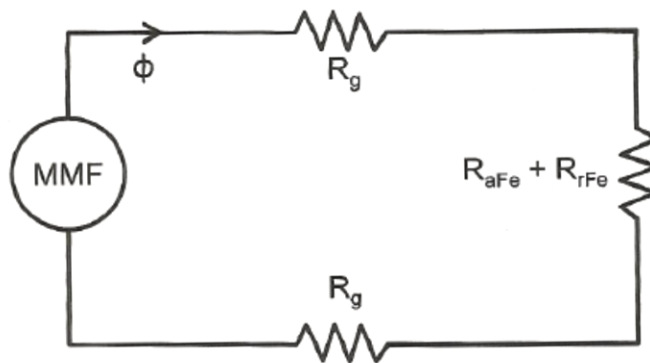
Figure 6.5. Magnetic circuit of actuator. From [7].

The reluctance of the circuit can be determined as with summing resistors in series. The total reluctance of the circuit then is equal to the reluctance of the two air gaps plus the reluctance of the rotor and the reluctance of the stator. Reluctance is given by the equation:

$$R = \frac{L}{\mu A}$$

L is the mean length of the path traveled by the flux and A is the cross-sectional area of the material. Because the permeability of free space ($\mu_0 = 4\pi \times 10^{-7}$ [N/A^2]) is on the order of 1,700 to 6,000 times smaller than the permeability of the silicon steel or "iron" of the stator and rotor, the reluctance of the stator and rotor can be neglected so that the total reluctance is given by

$$R_t = \frac{2s}{\mu_0 A} \; .$$

Note that A in this case is technically the cross-sectional area of the air gap through which the flux passes. Since fringing (where some flux is allowed to spread out and escape in making the transition across the air gap) is assumed to be negligible, and since the cross-sectional area of the material is kept constant through the flux path, A remains equal to the cross-sectional area of the stator pole (A = bc, as shown in **Figure 6.6** below). Since

$$MMF = Ni,$$

where N is the number of coil turns of the electromagnet and i is the current flowing through the coils, the magnetic flux in the circuit can be written as

$$\Phi = \frac{Ni\mu_0 A}{2s}.$$

The magnetic flux density is given by

$$B = \frac{\Phi}{A},$$

and can be used to calculate the attractive force produced by the magnetic actuator,

$$F = \frac{B^2 A}{\mu_0} \; .$$

In a form that is more useful for designing and which includes a correction factor, ε, to account for fringing and leakage losses, the force equation becomes*

$$F = \frac{\varepsilon \mu_0 N^2 i^2 A}{4s^2}.$$

[7] suggests a value for ε of 0.8 for radial bearings.

To extend this model to a two actuator system, the total force becomes

$$F_{tot} = F_1 - F_2 = \frac{\varepsilon \mu_0 N^2 i^2 A}{4} \left[\frac{i_1^2}{s_1^2} - \frac{i_2^2}{s_2^2} \right].$$
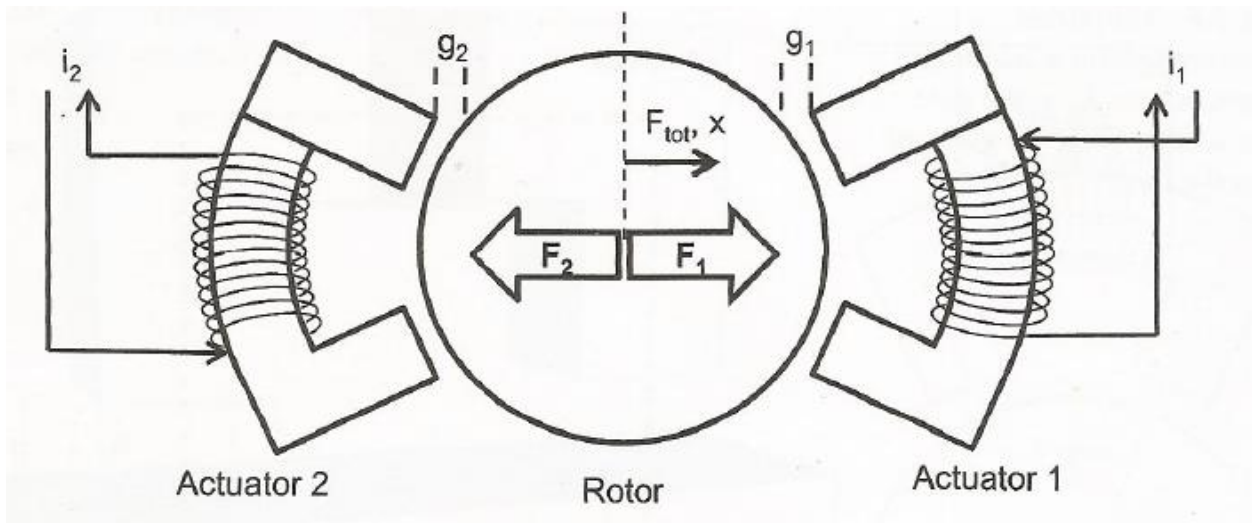
Figure 6.6. Two magnetic actuator model. From [7].

The linearization of this equation begins by defining i_0 as the base current or bias current and i_x as the perturbation current. The minimum perturbation current is zero while the maximum perturbation current is equal to the base current such that i_{max} through an actuator is equal to $2i_0$. Since for the force equation above, $F_1 > F_2$, likewise $i_1 > i_2$, so i_1 and i_2 may be defined as

$$i_1 = i_0 + i_x,$$

and

$$i_2 = i_0 - i_x.$$

17

Similarly, with s_0 defined as the nominal air gap present when the rotor is centered and x defined as the displacement of the rotor from its center position, s_1 and s_2 can be defined as

$$s_1 = s_0 + x,$$

and

$$s_2 = s_0 - x.$$

Using Taylor series expansion, the force equation can be modified to take the form

$$F_{tot} = K_i i_x - K_s x$$

where K_i is the open loop current gain or current "stiffness",

$$K_i = \frac{\varepsilon \mu_0 N^2 A i_0}{s^2} \cos(\alpha),$$

and K_s is the open loop stiffness of the actuator,

$$K_s = -\frac{\varepsilon \mu_0 N^2 A {i_0}^2}{s^3} \cos(\alpha) \, .$$

Here, the term $\cos(\alpha)$ has been added to account for the geometry of a two pole magnetic actuator where the centerlines of the poles are separated by an angle of α. For an 8 pole magnetic bearing with the poles spaced equally around the rotor, $\alpha = 22.5°$.

6.3. FEA Analysis

Generated magnetic forces and magnetic flux densities were analyzed utilizing the FEA method in Abaqus. Magnetic forces by each of the 8 poles were induced by an applied current to each actuator that acted perpendicular to an applied current density field inside solid copper windings. The expected force for a full scale AMB model was 36 N given the designed geometry and bias current. By scaling down the stator and rotor mass to 1/7 the thickness, the expected generated force became 5 N. This was validated through a convergence study that averaged the body forces of elements contained in each pole region.

For the purpose of this analysis, material properties were considered for M19 silicon steel (stator and rotor) and air. Copper properties were not included but should be considered for a future magnetic/thermal coupled simulation. **Table 6.2** provides the material properties used as well as magnetic force parameters.

18

Table 6.2. Material properties for M19 Silicon Steel and air as well as the magnetic force parameters governing the analysis.

M19 Silicon Steel Properties		Magnetic Force Parameters	
Gage	29	Bias Current (Amps)	1.4
Laminate Thickness (mm)	0.36	Current Density (A/m2)	2.70E+06
Number of Laminates	98.43	# Coils (Per Actuator)	250
Density (lb./in^3)	2.78E-01	G_o (m)	5.00E-04
Elect. Conductivity (Ohm-m)	5.00E-07	Mu_o(Perm$_{Air}$)	1.2566E-06
Rel. Perm. (Mu_r)	8.19E+03	Eps (Leakage + Fringing)	0.8
Resistivity (Ohm-m)	4.60E-07	A_{act} (m2)	4.25E-05
Curie Temperature (deg. C)	800	Gap Factor	1.05
P-sat (lb./in2)	171	A_{gap} (m2)	4.46E-05
Cp. (J/kg-K)	486	F_{mag} (N)	5.23
Air Properties			
Temperature (deg. C)	20		
Rel. Perm	1		
Density (lb./in^3)	4.34E-05		
Resistivity (Ohm-m)	3.30E+16		
Elect. Conductivity (S/m)	8.00E-15		
Therm. Conductivity (W/m-K)	2.57E-02		
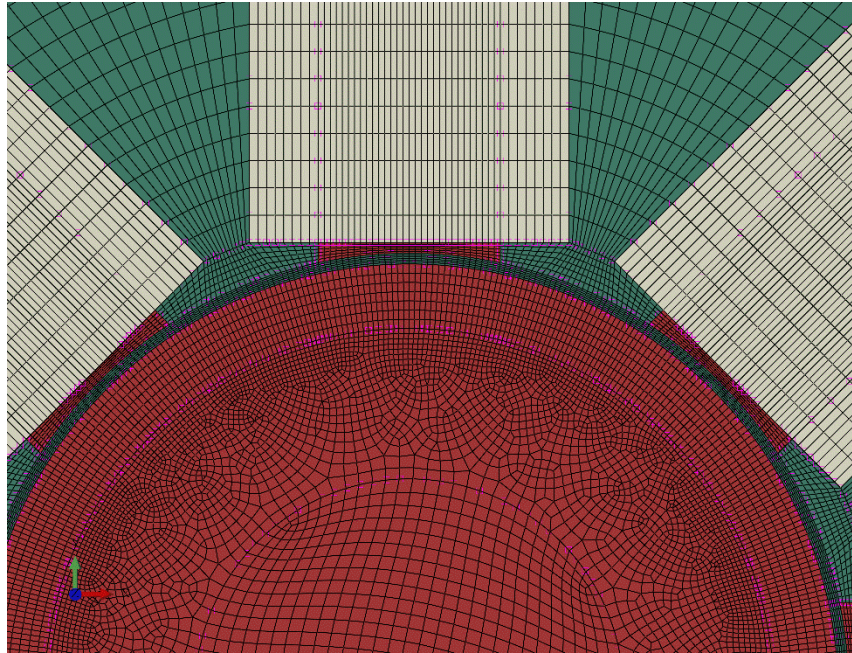
Figure 6.7. Mesh density fields of stator, poles, and air gap.

The FEA model consisted of partitioned sections representing the stator, copper windings, rotor mass, and air. All partitioned sections were mated together to form one solid piece. Within each main partition, sub-partitions were created to allow for linear quadratic elements to be used during the mesh process. The geometry of the assembly prohibited the use of global seeds, therefore sets of edges were created to define the varying seed sizes. **Figure 6.7** shows the congruency of each partitioned section during meshing. The smallest elements were in the air gap between the poles and rotor mass. Elements at the outer edge of the rotor mass were made the same size as those of the air gap.

The rotor mass itself was divided into three rung sections with the largest edge bias being towards the outside. Much of the generated magnetic flux during simulation was expected towards the outer edge of the rotor, therefore smaller seed sizes were used in this rung that lined up with nodes of the air gap elements. The seed sizes were made considerably larger moving towards the center of the rotor in order to reduce the number of elements during simulation.

Figure 6.8 and **Figure 6.9** give snap shots of both the generated magnetic body forces and magnetic flux. Results in both figures involved a total of 250,000 elements. Initially 1.1e06 elements were used, however this greatly increased the simulation run time. The magnetic body forces between each pole and rotor mass were averaged, producing results that matched those of **Table 6.2**.
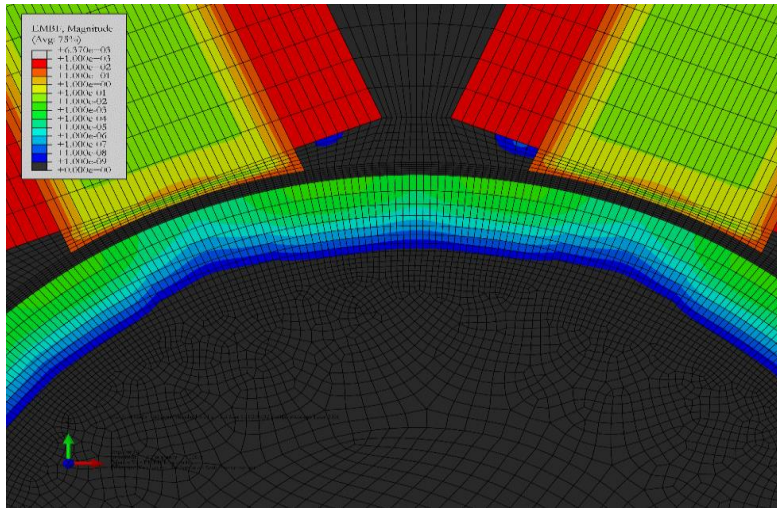
Figure 6.8. Force produced by the magnetization of each pole was compared to theoretical values for validation of the finite element model.

Stator/Rotor Interactions
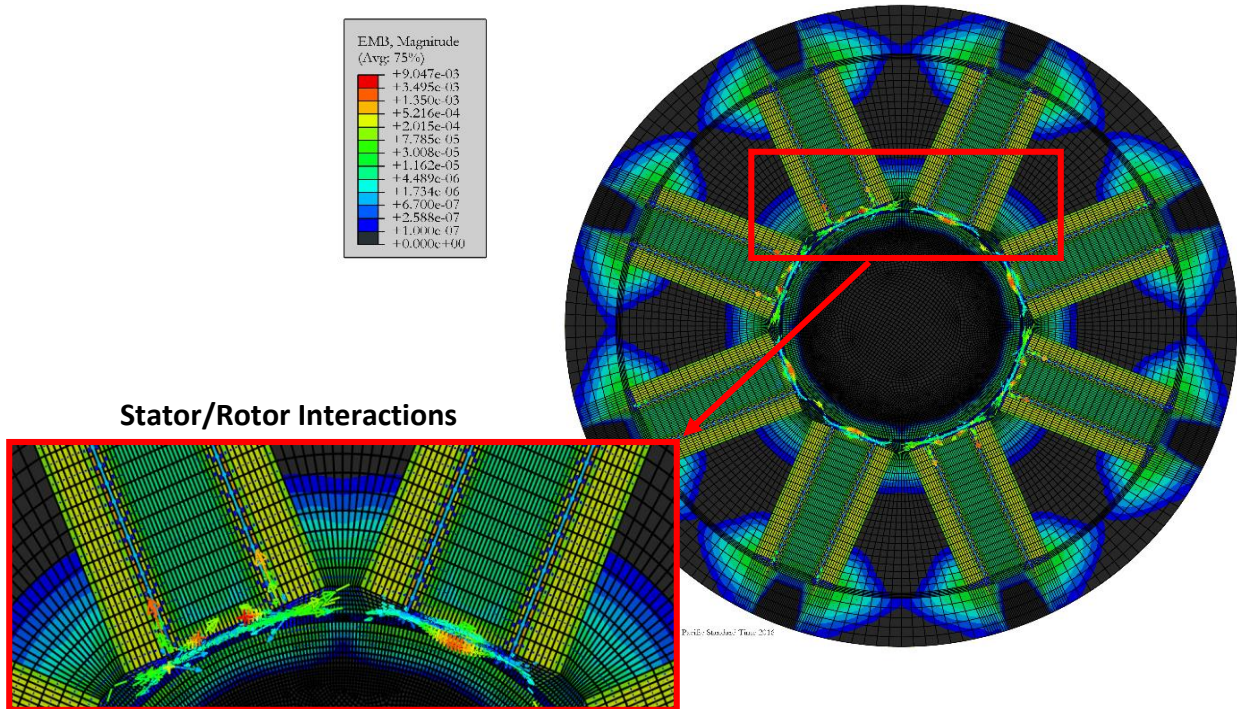
Figure 6.9. Magnetic flux density field with equally applied current density to copper surrounding all 8 poles of the stator.

Magnetic flux leakage occurring at the pole corners and air gaps is also evident in **Figure 6.9**. A fringing and leakage coefficient of 0.8 [2], [3] was assumed throughout the design process. For better accuracy, future FEA analyses may be performed that may quantify this coefficient through magnetic flux averages in various regions between the stator poles and air. Furthermore, a thermal/electromagnetic analysis could be performed to estimate the effect of heating from the copper coils on the magnetic permeability of the stator and rotor.

The FEA study provided a proof of concept and led to our final decision of going with M19 steel. For this study, 250 coils per actuator were used, however our final design came to include 300 coils. Due to time constraints, no further analyses were performed, however it is encouraged to make use of this existing approach moving forward to better quantity system characteristics for more precise applications.

6.4. Heat Transfer

Heat transfer was also considered throughout the iterative process. Two methods of heat transfer analysis were included in the MATLAB based design analysis (see **Appendix D**). The first took an elementary physics approach and calculated the amount of time required to increase the temperature of the coils and immediately adjacent core material by 30°F (presumably from a room temperature of approximately 70°F to the design limit of 100°F). This analysis assumed, based on the limited convection and conduction coefficients suggested by [8], that all of the resistive power losses dissipated by the coils would be stored by the coils and the core material surrounded by the coils as thermal energy. This helped to produce some intuition as to how rapidly the assembly would heat up.

The second analysis followed more closely to the 1-D heat transfer analysis outlined in [8]. This method calculates the heat transfer away from the coils assuming a 30°F temperature difference between the coils and the surrounding air and between the coils and the back iron of the stator. The calculated heat transfer rate could then be compared to the power dissipated due to resistive losses.

Both of these methods involved simplified versions of the relatively complex stator geometry, and can only be taken as ballpark approximations. Analogies to similarly sized hardware were sought so as to provide better intuition regarding how dissipated electrical power produces detectable temperature rises. An energy efficient laptop computer, for example, dissipates 15-25 Watts into a confined space with only modest temperature rises. This is achieved in part due to a small cooling fan. This analogy sheds some doubt on the results of the second heat transfer analysis, which indicated that a 30°F temperature difference between the coils and their open surroundings would only result in the transfer of 5.4 Watts. Intuitively, given the open nature of the bearing assembly and the large heat sink provided by the stator, the 5.7 Watts calculated to be dissipated by the coils would likely be transferred to the surroundings with only a minimal rise in overall AMB temperature. This analysis did

demonstrate the utility of minimizing current through the coils, which was taken into consideration when designing other parameters. Fortunately, this analysis does tell us that the system ought to be easily cooled using a small computer fan providing forced convection over the stator.

6.5. Physical Constraints

With the design force equation developed, work then began on determining the geometry and design parameters of the magnetic bearing. A number of constraints were determined based on the geometry of the RK4 rotor kit and recommendations made by various research groups and authorities on magnetic bearing design. In the following analysis, a safety factor of 3 was used for the design force as recommended in [3]. The outer diameter of the stator was also constrained to a maximum of 12 cm so that it could be made to fit within the V-shaped channel of the RK4 rotor kit.

According to [2], the most significant AMB power losses are due to the resistance of the copper coils. Since wire resistance is inversely proportional to wire cross-sectional area, using the largest possible wire diameter for the coils would minimize resistive losses. However, the wire diameter also have to be small enough to allow the coils to be easily wound around the stator poles and to allow the necessary number of coils to be wrapped around a given pole without making the poles so long as to exceed the 12 cm limit on the stator outside diameter. In [8], AWG 18 copper wire (1.02 mm diameter [9]) was used for a similarly sized AMB. By inspection, this appeared to be the largest wire diameter that would appropriately meet the described constraints, so it was selected as an upper limit for the analysis. Once the electrical hardware design began, it became clear that limiting the current provided to the actuators would be desirable in order to be able to use more available, lower cost power electronics components. Between AWG 18, 20, and 22, gauge 22 wire was selected. Reducing the wire diameter allows more windings to be added to each pole, which allows the same design force to be applied using less current. The tradeoff is that this also reduces the force slew rate (see Figure 9), which theoretically lowers the maximum operating speed. Gauge 22 wire should still allow a maximum controllable rotor speed of 10,000 RPM. The reduction in current also meant that the design adhered to another rule of thumb presented in [8], which is to keep the current density within the copper coils below 6 [A/mm^2] to avoid overheating.

This parameter is also relevant to the selection of the bias current. [7] recommends beginning by setting the base current equal to the current level that would produce a flux density equal to one half B_{knee}, or the value on the stator and core material's B-H curve which marks the upper limit of the linear range (**Figure 6.10** below). Grade M19 silicon steel was chosen as the rotor and stator material based on manufacturer recommendations [10]: "M19 is probably the most common grade for motion control products, as it offers nearly the lowest core loss in this class of material, with only a small cost impact, particularly in low to medium

production quantities." The silicon in "silicon steel" is alloyed with the steel to increase the material's resistance. This reduces losses due to eddy currents forming in the material, which are induced by the oscillating magnetic field. M19 silicon steel is commonly used in electric motor laminations. It is also a readily available stock material that most lamination manufacturers keep on hand, meaning its use should aid in limiting lead times during the manufacturing stage of the project. From data provided by [11], B_{knee} for M19 silicon steel is 1 Tesla. This was used as an initial rule of thumb for determining i_0 such that

$$i_0 = \frac{s_0 B_{knee}}{\mu_0 N}.$$

As the analysis progressed, B_{knee} was replaced by scalable parameter "B_{max}", or the maximum flux density produced by the design. During the design process, this served as a method to reduce i_0 and therefore minimize resistive losses without drastically changing the format of the MATLAB analysis (see **Appendix D**). B_{knee} was then treated as a constraint on B_{max} such that
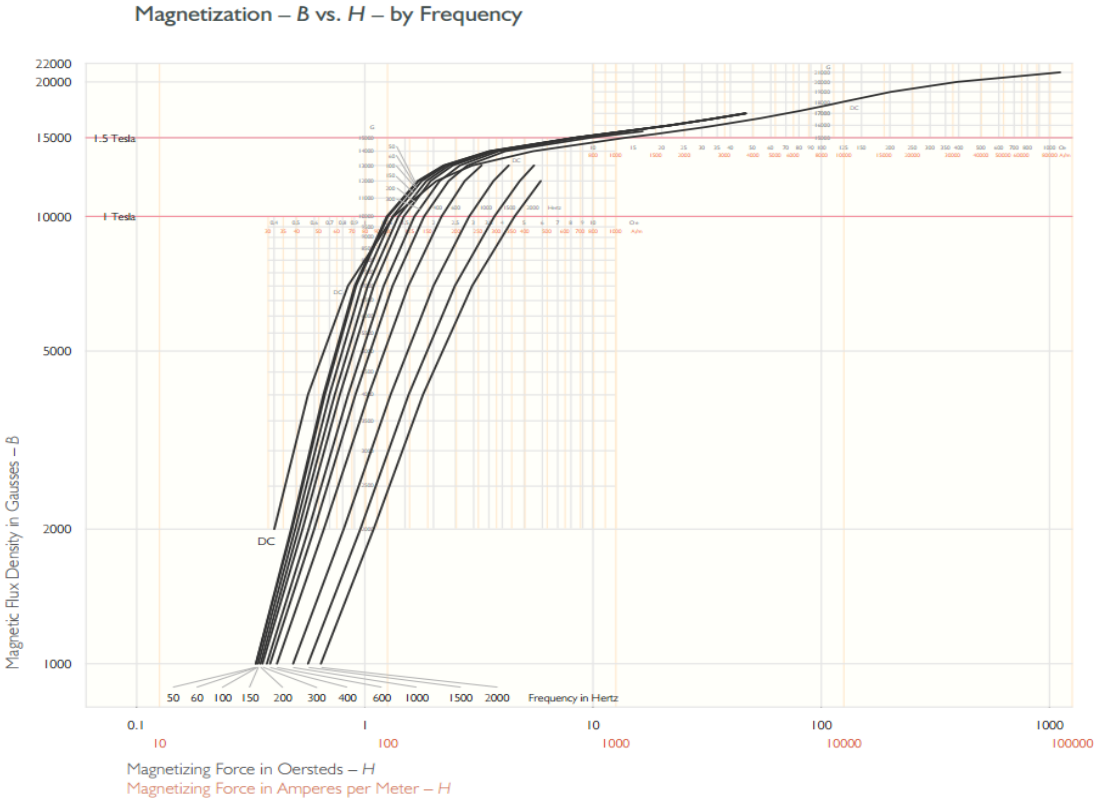
$$B_{max} \leq B_{knee}.$$

Figure 6.10. M19 B-H curve [11].

24

At high rotational frequencies, the current slew rate (max time rate of change of the current), can limit the force output of the AMB and therefore limit the operation speed of the rotating system. The current slew rate is related to the inductance of the system and is given in [7] as

$$max\left|\frac{di}{dt}\right| = \frac{2s_0v_{max}}{\mu_0N^2A}.$$

Here, v_{max} is the maximum voltage capable of being provided by the amplifier connected to each actuator. Multiplying this value by Ki gives the force slew rate,

$$max\left|\frac{dF}{dt}\right| = \frac{2\varepsilon i_0 v_{max}}{s_0}.$$

The force output of one of the opposing actuators for an axis has a sinusoidal nature in order keep the rotor balanced at its center position [7].   This force output as a function of time can therefore be modeled to take the form

$$f = Msin(\omega t)$$

while its time derivative then takes the form

$$\left|\frac{df}{dt}\right| = |Mcos(\omega t)\omega|.$$

$\frac{df}{dt}$ is limited by $max\left|\frac{dF}{dt}\right|$, meaning that the magnitude $|M|$ of the output force is limited such that,

$$|M| = \frac{2\varepsilon i_0 v_{max}}{s_0\omega}.$$

Therefore, the bias current and voltage output of the amplifier must be high enough so that the magnetic actuators can provide the design force throughout the entire range of operating speeds, ω. This is best verified through a log-log plot of the max load capacity vs. frequency. The intersection of the calculated design force and maximum force as a function of frequency can then be used to determine whether the system designed is capable of operating at the speed desired. Such a plot is presented by [7] and included below. During our conversation with Dr. Zhu from Solar Turbines, he estimated that about 80V, would be required for our application. As he described, this is because the inductance of the system should be considered the real driver for determining voltage. The load capacity plot, **Figure 6.12,** has been included for a max voltage of 72 Volts, which would theoretically provide a maximum

slew-rate limited operating speed of over 10,000 RPM. The real limit on speed then becomes the frequency at which the controller can run the PID control.
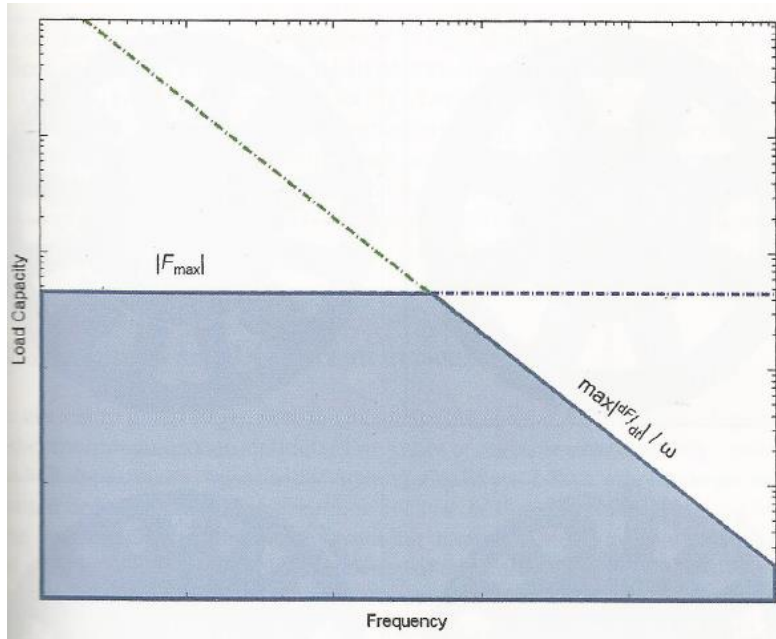

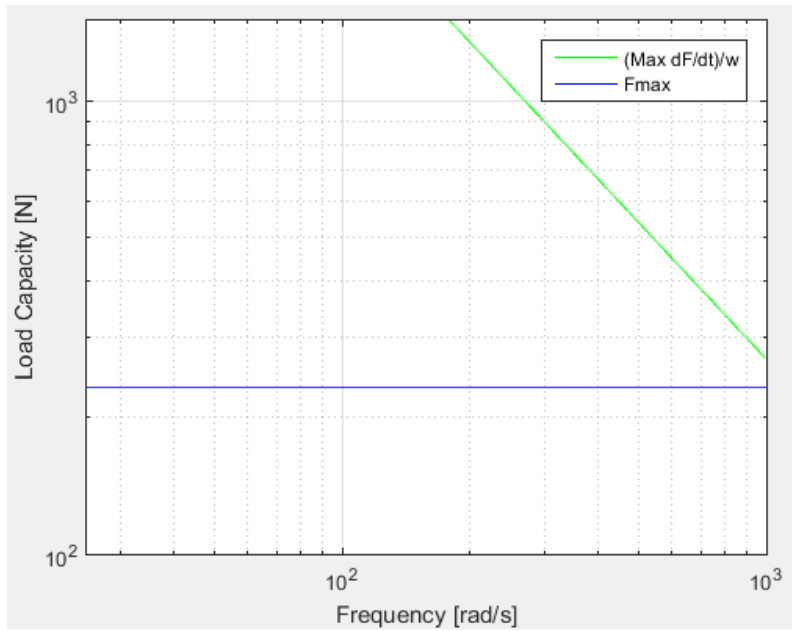**Figure 6.11.** Log-log plot of the load capacity vs. frequency from [7].

Figure 6.12. Log-log plot of the load capacity vs. frequency using design values. Note that the maximum force output is still possible up until the max speed of 10,000 rpm (1,047 rad/sec).

6.6. Physical Parameter Optimization

Once as many meaningful constraints were placed within the model as possible, several key variables were modified iteratively to come to a working design. These variables are presented in the following table. While more sophisticated techniques for optimizing the design parameters are available and described in [8], such methods were not possible given the time constraints on the project. These methods are also best utilized with more accurately characterized heat transfer phenomena.

Table 6.3. Design parameters and their effect on the AMB system.

Design Parameter	Description and Effect of Modification
Number of coils per actuator (N)	Increasing N increases actuator force output and resistive losses by increasing the total coil length.
Maximum flux density (B_{max})	$B_{max} \leq B_{knee}$. Decreasing B_{max} decreases bias current and resistive losses.
Max amplifier voltage (V_{max})	Increasing V_{max} increases the force slew rate and therefore allows the system to run at higher rotational speeds. Increasing V_{max} also increases the risk of electric shock.
Air gap (s_0)	Decreasing s_0 decreases the number of coils and the amount of current required to achieve the design force. s_0 is limited by achievable machining tolerances. Based on the capabilities of the Cal Poly machine shops and precedents set by [3] and [8], an air gap of 0.5 mm was selected.
Pole length past the coil (ppc)	Increasing ppc increases the stator outer diameter. 2mm was deemed appropriate for preventing the coils from slipping off the end of the pole.
Number of coil layers (nl)	Increasing nl minimizes the stator outer diameter, but can cause interference between the coils of adjacent poles. Increasing nl also reduces losses due to leakage.
Pole width (c)	The pole width also affects the rotor and back iron thickness (**Figure 5**). Increasing c increases the actuator output force but increases stator and rotor outer diameter and increases the chance of interference between coils of adjacent poles. A rule of thumb provided by [2] is to adjust c to make 50% of the stator inner circumference consist of pole material.
Stator, rotor axial thickness (b)	Increasing b increases the actuator output force but also means that the rotor and stator laminations must be joined more precisely to ensure proper alignment within the limited air gap. b must also be limited so that when the

	middle of the shaft experiences a deflection, that deflection does not cause the inboard end of the rotor to hit the inside of the stator before the shaft contacts the touchdown bearing. This was approximated using similar triangles.
Rotor laminations inner diameter (di)	Increasing di increases the stator outer diameter but also allows c and therefore the actuator output force to be increased without causing adjacent coil interference. 23 mm was selected for di because it struck a balance between increasing the stator outer diameter and allowing enough room for adjacent coils. It also allows for the use of the same connectors that join the Bently Nevada RK4 shaft to the Bently Nevada journal bearing rotor. Use of this existing hardware would allow the AMB rotor location on the shaft to be easily adjustable.

6.7. Design Results

The table below includes selected and calculated parameter values that characterize the design chosen. Geometric parameters are included and correspond to the figure below, modified from [2].

Table 6.4. Design results from Appendix D analysis.

Parameter Description (MATLAB variable)	Value
Coil Parameters	
Number of coils per actuator (N)	300 coils
Magnet wire diameter (dcc)	0.668 mm (AWG 22)
Number of coil layers on one pole (nl)	4 layers
Maximum current density	6.66 A/mm^2
Power and Heat Transfer Parameters	
Voltage provided by amplifier (V_{max})	80 Volts
Bias current (i0)	1.2 Amps
Perturbation current (ib)	-1.2 to 1.2 Amps
Power dissipation due to coil resistance (P)	5.7 Watts
Heat transfer rate (q_tot)	5.4 Watts
Minimum time to reach 100°F (t)	21 min
Geometric Parameters	
Air gap between stator and rotor (s0)	0.5 mm

Length of stator pole past the coil (ppc)	2 mm
Stator thickness (b)	35 mm
Pole leg width (c)	8.5 mm
Inner diameter of rotor laminations (di)	23 mm
Coil height (hc)	25.5 mm
Laminated rotor outer diameter (dr)	40 mm
Stator inner diameter (d)	41 mm
Stator outer diameter (da)	11.3 cm < 12 cm
Force Parameters and Constants	
Max force output desired (F_{worst})	77 N
Max force output generated (FgenMax)	232 N
Force safety factor (SF)	3
Maximum flux density (B_{max})	0.88 Teslas < B_{knee}
Loss factor (eps)	0.8
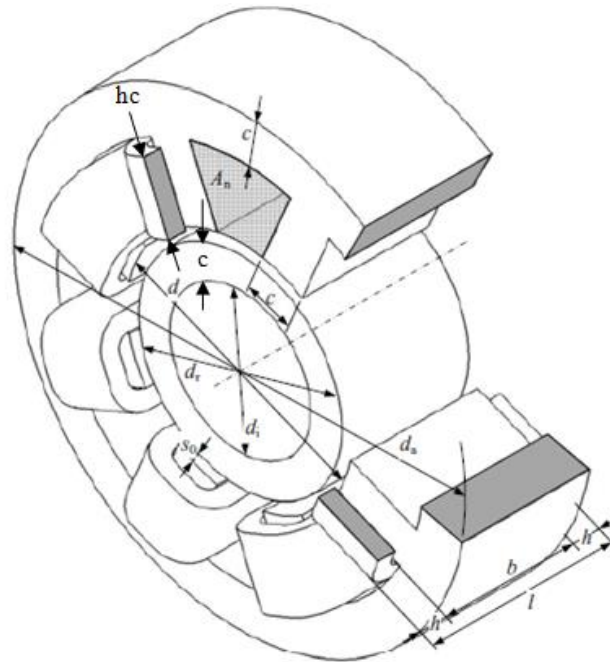
d	Inner diameter (bearing diameter)	d_a	Outer diameter
c	Leg width	d_s	Shaft diameter
hc	Winding height	b	Bearing width (magnetically active)
d_r	Rotor diameter	s_0	Nominal air gap

**Figure 6.13.** AMB geometry dimensions modified from [2].

The **Appendix D** MATLAB analyses produced the functional parameters of the AMB's mechanical system. A depiction of the resulting stator and rotor is displayed below.

7. AMB Design

With the stator and rotor dimensions determined, the assembly for mounting the stator, sensors, and touchdown bearing could then be designed. The design illustrated below makes use of the existing rotor kit bearing mount for the touchdown bearing and the sensor mount for the proximity sensors. The rotor kit uses lubricated bronze bushings, mounted in the bearing mount displayed below, to support the shaft. The touchdown bearing for the AMB made use of the same mount. This bushing was created by drilling out the inner diameter of a 10 mm rotor kit bushing with a lettered Z drill bit, thereby increasing the inner diameter to 10.5 mm. This provided a clearance of 0.25 mm (0.25 mm < 0.5 mm air gap) between the shaft and the bushing, which was thought to be able to prevent the rotor of the AMB from contacting the inner diameter of the stator during startup and during loss of control. This is critical to preventing damage to the rotor and stator. Utilizing the existing mounting hardware for the touchdown bearing and sensors also allowed for a simple stator mounting case design.
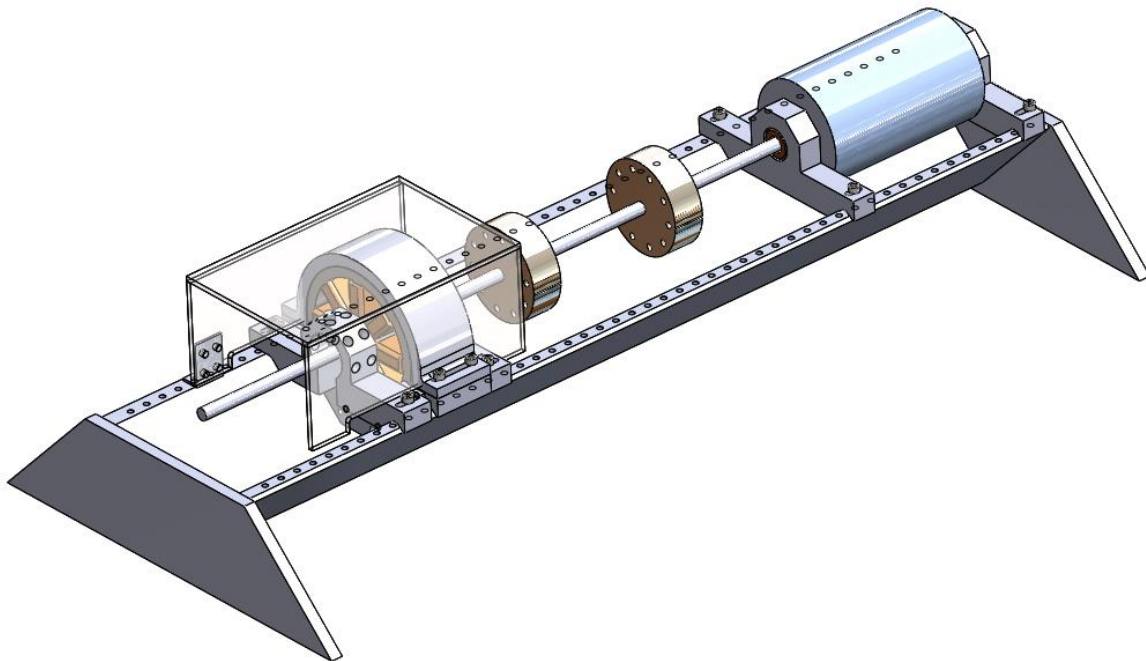
Figure 7.1. AMB assembly mounted to existing rotor kit assembly.

Touchdown bushing mount

Rotor kit sensor mount

Alignment surface

Touchdown bushing
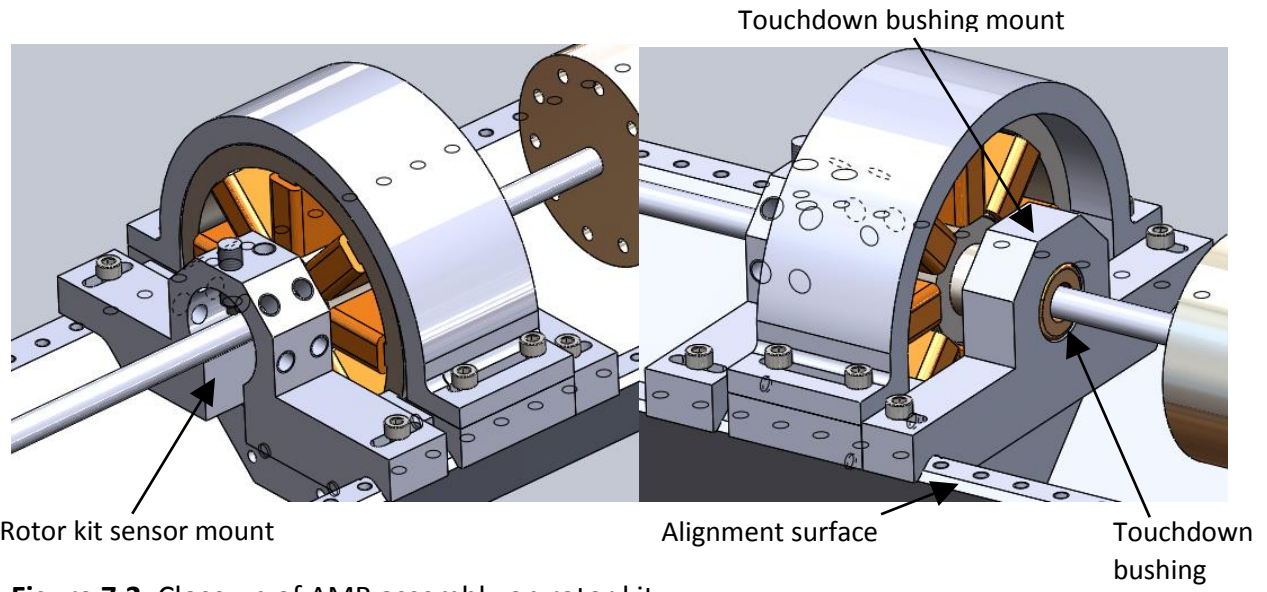
Figure 7.2. Close up of AMB assembly on rotor kit.

7.1. Stator and Rotor Mass Model

Stator

Laminated section

Trantorque

Coils

RK4 shaft
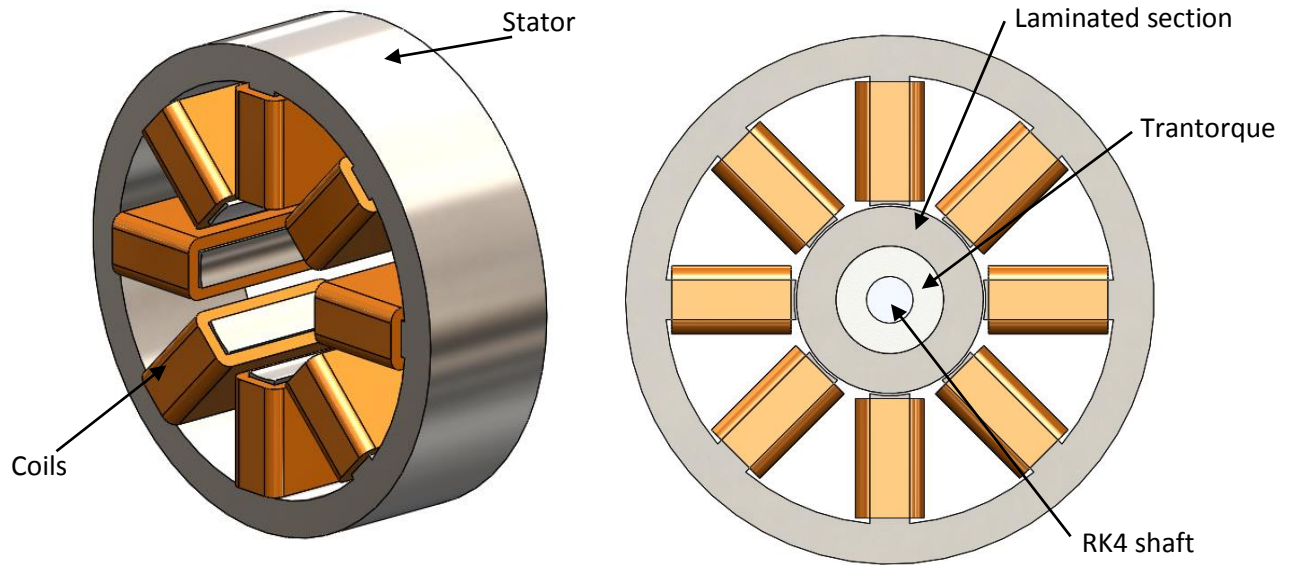
Figure 6.3. *Left:* Stator CAD without rotor. *Right:* Stator CAD with rotor.

7.2. Stator Case Model

The designed stator mounting case consists of three pieces. The primary load bearing support piece is depicted on in **Figure 7.4**. The necessary complexity and tight tolerances required that it be CNC machined.   6061-T6 aluminum was chosen for the material due to its low cost, easiness to machine, and paramagnetic nature. The method for mounting the case to the V-shaped channel of the rotor kit mimicked the existing bushing and sensor mounts. The surfaces below the right slot in the figure align with two 45° chamfers on the edge of the rotor kit channel so that, when screwed onto the channel, the face of the part aligns itself perpendicularly to the shaft. The stator was designed to rest on two flat edges rather than one curved edge in order to allow for easier shimming of the case should the case or stator not fall within tolerance. Tolerances much better than 0.001" or 0.025mm are difficult to achieve with the CNC mills in Mustang 60.
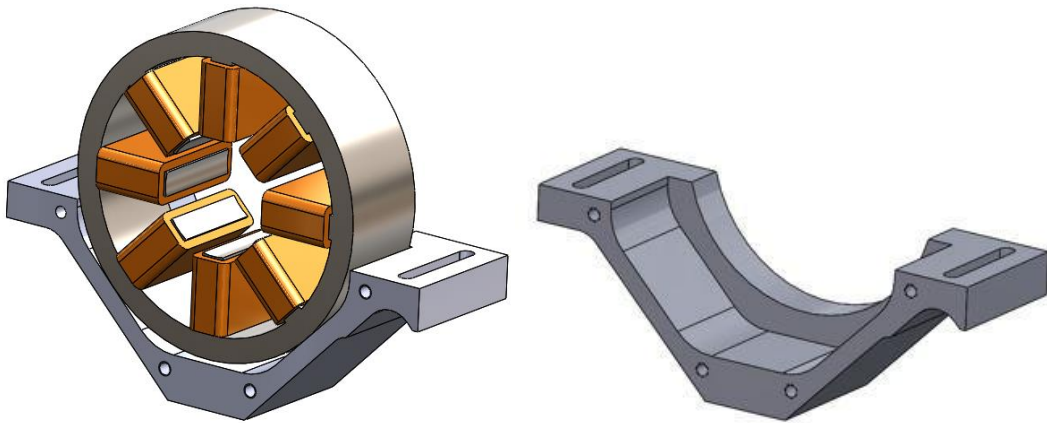
Figure 7.4. Stator case with stator *(Left)* and without stator *(Right)*.

The rib with the semicircular cutout provides stiffness to the case while serving as an alignment surface when installing the stator and clamping it in place with the case cover. Case deflection was raised as a concern due to the small air gap between the rotor outer diameter and stator inner diameter. Deflection in the case could change the stator's position relative to the rotor and compromise the air gap. This concern was addressed with a simple analysis where the case "base" (**Figures 7.5-7.6**) and "cover plate" were modeled together as a straight beam with an equivalent area moment of inertia. The case's dimensions were simplified and flattened as shown in the figures below to determine an equivalent length for the straight beam of 150mm.
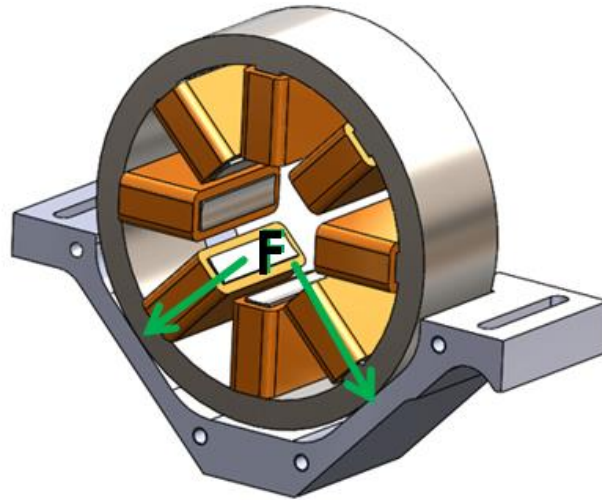
Figure 7.5. The combined force from the stator's weight and the max magnetic force acts normally at the stator/case interface. Note that while the cover plate has been excluded here for clarity, its area moment of inertia was included in the beam deflection equation.
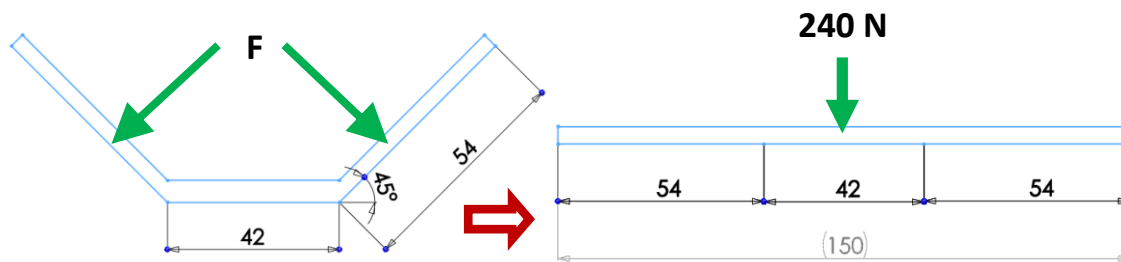
Figure 7.6. The case geometry was simplified and then flattened into a straight beam. The forces were then resolved into a single downward force of 240 N, which is equal to the combined force from the weight of the stator and the max generated magnetic force.

Using the appropriate equation from Shigley's Machine Design text [12], $\delta = \frac{-Fl^3}{48EI}$, the maximum deflection, δ, was calculated to be 0.012mm which constitutes 2.4% of the nominal 0.5mm air gap. While this uses the max design load with a safety factor of 3, this load is not very realistic as the safety factor of 3 was chosen more as a way of accounting for losses when calculating the bias current than due to uncertainty regarding the force required to levitate the rotor. A more realistic max load is about 80 N. This produced a deflection of 0.004mm or 0.8% of the air gap. This was expected to have little impact on the control of the system, and so the case design was considered acceptable.

The case's cover plate holds the stator in place axially while the "roof" secures it vertically. With the bolts that hold down the roof and attach the case to the rotor table not

tightened down, there was designed to be a 0.5mm gap between the interface of the base and roof of the case. This was to ensure contact between the top of the stator and inside of the roof. These two parts were also CNC machined from 6061-T6.
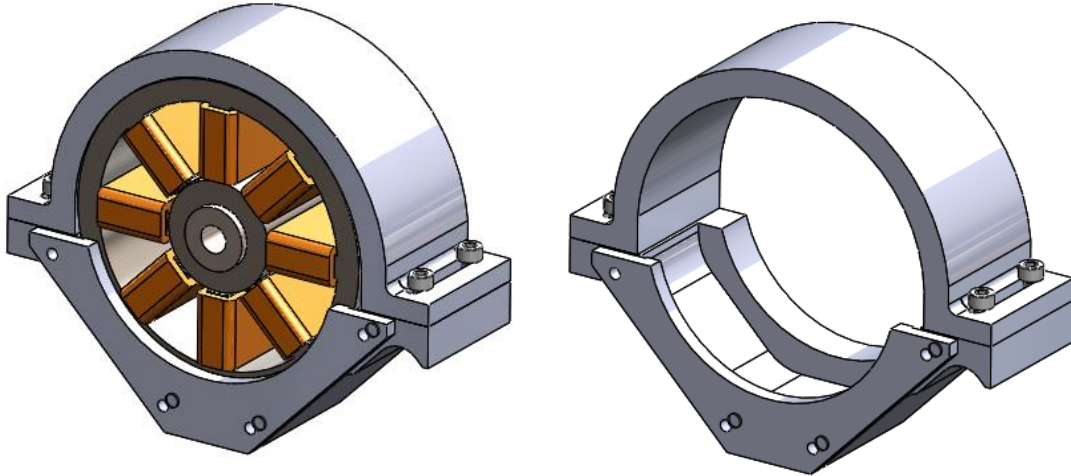
Figure 7.7. 3 part stator case with and without stator and rotor.

7.3. Control System Model

The control schematics by Schweitzer [2] and the independent Republic of Korea group [3] were followed in developing the closed-loop system for one electromagnetic actuator. There are a total of four actuators surrounding the rotor: two opposing actuators in the y-axis and two opposing actuators in the x-axis. Each actuator is supplied a current by a power amplifier to induce a magnetic force on the suspended rotor. The power amplifier supplies a bias current (1.2 Amps) that is set at startup. The current will increase or decrease according to the rotor's position relative to the shaft's center position inside the AMB. A constant tug-of-war results as each actuator attracts the rotor to the center position while the rotor's rotational speed is increased. Two proximity sensors, one for each axis, measure the rotor's position and provide feedback to the system's controller. Deviations from the center position are corrected by PID control. The corrected signal is then fed back into the amplifier, providing an up-to-date current magnitude.
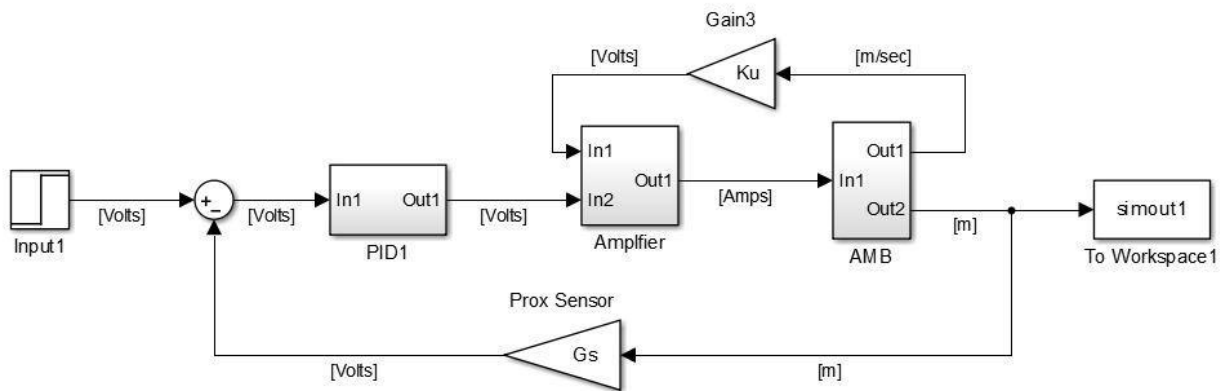
Figure 7.8. Control block diagram of one actuator with voltage input and displacement feedback.

The power amplifier output signal (input to AMB) would ideally follow the input signal to the power amplifier, however this is not the case. The inductance of the AMB coil will resist any sudden changes in current, therefore fast current changes can only be achieved by a suitably high internal amplifier voltage [2]. The coil current now becomes part of the system dynamics, making it important to model the electrical properties of the bearing magnet and power amplifier (inductance, reluctance, etc.). In this case, the power amplifier must be modeled as voltage-to-voltage and not voltage-to-current. **Figure 7.9** provides a general model of a trans-conductance operational amplifier (voltage controlled) that will be incorporated into the AMB system.
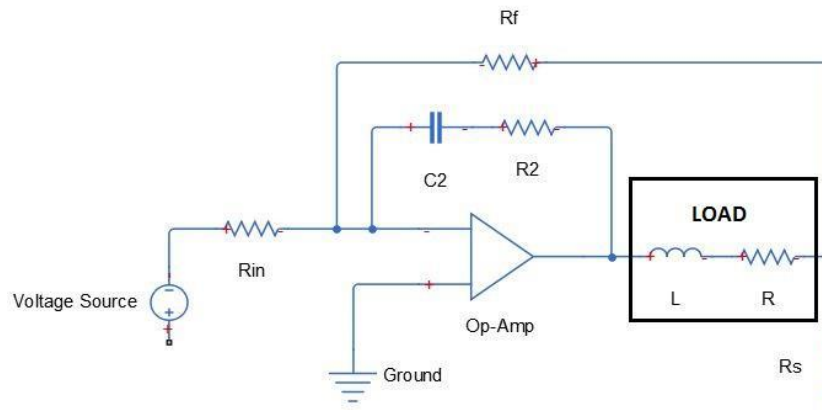
Figure 7.9. Voltage controlled power amplifier with output current and actuator load (L + R).

Current from the power amplifier will be supplied to the AMB actuator. Stiffness coefficients Ki and Ks due to the input current and position of the rotor, respectively, are seen

in **Figure 7.10**. The mass used to model the AMB is the effective mass of the rotor at the bearing location. The motion induced voltage coefficient Ku is fed back to the power amplifier. A disturbance representing forces caused by mass imbalance of the rotor system is input into the model. The greater the disturbance, the larger the current perturbation needed to bring the rotor back to center.
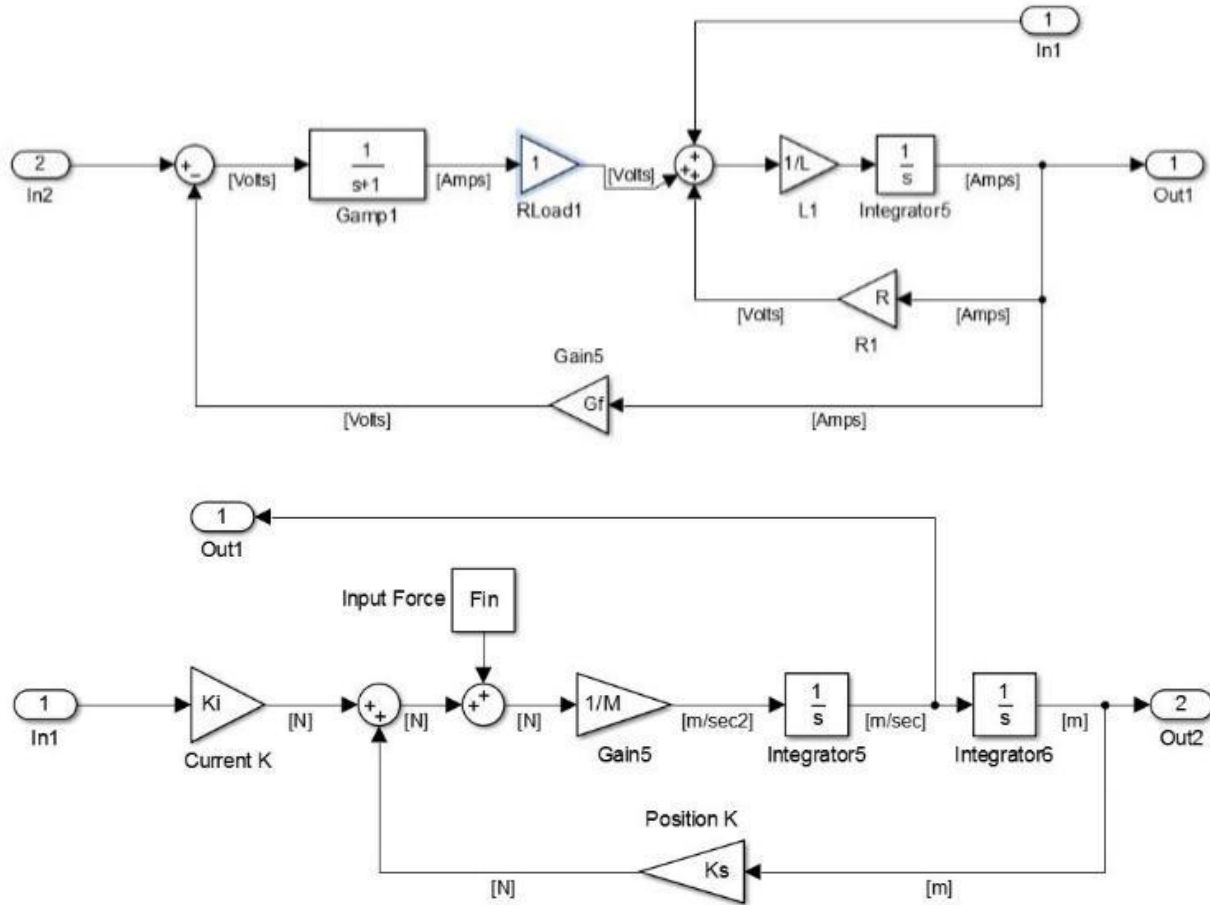
Figure 7.10. *Top:* Control block diagram of voltage controlled operational amplifier. *Bottom:* Control block diagram of AMB with current/force input and force disturbance from rotor imbalance.

The following equation is used to describe the total voltage output of the amplifier that includes the system dynamics [2]:

$$u = Ri + L\frac{di}{dt} + k_u\frac{dx}{dt}$$

The coefficient k_u describes the dynamic stiffness induced by the rotor mass within the AMB while R and L are the resistance and inductance of the actuator copper wiring, respectively. The largest contributor to voltage potential across each actuator is the coil inductance, L. Schweitzer [2] and Yoon [7] estimate this value with the following equation:

$$L = \frac{\mu o * A * N^2}{2 * so}$$

This equation produced a coil inductance of 35.3 mH for our system. With a maximum slew rate of 2140 A/sec, the corresponding inductance requires 75.6 V. Based on these two results, 80 V provided a safe estimate of the maximum voltage required for each actuator. Dr. Lei Zhu, senior electrical engineer for Solar Turbines Inc.'s magnetic bearing team, estimated the required voltage to be as much as 100 V due to the expected inductance and unanticipated iron losses in our actuators. As a general estimate, Zhu uses the following equations for required voltage capacity:

$$V = L * w_1 * i_1 + L * w_2 * i_2 + L * w_4 * i_4$$

The "w's" represent the first, second, and fourth harmonics of the operating speed, in rad/sec. The "i's" represent the bias current divided into thirds over each harmonic. In this case, with a maximum bias current of 1.4 amps, $i_1 = 1$ Amp, $i_2 = 0.2$ Amps, and $i_4 = 0.2$ Amps. With an expected maximum operating speed of 10,000 rpm, this equation produces 81.4 Volts.

To avoid the issues associated with higher voltage, we reduced the maximum operating speed to 6,000 rpm. This produced an expected voltage capacity of 48.8 Volts. Anticipating additional eddy current and hysteresis losses at higher speeds, a safe design voltage capacity was set to 60-80 Volts.

8. ADAMS and MATLAB Co-Simulation

The bearings systems of **Figure 8.1** were analyzed in MSC ADAMS to determine the vibrational response of suspended masses on a flexible rotor that each have an eccentricity at different phase angles. The first system on the following page (*Left)* contains a rotor suspended by a flexible bushing and an AMB (Active Magnetic Bearing). The second system (*Right*) contains the same rotor suspended by two flexible bushings. The suspended mass location and eccentricity properties of both systems are identical. The AMB and bushings each have a defined stiffness that acts in the X and Y directions with axial stiffness and damping neglected.
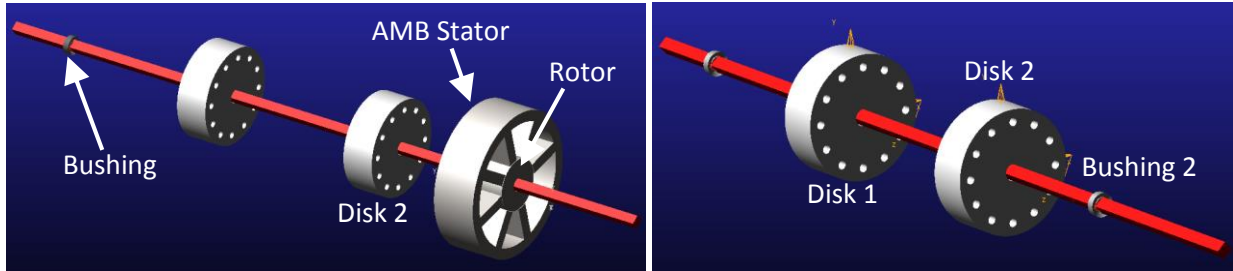
Figure 8.1. *Left:* AMB and bushing rotor system. *Right:* Two bushing system.

A co-simulation between ADAMS and MATLAB was developed for the first system containing the AMB. Relative displacement, velocity, and acceleration state variables were defined inside the AMB that linked the stator to the center of mass of the "Rotor Mass" element. These state variables characterized the AMB plant used in a MATLAB/Simulink AMB system block diagram. Simulation results from MATLAB were imported back into ADAMS and viewed as an animation during post-processing where the model could be further tuned and adjusted.

SOLIDWORKS models of the steel rotor balancing disks and a shaft were created to match the dimensions of the RK4 rotor kit components. Both disks were identical with an OD = 0.075 m, ID = 0.01 m, and Thickness = 0.025 m. They also contained 12 cut holes with Diameter = 0.005 m used for adding balancing weights. The extruded steel shaft has a Length = 0.56 m and OD = 0.01 m.
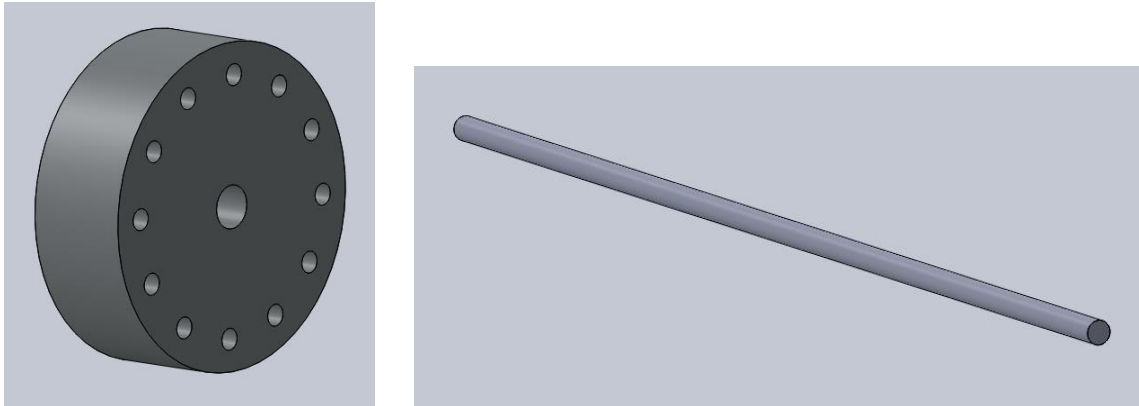
Figure 8.2. *Left:* Disk 1 and 2 used in AMB system, OD = .075m, Thickness = 0.025m. *Right:* Steel shaft used in AMB system, length 0.56 m.

8.1. ADAMS Model Setup

The AMB assembly from SOLIDWORKS was directly imported into ADAMS. Once in ADAMS, the assembly was translated to line up along the global Z axis. Before any simulations

could be performed, a few system parameters were defined that include material definitions, constraints, applied motion, force and stiffness interactions, and state variables. **Figure 8.3** shows the locations of the AMB/bushing and suspended disks.
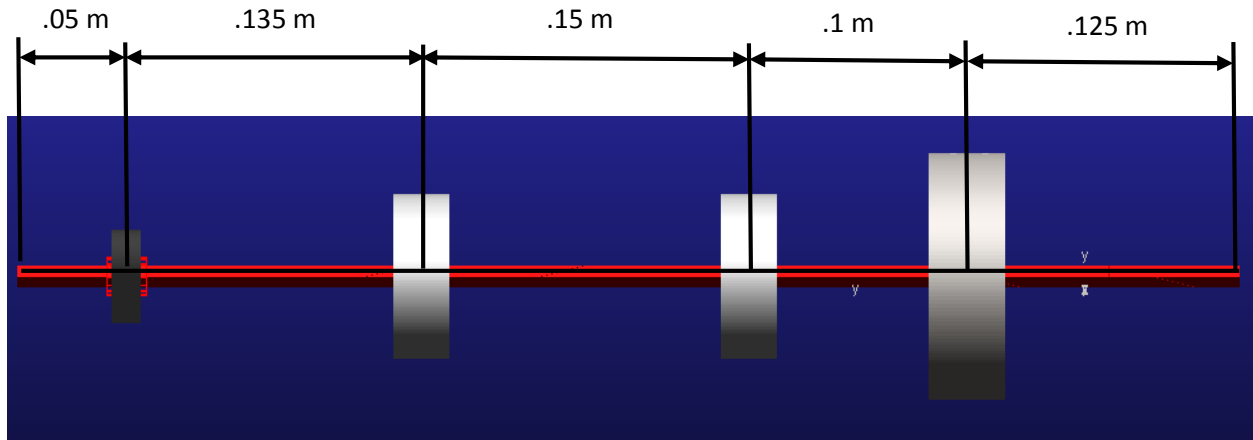
Figure 8.3. Dimensioned ADAMS assembly starting from the left: Bushing, Disk 1, Disk 2, and AMB with Rotor Mass.

All pieces of the AMB/bushing and two bushing assembly are made of steel with Young's Modulus E = 2.07e5 N/mm², density ρ = 7.8e-6 kg/mm³, and Poisson's Ratio ν = 0.29. The material properties become very important when converting the steel shaft from a rigid to flexible body.

8.2. Constraints and Applied Motion

The steel shaft had 152 nodes and 36 modes of vibration after being modeled as a flexible body. The length of the shaft was aligned with the global Z axis and the center of its diameter was set to 0 m in the global X and Y coordinates. Bearings in each model were locked to the ground and the flexible shaft and had zero translational or rotational degrees of freedom. The bushings in each model were given a lateral stiffness of 2e05 N/m with 0 N/m axial stiffness and negligible damping. Each disk's center of mass was offset from its geometric center to induce an eccentricity. Disk 1's eccentricity in global coordinates is 0 m (X direction) and 0 m (Y direction). Disk 2's eccentricity in global coordinates is 4e-4 m (X direction) and 0 m (Y direction). The center of mass of each disk was locked to the flexible shaft and has zero translational and rotational degrees of freedom.

A rotational joint was added to both models that connected the inboard of the flexible shaft to the ground. A rotational motion with initial velocity of 4 rev/sec (240 rpm) and

acceleration of 35 rev/sec/sec was applied for a time interval 5 seconds, ramping the shaft to a final velocity of 27 rev/sec (1620 rpm).

8.3. Force and Stiffness Interactions

Applied current to the AMB stator induces an attractive force and a negative stiffness on the levitated rotor mass. Both effects tend to pull the levitated mass to each actuator during operation. **Figure 8.4** shows the force and stiffness interactions acting on the center of mass of the levitated rotor mass in the global X and Y directions. Four points attached to ground were placed on the inner diameter of the stator along the X and Y axes and halfway between the poles of each actuator. The other end of the force and stiffness interactions on the laminated rotor mass were then anchored to these points.

The stiffness is a constant term defined by the bias current, nominal air gap, and number of coils on each actuator. With a bias current of 1.2 Amps, the stiffness was 3.08e5 N/m. The applied forces in the X and Y directions vary with time during the simulation and depend on the location of the rotor center mass with respect to the 4 inner stator grounded points.
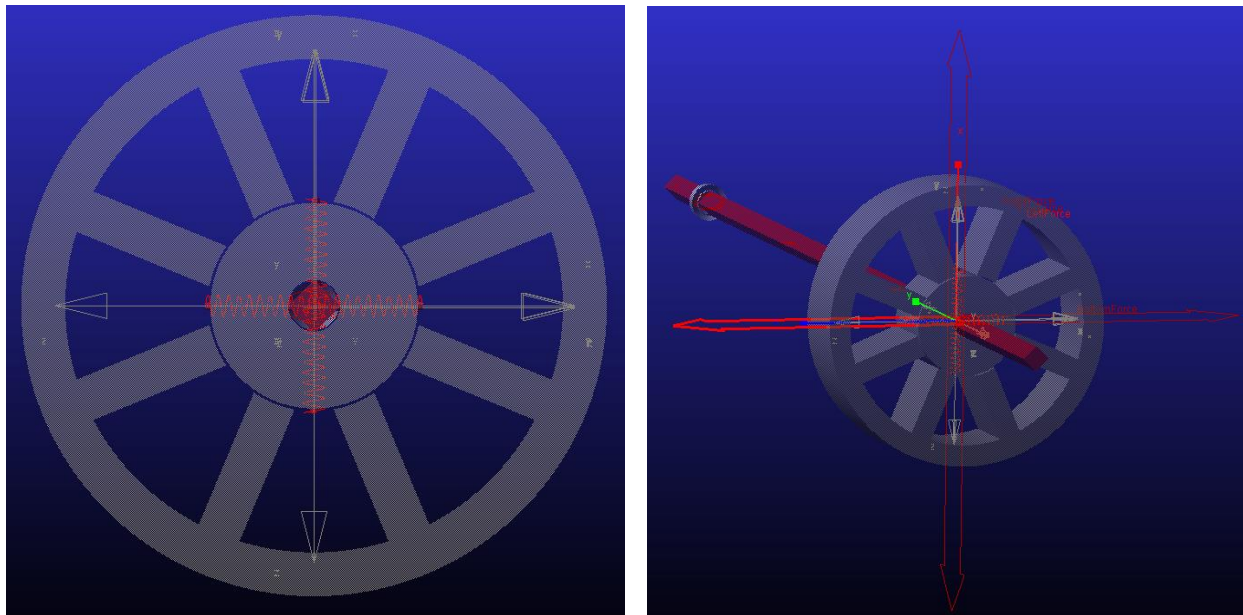
Figure 8.4. *Left:* AMB profile with springs setup in ± X and Y directions (-Ks). *Right:* Springs with Force function defined in the ± X and Y directions.

8.4. State Variables

Relative displacement, velocity, and acceleration between the center of mass of the rotor and grounded stator points were defined. These variables were used in a MATLAB/Simulink block diagram to accurately describe the motion of the suspended rotor system during simulation. **Figure 8.5** shows where the exported ADAMS plant is implemented in the AMB system transfer function.
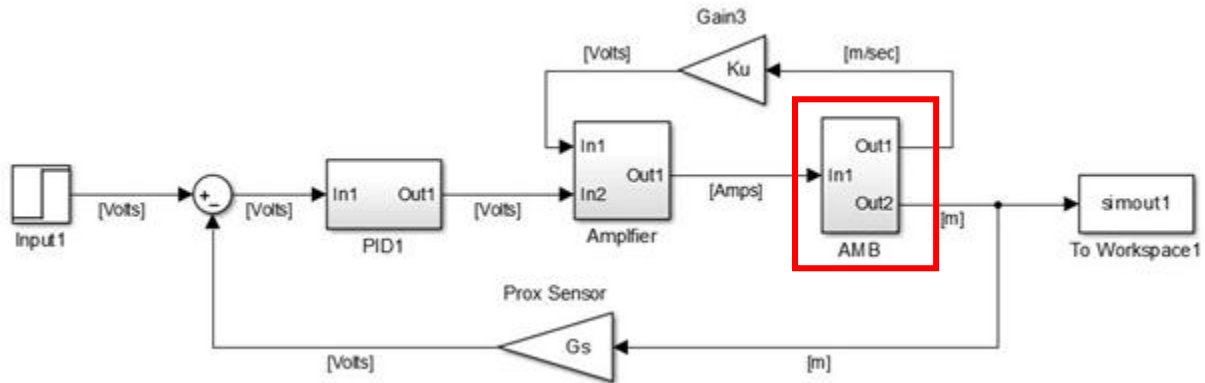
Figure 8.5. AMB system block diagram for 1 actuator with highlighted block of the imported ADAMS rotor plant.

8.5. MATLAB Modeling

The force and stiffness calculations were conducted in a separate MATLAB function file. **Table 8.1** provides a list of AMB parameters, calculated stiffness terms, and amplifier circuit parameters (servo drive parameters). The generated magnetic force (F_mag) varies during the simulation as the rotor mass' distance varies from each actuator. The Ks term is implemented in the ADAMS model before the system plant is exported into Simulink. The Ku term was neglected for this initial analysis but may be implemented if the amplifier dynamics are considered in future analyses. The Ki term is a current stiffness that becomes the generated magnetic force of each actuator when multiplied by the applied current.

```
%% Gamp
C2 = RB*CB*RD*L;
C1 = RD*L + RD*RB*CB*R;
C0 = RD*R;
D2 = RA*L*CB*RD;
D1 = CB*(RA*RB*RC+RA*RD*(R+RC)-RB*RD^2);
D0 = RA*RC - RD^2;
```
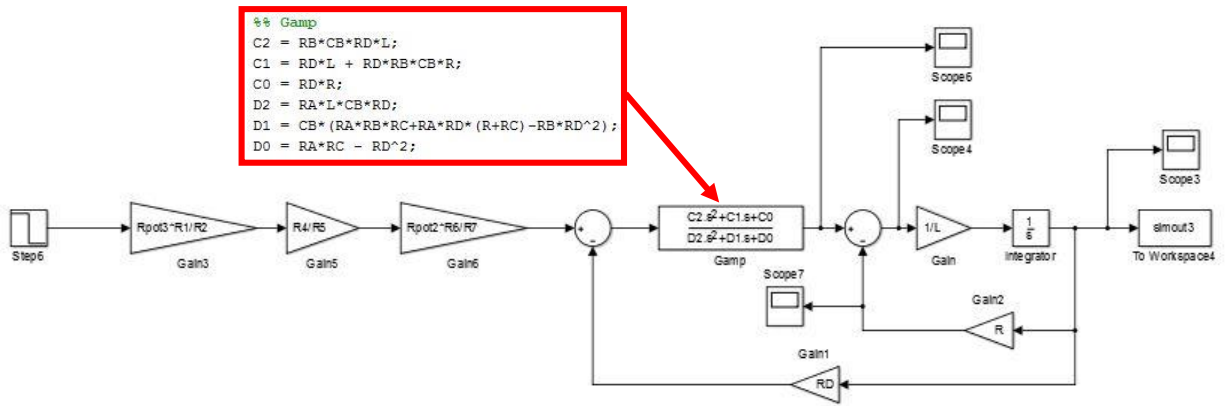
Figure 8.6. Block diagram of Servo Drive implemented in the MATLAB/ADAMS co-simulation. Included is the G_{amp} block with corresponding parameters for each of the circuit components.

Table 8.1. AMB and Servo Drive (Amplifier) parameters implemented in MATLAB function file.

Bias Current (Amps)	1.1671
# Coils (Per Actuator)	300
g_o (m)	5.00E-04
mu_o (Perm_Air)	1.25664E-06
Eps (Leakage + Fringing)	0.8
A_act (m2)	2.98E-04
Gap Factor	1.05E+00
A_gap (m2)	3.12E-04
F_mag (N)	3.67E+01
Ki (N/Amp)	1.32E+02
Ks (N/m)	3.08E+05
Ku (V/m/sec)	1.32E+02

```
%% Ampflifier Circuit Parameters
R1 = 50000;
R2 = 20000;
R4 = 5000;
R5 = 10000;
R6 = 500000;
R7 = 500000;
C7 = .05e-06;
Rpot3 = 10000; %6000
Rpot2 = 1;
RA = 10000; %[Ohm]
% Ra = 20000; %[Ohm] max without Rb
% Rb = 10; %[Ohm] 500,000 max
% RB = Ra*Rb/(Ra+Rb); %[Ohm]
RB = 20000; %[Ohm]
Ca = 0.01e-06; %[F]
Cb = 0.00e-06; %[F] 0.8e-06, 0
CB = Ca + Cb; %[F]
L = 35.3e-03; %[H] with N=150, L=8-10 mH
R = 0.641; %[Ohm]
RC = 10000; %[Ohm] 1, 10000
RD = 10000; %[Ohm]
```

8.6. Simulation Procedure and Results

Once all the state variables were fully defined, the control plant developed in ADAMS was exported into MATLAB/Simulink (**Figure 8.7**). This became a Control_Plant_##.m file that had to be run in MATLAB. The next step was to run "adams_sys" in the command prompt for the .m file to become a Simulink block diagram (**Figure 8.7**). This new block diagram was then copied and inserted into a developed AMB system block diagram that was then run from a

separate .m file containing the complete system parameters. A complete AMB system block diagram can be viewed in **Appendix G**.
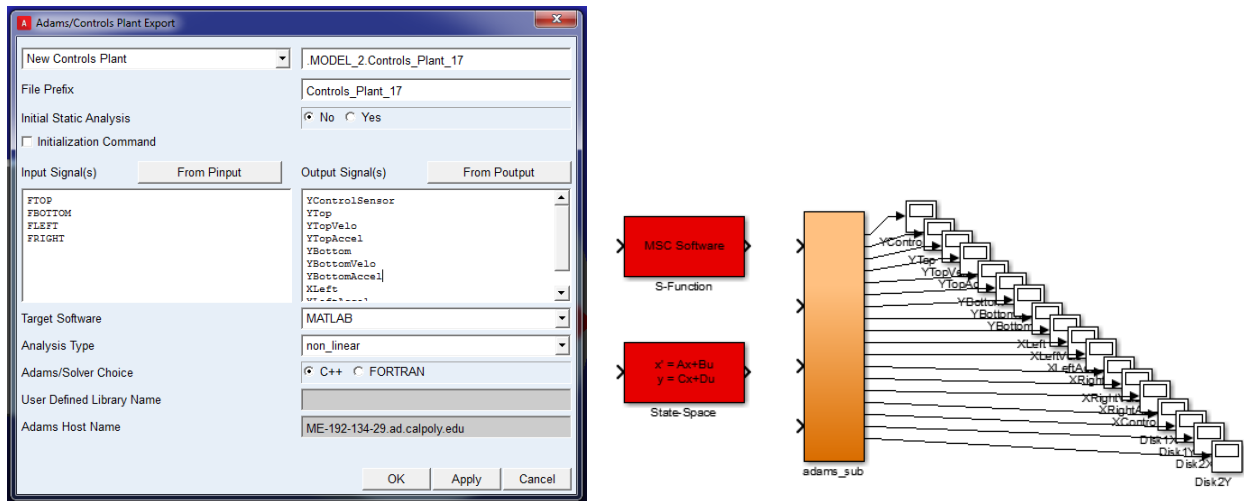
Figure 8.7. *Left:* Exported plant variables from ADAMS model to MATLAB/Simulink models. *Right:* ADAMS control plant Simulink block diagram.

Displacement in the X and Y directions for Disks 1 and 2 as well as force vectors inside of the AMB Stator and Bushing 2 were captured in **Figures 8.8-8.11.** Both simulations ran the same length of time with identical eccentricity, velocity, and acceleration parameters. The two suspended disks were also locked at the same locations.

The bushing/bushing model shows an increase in amplitude for Disk 1 as the rotor approaches the first natural frequency. Interestingly, the AMB/bushing model shows an almost constant displacement at Disk 1. Displacement values for Disk 2 in the bushing/bushing model remain constant at a lower amplitude than a constant amplitude displacement in the AMB/bushing model. Both Disks 1 and 2 hold the same displacement in the AMB/Bushing model.

As can be expected, the reaction forces experienced by the bearings increases as the rotational speed increases with time. The bushing/bushing model shows a maximum force = 27 N (**Figure 8.10**) after 5 seconds. This value supports previous analyses (two-plane superposition model) used to predict expected loads while sizing the AMB actuators. The forces captured by the AMB Stator in the X and Y directions are the applied forces to each actuator. The forces remain close to constant magnitude (153-155 N) however their oscillating frequency increases with the shaft's rotation speed.
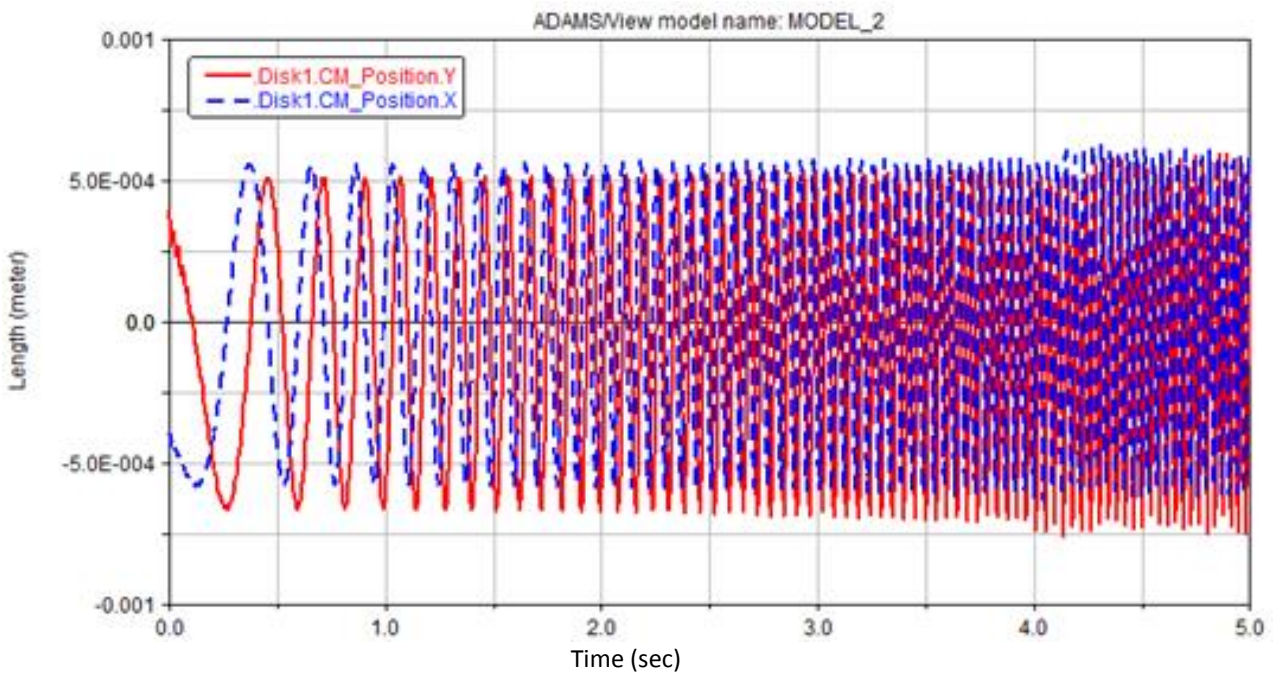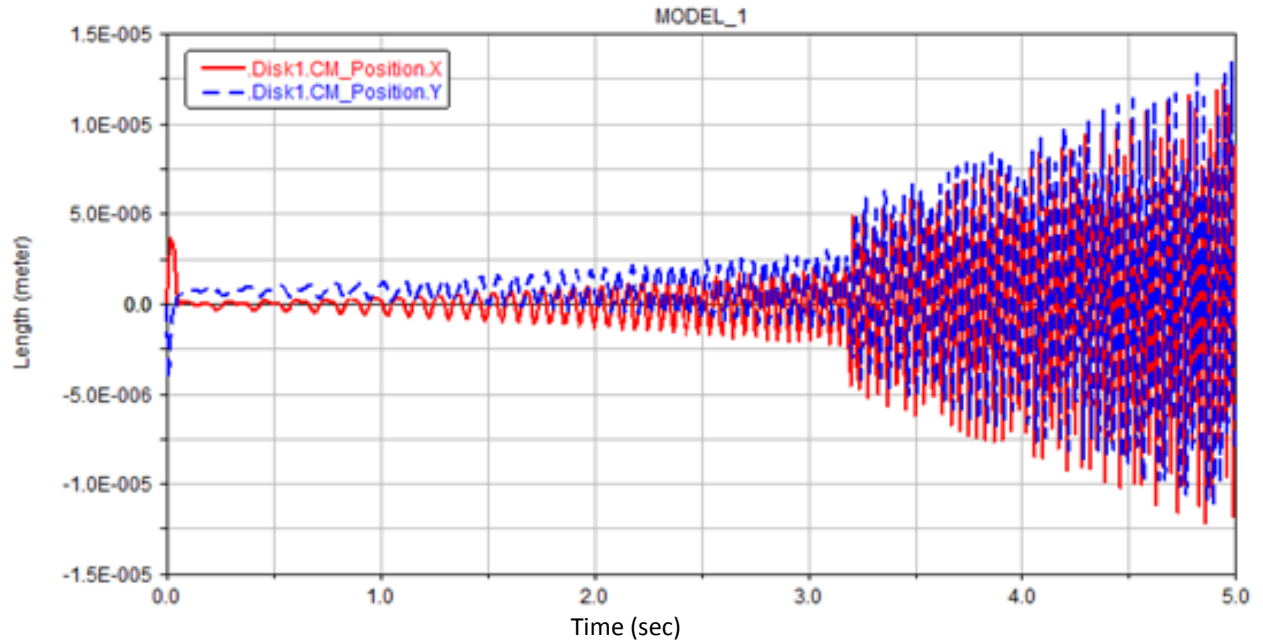
Figure 8.8. *Top:* Disk 1 X and Y displacement in Two Bushing Model. *Bottom:* Disk 1 X and Y displacement in AMB and Bushing Model.

44
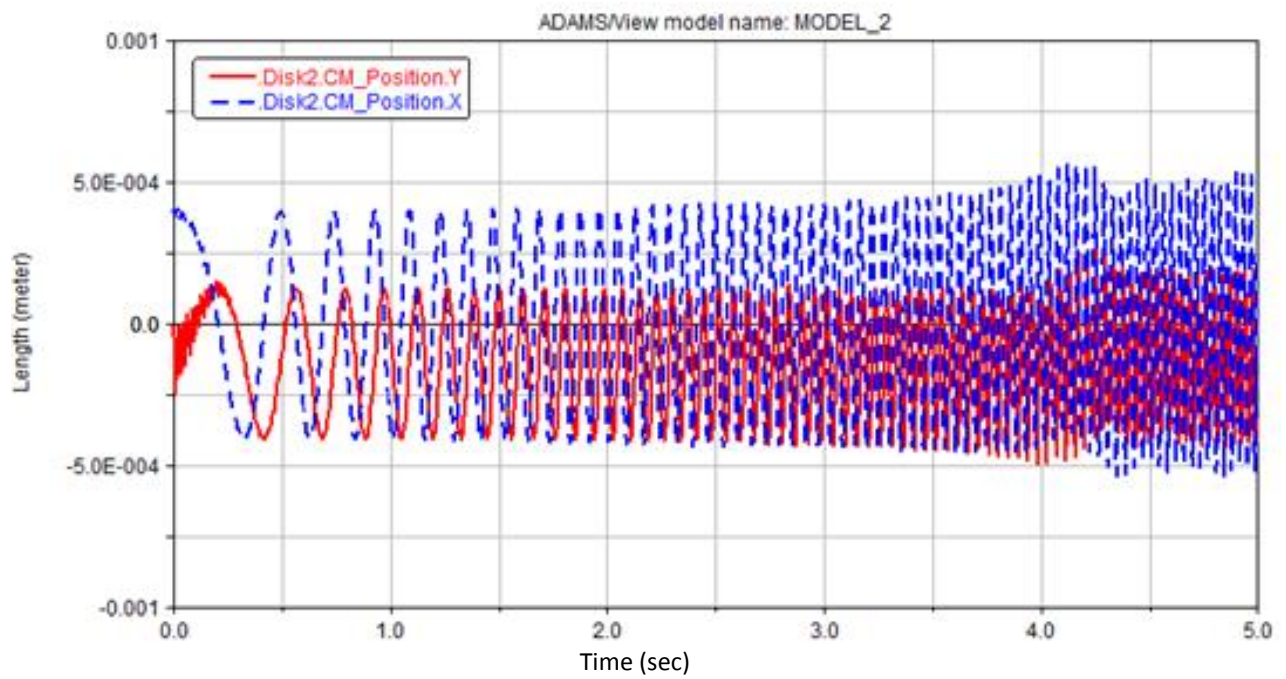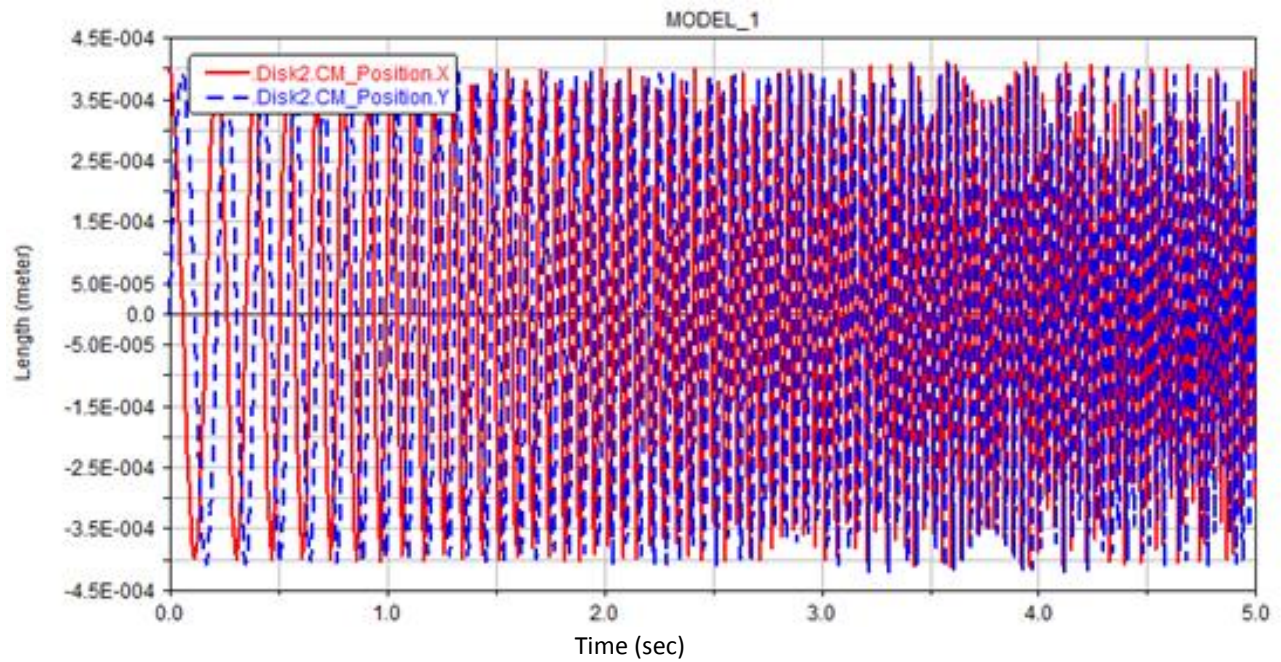
Figure 8.9. *Top:* Disk 2 X and Y displacement in AMB and Bushing Model. *Bottom:* Disk 2 X and Y displacement in Two Bushing Model.
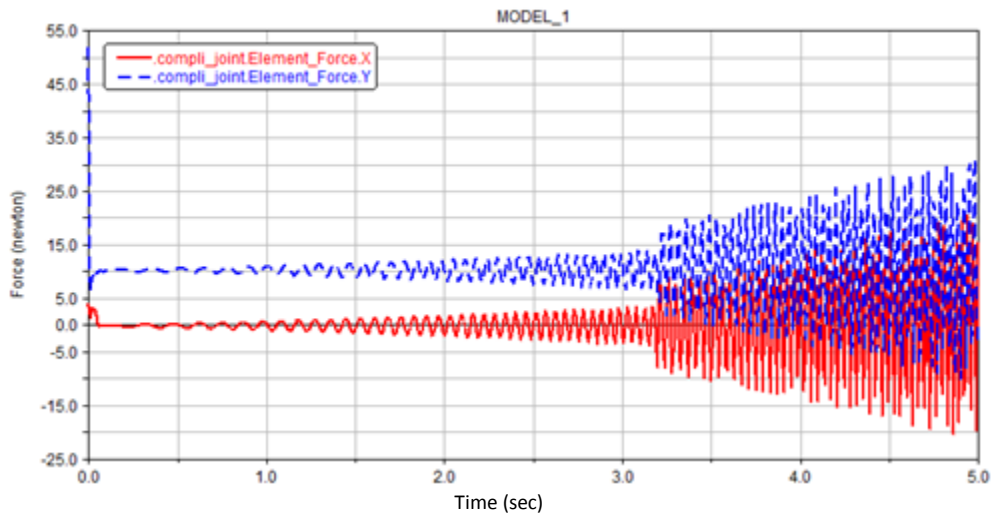
Figure 8.10. X and Y force components in Bushing 2 of the Two Bushing Model.
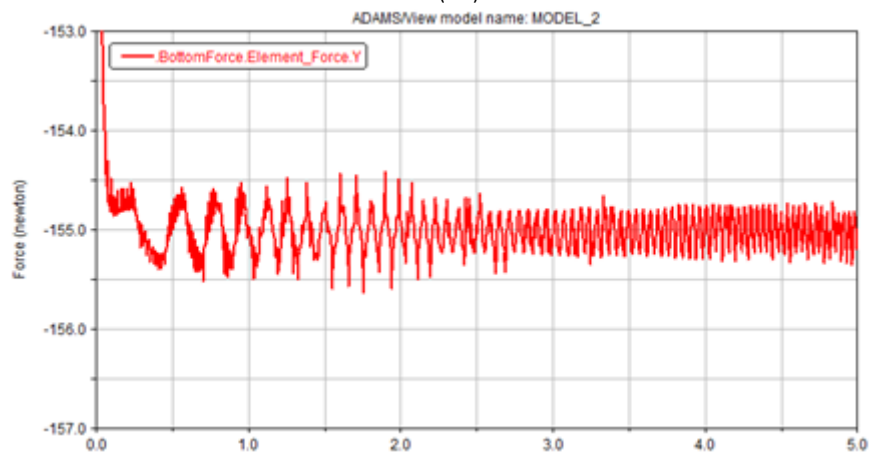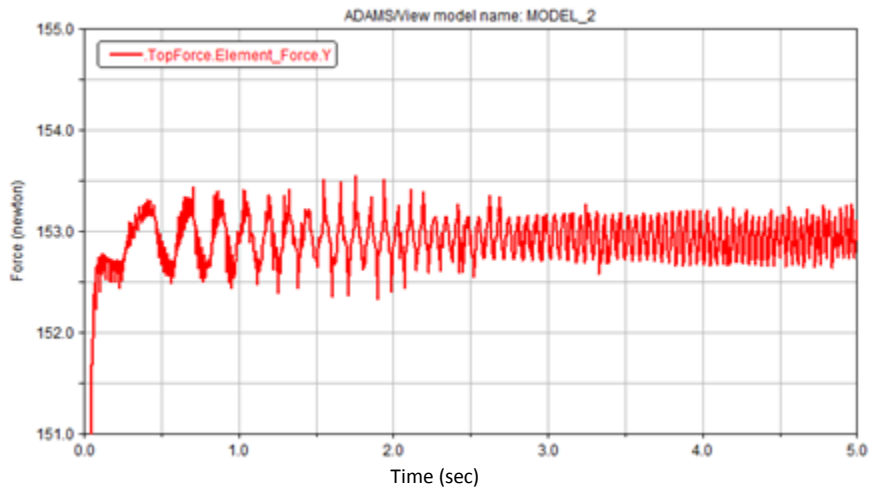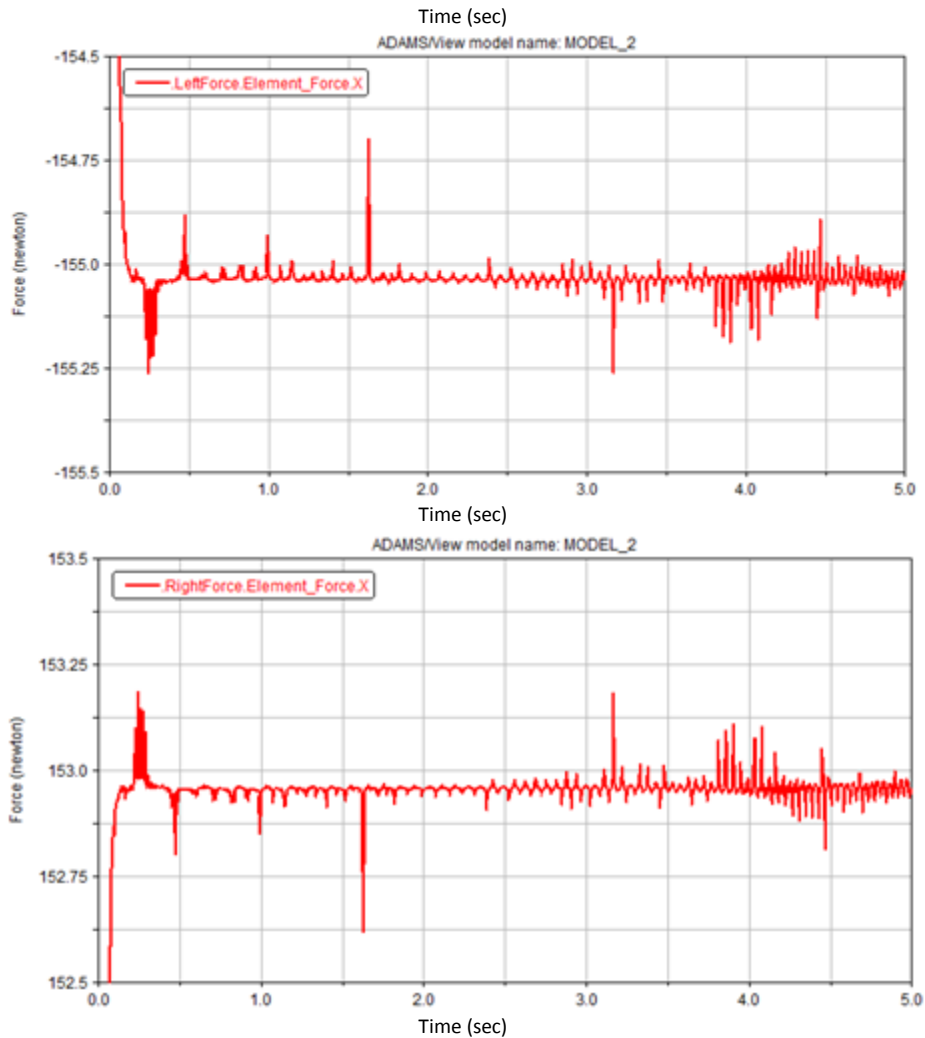
Figure 8.11. Force components from Top, Bottom, Left, and Right Actuators respectively (top to bottom).

The co-simulation results provide the user some extremely useful insight into modeling a system when designing a controller. This model can be adjusted for different rotor system parameters (location of the disks, eccentricities, length of rotor, etc.). Additionally, poles and zeros created when adding filtering can be added to the system in either ADAMS or MATLAB. Filters can remove outside disturbances (noise) and affect time delay after discretizing the system for digital control.

9. Design Hazard Identification

Several potential hazards will exist during the testing and operation of the AMB assembly and must be addressed with precaution and care. Hazards include 1) electrical wiring, 2) mechanical parts in motion at high speeds, and 3) heat dissipation by the iron core. The upper limit of voltage consumption by the system is estimated to be 60-80V. Proper wiring (placement and covering) of all wires will be critical for use by the user as well as limiting any parasitic losses during operation. The typical rotor operating speed will be between 300-3000 rpm. Anytime a rotor is spinning there will be the chance of metal fragmentation from contact interference or the assembly not being properly fastened and secured. During operation the iron core and casing will increase in temperature due to generated heat by the copper coils on each actuator. An operating time limit with corresponding running speeds may have to be defined to maintain lower levels of heat generation.

A detailed Failure Modes and Effects Analysis (FMEA) is provided in **Appendix H**. This explains all of the foreseen potential failures, their resulting outcome, and design constraints implemented for prevention. Severity and occurrence scales have also been provided to show the likelihood of these events as well as how great the consequences.

10. Bill of Materials

BILL OF MATERIALS			
Magnetic/Mechanical Hardware			
Part(s)	Quantity	Unit Price	Total Line Price
Laminated stator and rotor from Polaris Laser Laminations	1	$1,671	$1,671
CNC 6061-T6 Stator case	3 pieces	$100 for aluminum stock $100 for tooling $306 for CNC machining labor	$506
AWG 22 Magnet wire	2	$18 per 507 ft spool	$36
Coil sleeve (3D printed ABS)	8	No purchase	$0
Touchdown Bushing	1	No purchase	$0
M5 x 0.8, 35 long screws	1	$9 for box of 10	$9
M5 x 0.8, 16 long screws	1	$5 for box of 50	$5

Trantorque couplers	2	No purchase	$0
Sheet metal shims	NA	No purchase	$0
Magnetic/Mechanical Subtotal:			$2,227
Electronics Hardware			
Part(s)	Quantity	Unit Price	Total Line Price
GE Proximity sensors	2	No purchase	$0
GE Sensor amplifiers	2	No purchase	$0
National Instruments Real-Time Control Board (cRIO-9063)	1	$1,246	$1,246
Advanced Motion Control 12A8 Servo Drives	4	$206.25	$825
Advanced Motion Control PS16L72 Power Supply	1	$650	$650
AWG 18 Shielded electrical wire (gray)	1	$60 per 50 ft reel	$60
PC fan	2	No purchase	$0
Hall effect sensor and ±15V power supply	1	No purchase	$0
Electrical enclosure/box	1	$150	$150
Electronics Subtotal:			$2,781
Total Cost:			$5,008

11. Electronics Assembly

In addition to the stator and casing, the AMB assembly consists of actuating and sensing electronic hardware. Typical hardware includes: 1) a digital control board that receives and analyzes data, then implements C code converted from MATLAB or LabVIEW, 2) power amplifiers that convert controller signals into desired magnetic actuator currents, and 3) sensors that convert physical displacements into voltages.

11.1. Controller and Data Acquisition Board

In selecting a controller and data acquisition system, it was decided to combine both of these functions into one compact solution for convenience and feasibility. National Instruments gave us the best option in meeting our needs by providing a high sampling rate

(>10kHz), programmable logic that interfaces with a computer real-time simulation (LabVIEW), and an adequate number of input and output terminals (8 and 4, respectively). The selected unit is the NI cRIO-9063 (**Figure 11.1**) which combines a dual-core processor, reconfigurable FPGA (Field Programmable Gate Array), and four slots for input/output modules all in one chassis. The system is well suited for advanced embedded control and monitoring applications, thus perfect for operating an AMB. LabVIEW can be used to create, debug, and deploy logic to the onboard FPGA. **Table 11.1** provides the specifications for the chassis setup. Two NI 9215 modules were used to meet the requirement of 8 input channels. For more information regarding these units, please consult the National Instruments website [18,19,20].

Figure 11.1. *Left:* NI 9063 FPGA Controller. *Right:* NI 9215 Simultaneous ± 10V Analog Input and NI 9263 ± 10V Analog Output.

Table 11.1. Specifications of NI instrumentation for control and analog input/output voltage signals.

NI 9063 FPGA Controller		NI 9215 Analog Input		NI 9263 Analog Output	
Architecture	ARM Cotex-A9	Signal Levels	± 10V	Signal Levels	± 10V
Speed	667 MHz	Channels	4 Differential	Channels	4
Cores	2	Sample Rate	100kS/s/ch	Sample Rate	100kS/s/ch
Flash Reboot Endurance	100,000 cycles	Simultaneous	Yes	Simultaneous	Yes
Nonvolatile Memory	512 MB	Resolution	16-Bit	Resolution	16-Bit
Volatile Memory	256 MB	Connectivity	BNC	Connectivity	Spring-Terminal
Accuracy	5 ppm				
Voltage Input Range	9-30 VDC				
Max Power Input	18 Watts				

11.2. Power Amplifiers and Power Supply

Voltage signals ranging from ±3.3V to ± 10V are sent from the controller into the power amplifier. The amplifier's parameters are sized according to a desired output, in this case 1-2 Amps. The chosen amplifier and power supply are shown in **Figure 11.2**. The performance characteristics of the servo drives are shown in **Table 11.2**. More information regarding the specifications of these units can be found on the Advanced Motion Controls website [12,13].
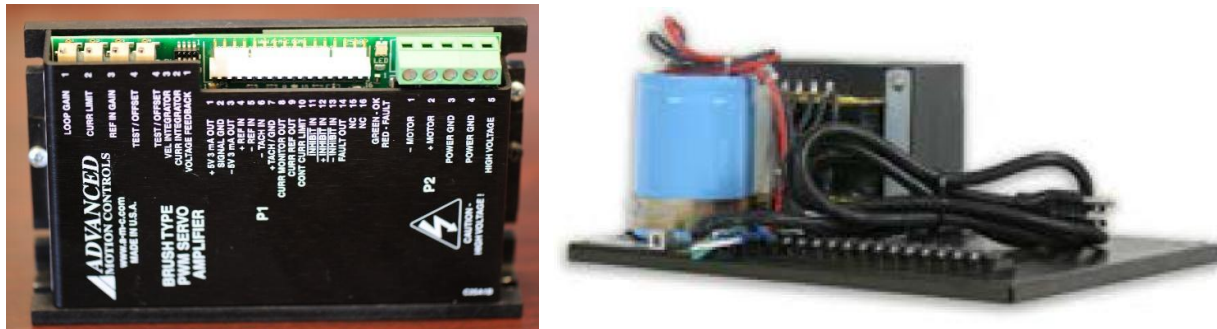
Figure 11.2. *(Left)* 12A8 analog servo drive. *(Right)* PS16L72 power supply.

Table 11.2. Advanced Motion Controls servo drive and power supply specifications

AMC 12A8 Analog Servo Drive		AMC PS30A Power Supply	
Peak Current	12 A	DC Output Voltage	72 VDC
Max Continuous Current	6 A	Output Current	11 A
Supply Voltage	20-80 VDC	Output Power	800 W
Command Voltage	± 10 V		
Switching Frequency	36 kHz		

11.3. Proximity Sensor and Amplifier

An important element to the performance of the overall AMB system is the type of proximity sensor used to measure the placement of the rotor during operation. This sensor must remain contact free during operation and provide accurate position feedback to the controller. Typical sensors used in industry for this application are eddy current sensors. Eddy

current sensors work by creating a rapidly oscillating current in a sensing coil at the end of the probe. This creates an alternating magnetic field that induces eddy currents in the target material being measured. The induced magnetic field in the opposing target material will then resist the field being generated by the probe, thus providing a measurable voltage potential.

Important parameters to consider when selecting a sensor include: 1) measuring range, 2) linearity, 3) sensitivity, 4) resolution, and 5) frequency range. Measuring range is the range of distances that can be measured for which the relationship between distance and sensor output voltage remains linear. Linearity shows to what extent the measured quantity will deviate from a linear relationship between the measured quantity (mm) and output signal (V). Sensitivity indicates the ratio of the output signal over the quantity to be measured (increment size, V/mm). Resolution indicates how much useful signal from the output can be distinguished from noise produced by the sensor amplifier system. Finally, frequency range indicates the bandwidth of the linear frequency response that has a cut-off frequency of -3 dB. The chosen proximity sensor assembly is Bently's 3300 XL 8mm. Assembly and specifications are shown in **Figure 11.3**.

Bently 3300 XL Proximity Sensor System	
Recommended Gap	1.27 mm
Sensitivity	200mV/mil
Deviation from Straight Line (DSL)	<+/-.025 mm
Frequency Range (-3 dB)	0-10kHz
Linear Range	0.25-2.3 mm
Power Supply	-17.5 to -26 VDC

Figure 11.3. Bently 3300 XL 8mm sensor probe and amplifier assembly with specifications

Bently's product is common in industry today for monitoring rotating machinery and is currently being used in the vibrations lab. Dr. Lei Zhu recommended a probe sensitivity of around 5 mV for a magnetic bearing application. Bently's probe sensitivity is slightly worse at 7.84 mV, but this is still very good for the size and scope of our system. More product information can be found Bently's website [21].

12. Manufacturing and Construction
12.1. Laminated Stator and Rotor Mass

Since Cal Poly does not possess the expertise to perform effective bonding of the laminations, these services were sourced externally. Quotes from several vendors were received. The least expensive quote was $1,650, from Polaris Laser Laminations based in Chicago (the most expensive being over $13,000 from Wingard Hydroblanking in Baltimore). Since Polaris Laser Laminations (PLL) also claimed the shortest lead time of about 4 weeks from purchase completion to shipment, it was chosen as the manufacturer for the rotor and stator. Gauge 29 (0.014") sheets of M19 silicon steel were laser cut and bonded together to make the parts. Each layer of glue between the laminations is on the order of 0.0002" thick. Gauge 29 is a typical gauge found in motor laminations and should be suitable for the speeds we expect to operate at.

The received parts were within the ± 0.001" requested and no post-cutting operations were necessary. Quotes for lamination thicknesses between 0.025" and 0.014" were requested from PLL. There was a marginal increase in cost for thinner laminations, but thinner laminations reduce losses due to eddy current formation in the material. This allows for higher operating speeds to be attained.   In accordance to advice given by Dr. Zhu of Solar Turbines, the laminated rotor's axial length was slightly increased past the axial length of the stator to account for fringing, or the spreading of the magnetic field within the air gap as the flux transitions from the stator steel to the rotor steel.
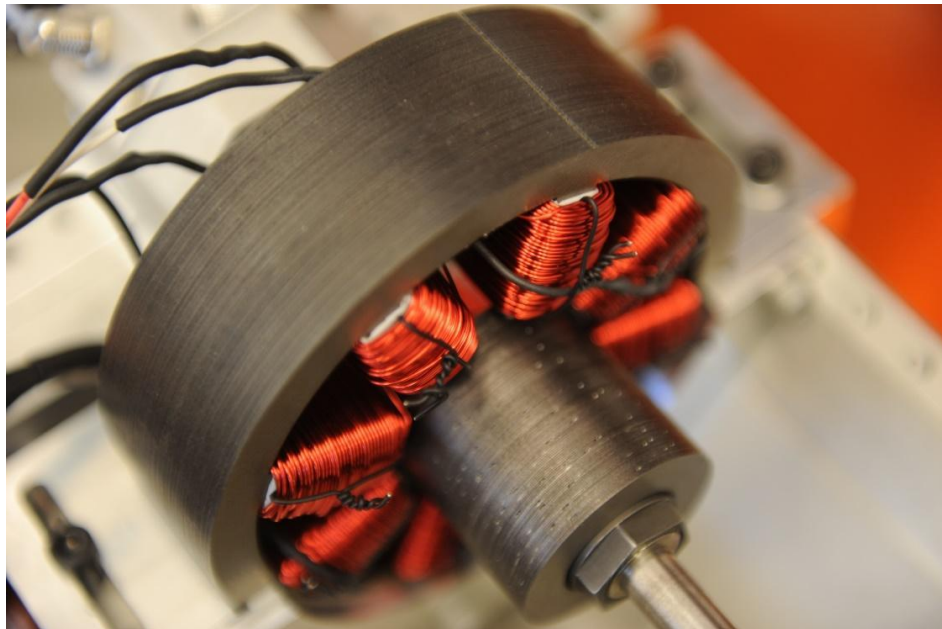
Figure 12.1. Laminated rotor and stator. Rotor withdrawn from operating position for image.

Appropriately sized Tran-torque connectors from the Bently fluid film bearing kit were used to connect the laminated rotor to the existing 10 mm rotor shaft. At the time of their incorporation into the design, it was not realized that their steel construction would introduce undesirable flux leakage from the laminated rotor into the Tran-torques. These were retained in the final project as it was determined that their ease of use and ability to keep the laminated rotor attached to the shaft with limited eccentricity was more valuable than the losses they produced. Changing the shaft/laminated rotor coupling to a paramagnetic material like aluminum would be a prudent future upgrade for when attempting to attain higher operating speeds.

12.2. Stator Case

The stator case was CNC milled by Alec Bialek (Cal Poly shop tech) from 6061-T6 aluminum. Aluminum was used to prevent magnetic flux from leaking into the case since aluminum has a much lower magnetic permeability than steel. The first "base" of the case had to be scrapped due to a mistake when dimensioning the CAD file. It was assumed that the 10 mm rotor kit shaft rests centered between the threaded holes on either side of the V-channel. As was revealed, there is actually a slight asymmetry and the shaft is biased to one side. This was too big of an error to correct through shimming.

**Figure 12.2.** CNC milled, aluminum, stator case components.

Even with the revised base, shims were necessary to properly align the stator around the rotor. These consisted of nonmagnetic strips of sheet metal inserted between the 45° contact surfaces of the base and the bottom of the stator. An unfortunate result of the shimming was that it produced a gap separating the contact surfaces between the roof and the base. While additional shims could be manufactured to fill this gap, it was found that the built in interference at the base/cover plate interface provided adequate clamping force to prevent any motion of the stator during operation. For this reason, the roof was left off of the finished project.

Upon further inspection of the roof component, one may notice several differences between the physical part and the CAD model. First, the outside top of the roof is flat as a result of purchasing the wrong sized stock material. Second, there is a cutout section at the top of the roof. This was manually milled out to remove a large defect from the CNC cutting process that resulted when a shell mill cutter came unscrewed and blew apart the top of the part. Despite these defects, the roof should perform satisfactorily if it is deemed necessary during future tests.

12.3. Magnetic Coils

Producing the eight magnetic coils for the stator poles presented a challenge. The coils had to be wound tightly and with an accurate number of windings (150 for each pole) for the best performance. It was initially hypothesized that the lathe in Mustang 60 could be used to wind the coils by attaching a spool of magnet wire to the auto-feed and running the machine at low RPM. A fixture for holding the coil sleeve could be held in the chuck. While this would likely have produced tight, precise windings, accurately counting the number of windings would have been challenging. However, a quick YouTube search yielded several examples of individuals easily producing tight windings by hand with a cordless drill with speed modulation.
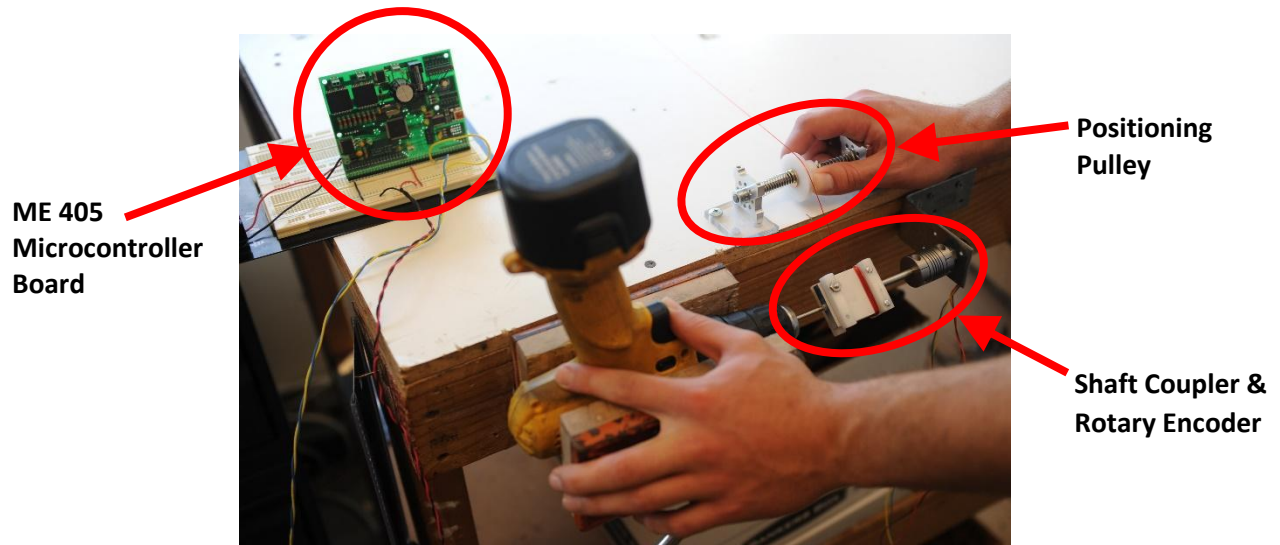
Figure 12.3. Construction setup of stator pole magnetic windings.

This simple setup was combined with a rotary encoder attached to the spinning coil sleeve mold. This mold consisted of a rectangular piece of aluminum of the same cross section as a stator pole with a 6-32 through tap at the rotational axis. This allowed a spindle to be threaded into one end for the drill chuck to hold and a quarter inch shaft to be attached to the other end. This shaft was connected to the rotary encoder via a shaft coupler to account for the misalignment in the system. The encoder was held by a bracket mounted to the mechatronics lab workbench. The drill was held inverted in the vice of the workbench. The magnet wire reel was mounted to the back of the workbench via a pair of brackets, a wooden dowel, and a friction plate to keep tension on the wire. A pulley with an adjustable position was mounted at the front of the workbench near the encoder bracket. Springs on either side of the pulley shaft provided a consistent starting position but also adjustability so that the user could guide each subsequent winding down the length of the mold. The encoder was wired to an ME 405 (Mechatronics) microcontroller. An existing ME 405 lab assignment was then modified to output the revolution count from the encoder on a computer monitor so that the user could keep track of the number of completed windings.
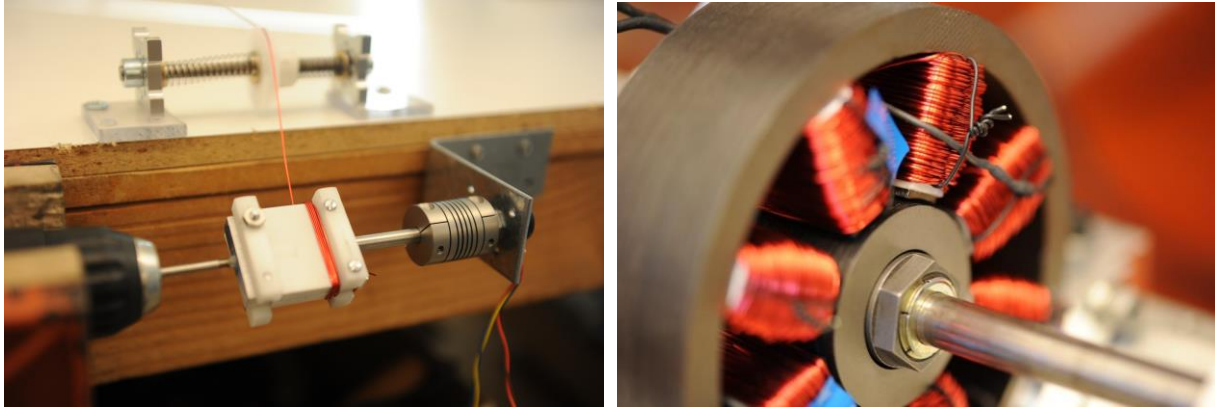
Figure 12.4. *Left:* Coil sleeve being wound with magnetic wire. *Right:* Magnetic coils fastened to the laminated stator.

Free prototype coil sleeves had been requested early in winter quarter from the Innovation Sandbox. These were intended to provide additional insulation between the stator and the coils and also allow the coils to be transferred from their mold to the poles without falling apart. The Sandbox's filament deposition printer was claimed to have the precision necessary to produce these simple parts, and, since they were printed from ABS plastic with a melting temperature of about 220°F, heat deformation was not an issue. A mechanical failure in the printer meant that those prototypes were never printed. Several wall thicknesses of the sleeve design shown below were originally requested, but time constraints and high printing demand meant that different thicknesses could not be experimented with. The first print was the final print. Fortunately, the 0.8 mm wall thickness requested proved satisfactory. What was not anticipated was the difficulty of preventing the wires from slipping off of the sleeve, particularly when winding over previous layers of wire. This difficulty produced considerable delays. Modifying the ends of the sleeve to be more like a spool would be prudent for future iterations. Delrin stops were added to the winding mold to help overcome this design flaw. It may have been prudent to seek out prototype coil manufacturers in order to reduce the time it took to produce the coils, but this would also have introduced its own challenges with no guarantee of less difficulty. Nevertheless, if future coils are to be made, it would be worth investigating.
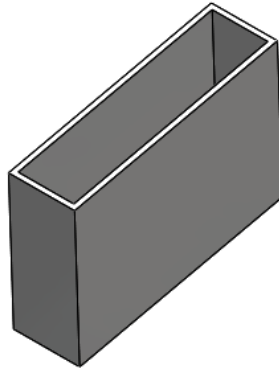
Figure 12.5. SolidWorks model of an ABS plastic coil sleeve, around which the magnet wires for one pole were wound.


12.4. RK4 Rotor System

The AMB was mounted at the outboard end of the RK4 rotor kit assembly. **Figure 12.6** illustrates the complete setup when running a two-plane mass experiment. Keeping with the existing rotor kit configuration, the rotor shaft's inboard end was connected to the drive motor via a shaft coupler and supported by a bushing. Rotor disks can be moved along the shaft to adjust the weight distribution and affect the displacement amplitudes. Additional balancing weights can be added to each rotor disk to reduce vibrations from mass eccentricities. A three-sided acrylic cover from Tap Plastics was mounted around the AMB to protect the user from metal fragments and exposure to electrical wires while providing a minimally obstructed view during operation.

The touchdown bearing and eddy current probes were mounted on the kit as close as possible to the AMB on opposite sides. The eddy current probes measure the shaft position next to the laminated rotor, rather than the laminated rotor itself. This was for convenient sensor mounting and because eddy current probes typically need factory recalibration if they are used with a different material than originally intended. The probes are offset from each other axially to prevent signal interference between the sensors. It is imperative that the touchdown bearing is as close as possible to the AMB in the event that control is lost by the actuators. The touchdown bushing was designed to "catch" the spinning rotor, preventing any damage to the stator poles by the rotor mass. To make this bushing, one of the brass, Bently kit bushings was drilled out to allow the shaft to be displaced from its center position by about half of the air gap between the stator and rotor before contacting the bushing. Using a simple, similar triangles approximation, it was assumed that the laminated rotor would not be able to contact the inside of the stator so long as the touchdown bearing block was positioned directly against the base of the stator case. Upon experimentation, it was found that this assumption

was insufficient and did not adequately take into account the flexibility of the shaft. The actuators are strong enough to pull the rotor mass against the inside of the stator. Once this has happened, the magnetic force is so strong that it is difficult to free the rotor from the stator without powering down the AMB system. You will notice that the touchdown bushing is held in place by aluminum sheet metal shims. This was to provide more rigidity to this bushing and help prevent the rotor from being pulled against the stator. The other bushings use O-rings as an interface between the brass bushing and the aluminum bushing holder. This helps deal with shaft misalignment and provides damping, but this also allows the bushing to move within the housing, which is undesirable for the touchdown bushing.

The small, controller connection box is a junction between the actuators and the servo drives supplying the current. This is attached to the RK4 base with Velcro and can be moved along the length of the rotor with the AMB for different configurations. The wire connection design from the actuator coils to the connection box is intended to allow a Hall-effect current probe to be easily inserted or removed from any of the four actuator circuits. Individual female connectors were used and surrounded by heat shrink to provide isolation from accidental arcing in the case of a voltage spike. Connections on the inside of the connection box are similarly insulated from each other with hot glue covering the solder points.
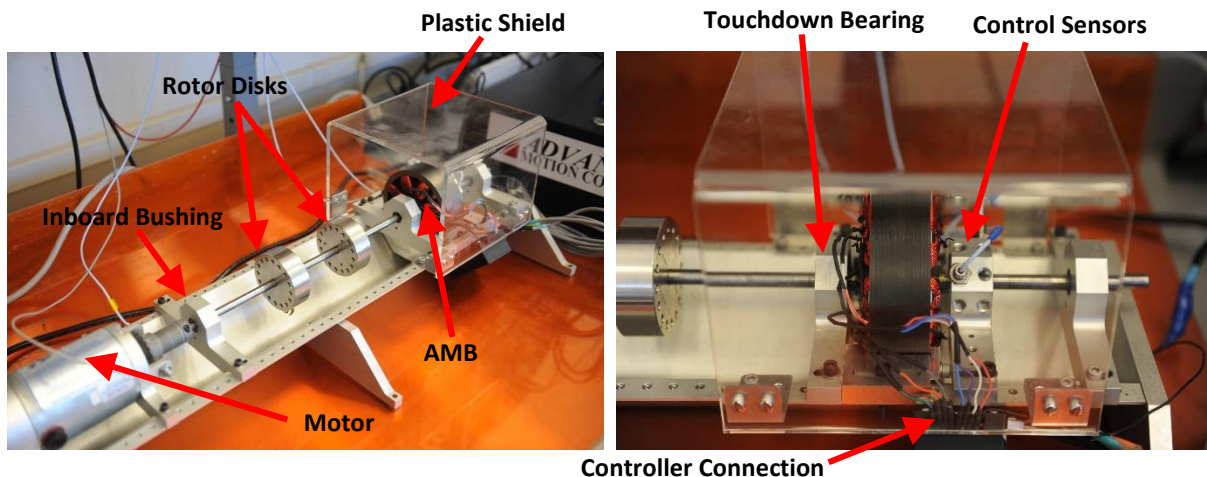
Figure 12.6. *Left:* RK4 rotor kit assembly with mounted AMB. *Right:* Profile of AMB mounted between a touchdown bearing and control sensors.

12.5. Power Electronics Enclosure

The servo drives and power supply are housed inside of an electronic enclosure set next to the RK4 rotor assembly. It has holes in the front and back for the servo drive/controller

wires and power wire, respectively. A vent and two fans were installed on the ends to allow for transient cross-flow of air if the system is operated over extended periods of time. **Figure 12.7** shows the electronic enclosure next to the RK4 system *(Left)* as well as the inside with the servo drives mounted and wired to the power supply *(Right)*. Due to the high voltage and close proximity of the electronic enclosure to the user, a lock is engaged to keep the lid of the enclosure closed during operation.

Figure 12.7. *Left:* Electronic enclosure with wire connections to the AMB and NI FPGA Controller. *Right:* Inside of electronic enclosure with the four servo drives mounted to the power supply.

13. Wire Diagrams
13.1. System Schematic

A schematic of the AMB core and electrical system is provided in **Figure 13.1**. There is an X and Y axis probe receiving displacement signals that travel to their respective amplifiers. These sensor amplifiers are being supplied -17.5/-26 VDC. The signal is then amplified and sent to the National Instruments RIO control board. This board uses a field programmable gate array (FPGA) architecture. A control program was written in LabVIEW on a PC and then loaded onto the FPGA. During operation, the control is performed entirely on the FPGA hardware. No processing power from the PC is used for control, but the FPGA does send select data points back to the visual interface on the PC so that the user can monitor its operation.
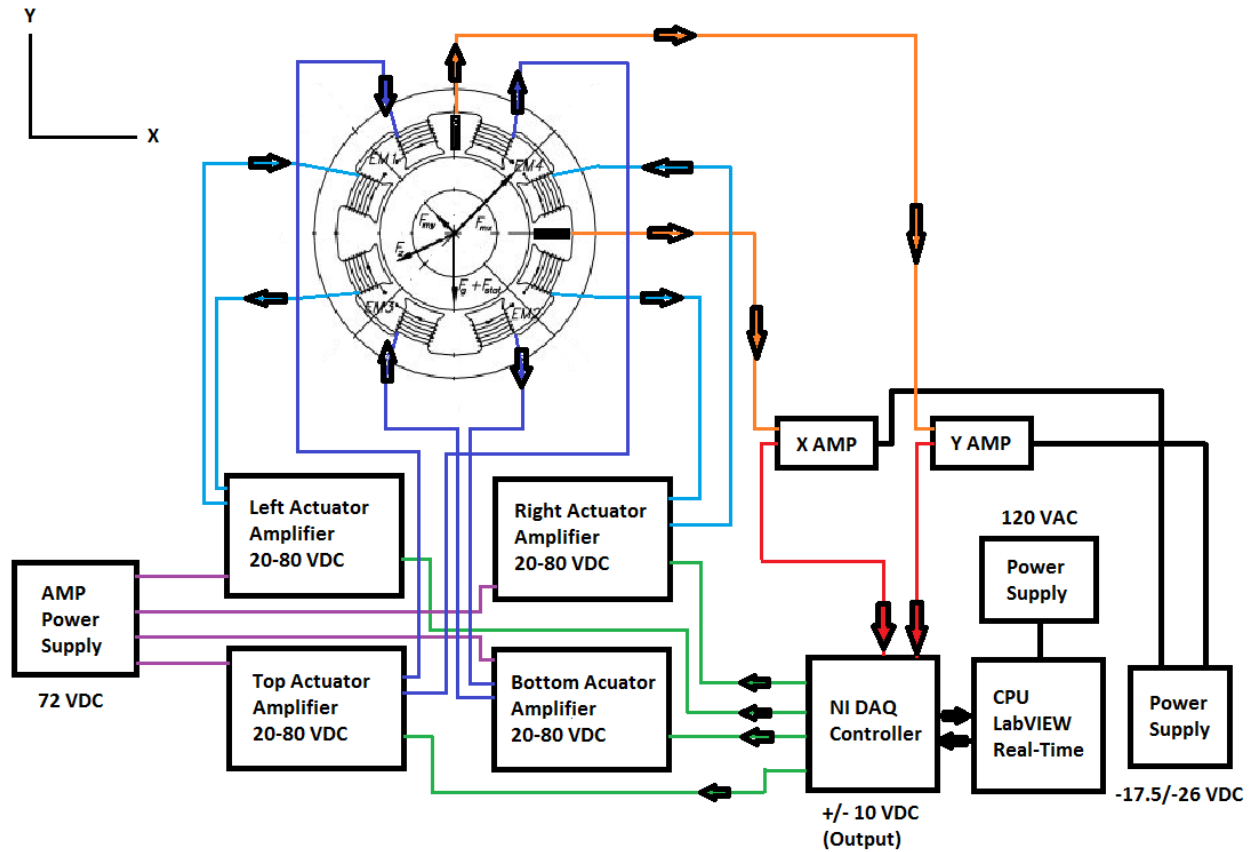
Figure 13.1. General schematic of the overall mechanical and electronic assembly with flow of current signals. (Note, the colors used in this schematic do not reflect the wiring colors of the final assembly).

13.2. Servo Drives to Power Supply

The four servo drives used to drive the AMB actuators were mounted and wired to the power supply according to the arrangement in **Figure 13.2**. As shown on the capacitor, *Red* and *Black* wires correspond with '+' and '-', or high and low voltage, respectively. Wire connections from each of the servo drives correspond with the pin call-outs in the Advanced Motion Controls product manual [12]. To conserve wire, the servo drives were grouped in pairs with the '+' and '-' leads being shared with Gage 18 two conductor wire. The shielding of each wire was grounded from one end to the power supply base. A single conductor wire connected to the power supply base is connected to the RK4 rotor kit base. This configuration of the ground wires is to ensure that everything in the system has the same common ground.

Included in **Figure 13.2** is the location and call-out of the servo drive potentiometers [12]. Each one can be adjusted with a small flathead screwdriver when the power is off. For

the purpose of this application, potentiometers 1-3 are adjusted to meet performance specifications.
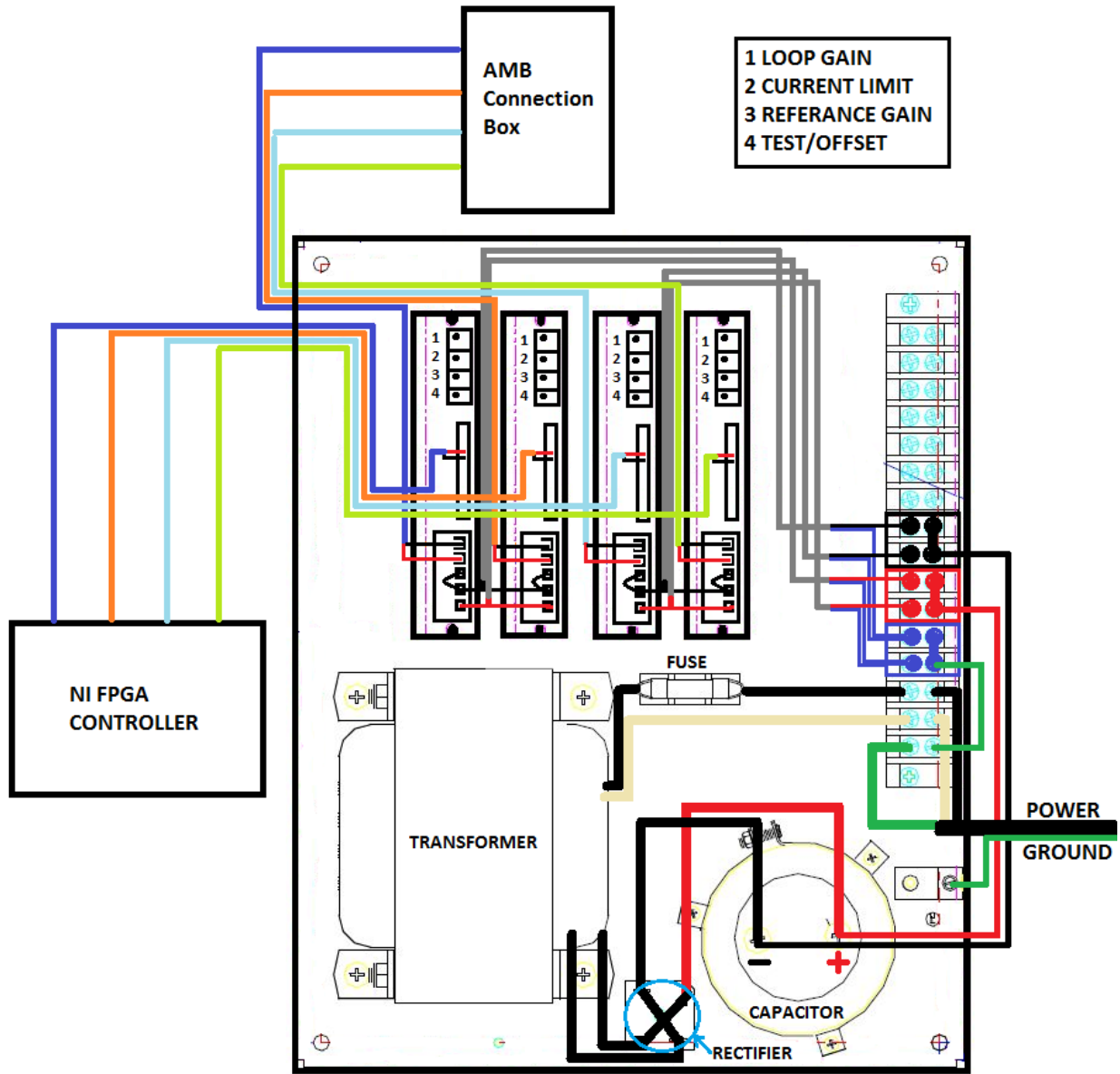
Figure 13.2. Wire diagram of servo drives to power supply with additional connections from the servo drives to the AMB Connection box and NI FPGA Controller.

13.3. Servo Drives to NI FPGA Controller

The wire connections between the servo drives and NI FPGA Controller are shown in **Figure 13.3**. The "current monitor" connections require a BNC adaptor to inject the +, - signals coming from the servo drives. The "controller to servo drive" wires do not require a special adaptor and were directly connected to the controller via spring-terminal. All of the shielded wires were ground to the controller chassis (**Figure 13.3**).

Figure 13.3. *Left:* NI FPGA Controller with 1) control signal, 2) current monitor, and 3) shield wire ground connections. *Right:* Servo drive Molex connections from the NI FPGA Controller.

13.4. Servo Drives to AMB

There are 8 wires going to and from the AMB actuators. For good organization, color-coded wires were used and paired according to the configuration of **Figure 13.4.** This view comes from the vantage point of looking down the rotor from the outboard end. The '+' and '-' labels indicate which wire is going to or from each actuator, respectively. Each color-coded pair (red/white, purple/blue, gray/orange, green/brown) are to remain together as they each represent an actuator. The wires coming from the servo drives to the connection box are color-coded according to the designated colors of **Figure 13.2.**

Figure 13.4. Color coded wire configuration of AMB

14. Servo Drive Operation

Before AMB operation, it is important to follow a safety check and proper power up procedure. The following is a condensed electronic assembly inspection checklist and tuning procedure. For more information, please refer to the **Downloadable Resources** on the Advanced Motion Controls website [12,13,14,15,16,17].

14.1. General Inspection

1) Shielded cables must be used for all interconnect cables to the drive and the shield of the cable must be grounded at the closest ground point with the least amount of resistance.
2) The motor chassis, controller chassis, power supply chassis, and analog servo drive chassis must be grounded to the closest ground point with the least amount of resistance
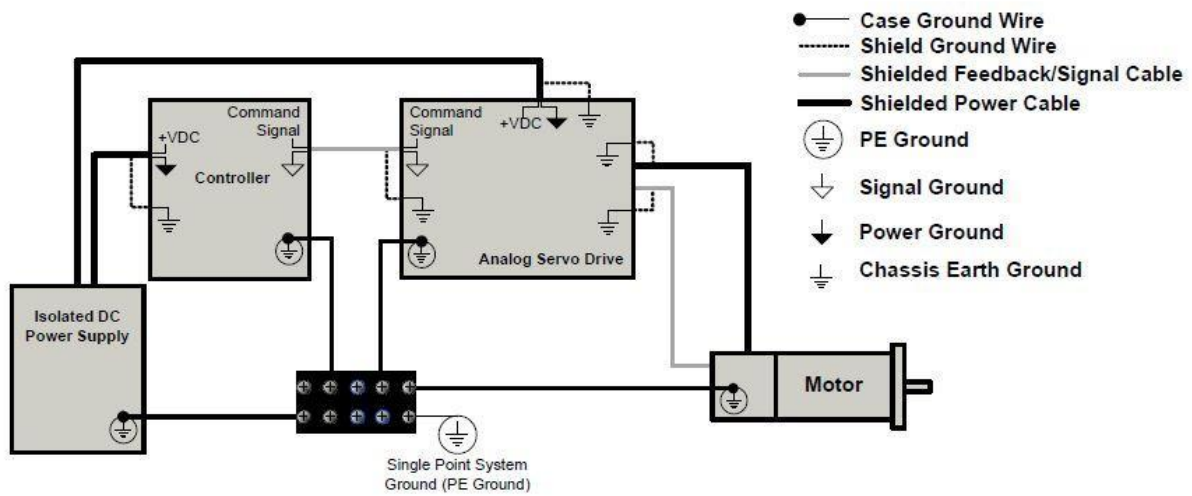
Figure 14.1. System grounding [12].

3) The drive must be mounted in such a manner that the connectors and exposed printed circuit board are not accessible to be touched by personnel when the product is in operation.

4) A Fair Rite model 0443167251 round suppression core must be fitted to the low level signal interconnect cables to prevent pickup from external RF fields.

5) Run separate power supply leads to each drive directly from the power supply filter capacitor. Never "daisy-chain" any power or DC common connections, use a "stator"-connection instead.
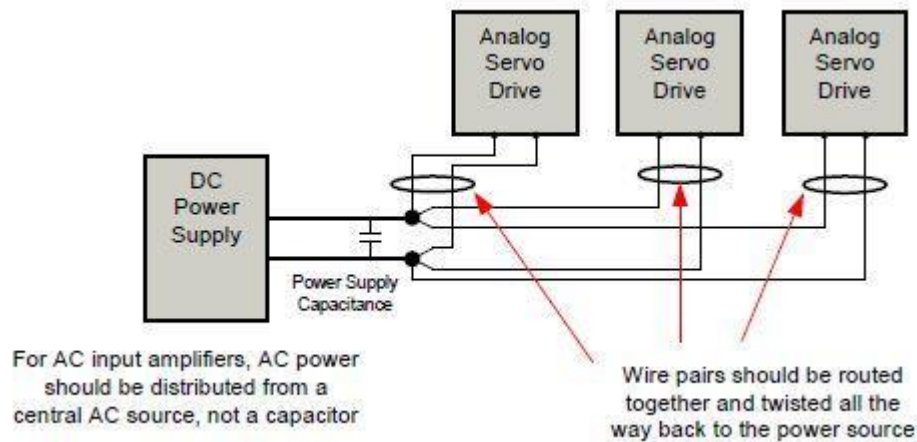
Figure 14.2. Correct configuration of multiple power supply wiring [12].

6) Power Supply- connect the transformer-isolated DC supply high voltage to the DC Power Input terminal, and the DC supply ground to the power ground terminal.

14.2. Block Diagram
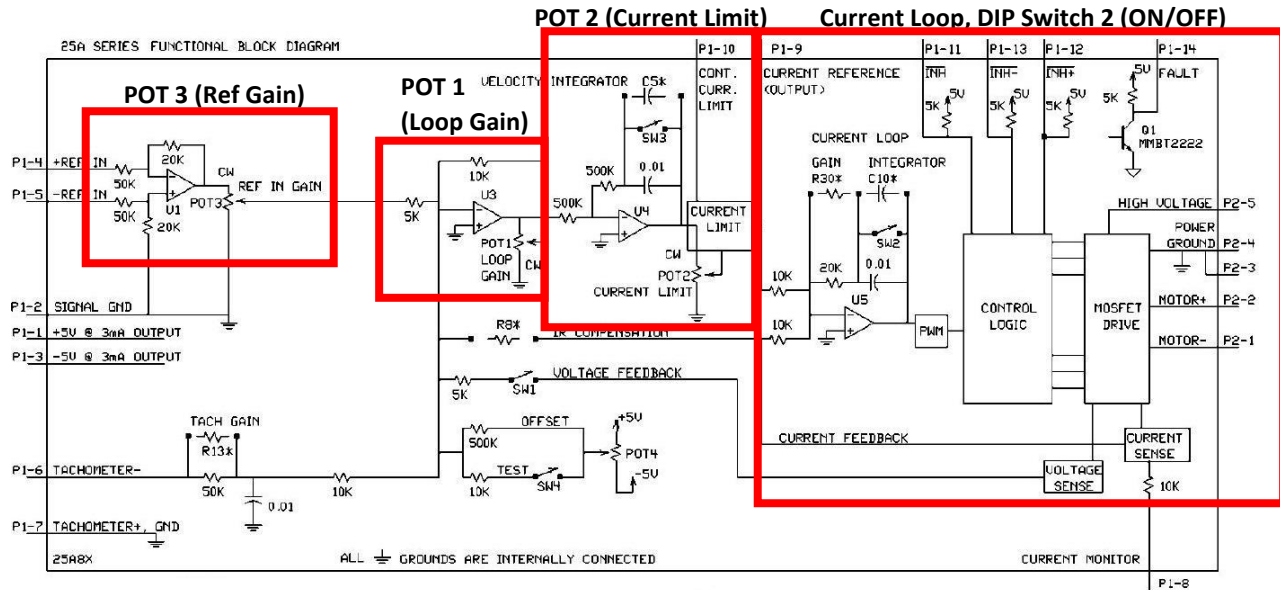
Figure 14.3. 12A8 Analog Servo Drive block diagram.

14.3. Tuning Procedure

1) Set Servo Drives to Current Mode
2) DIP Switches- Switch 1: **OFF**, Switch 2: **ON**, Switch 3: **ON**, Switch 4: **OFF**
3) Potentiometers- POT 1: **FULLY CCW**, POT 2: Adjustable, POT 3: **FULLY CW**, POT 4: Adjustable (Offset/Test).
4) Servo Drive Inputs- Pin 4: **+REF IN**, Pin 5: **-REF IN**
5) Servo Drive Outputs- Pin 8: **CURRENT MONITOR**, Pin 2: **SIGNAL GND**
6) Use DIP switches to set the servo drive in current mode.
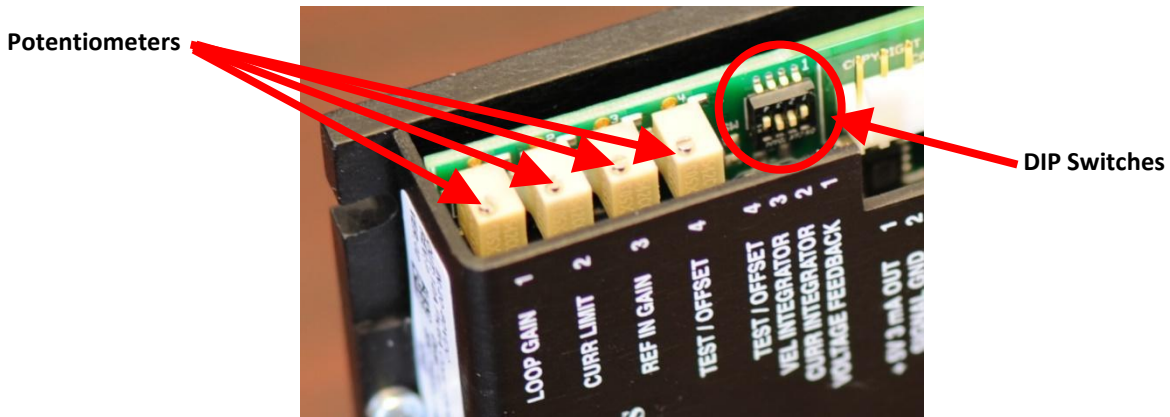
Figure 14.4. Adjustable potentiometers and DIP switches on 12A8 servo drive.

7) Use a function generator to produce the input command. Hook it up to the input reference of the drive and set it to the input of a 50-100 Hz square wave. Set the square wave amplitude so the drive outputs a current step similar to what will be expected when the drive is in operation. Use **Channel 1** of oscilloscope to view square wave input.

8) Connect wire of **CURRENT MONITOR** pin to **Channel 2** of oscilloscope to view the output of the drive. **Note: Best option is using a current probe clamped to the MOTOR PHASE A. Signals from the CURRENT MONITOR pin are unfiltered and may be difficult to view. Also, this pin may be isolated from the drive power ground. If this is the case, the oscilloscope must have isolated channels to avoid large ground currents.**
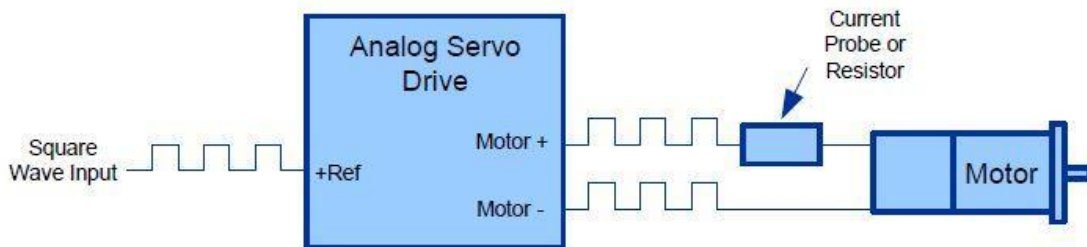
Figure 14.5. Single phase (Brush type) configuration [16].

9) View initial response of the current loop on oscilloscope. Switch any of the DIP switches within current loop to adjust response.
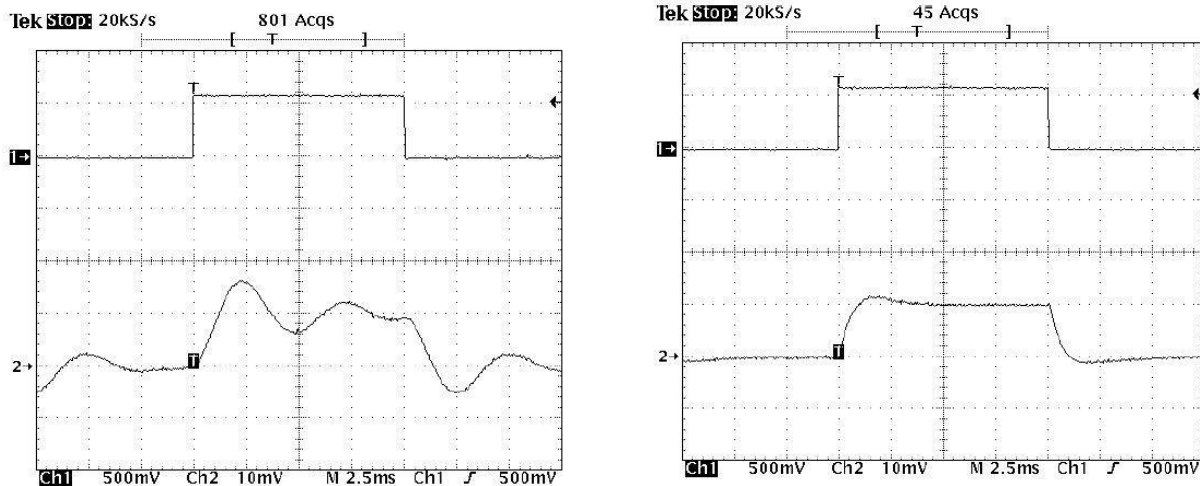
**Figure 14.6.** Current loop responses with Switch 2 ON (Left) and Switch 2 OFF (Right) [16]. *Note: These are example responses provided by the manufacturer.*

10) Additional current loop tuning with through PCB through-hole components may be necessary in the case of the following:
   a) Motor rapidly overheats even at low current.
   b) Drive rapidly overheats even at low current.
   c) Vibration sound comes from the drive or motor.
   d) The motor (load) has a high inductance **(>10mH)**.
   e) The motor has a low inductance (near minimum rating of the drive).
   f) Slow system response times.
   g) Excessive torque ripple (N/A).
   h) Difficulty tuning position or velocity loops (N/A).
   i) Electrical noise problems.
   j) High power supply voltage (power supply voltage is significantly higher than the motor voltage rating or near the drive high voltage rating).
   k) Low power supply voltage (power supply voltage is near the low voltage rating of the drive).
11) An Additional resistor may be added at the **R30*** location, effecting the gain of the current loop. An additional capacitor may be added at the **C10*** location, effecting the current loop integrator (dampened response).

R30*/C10*
Through-Holes
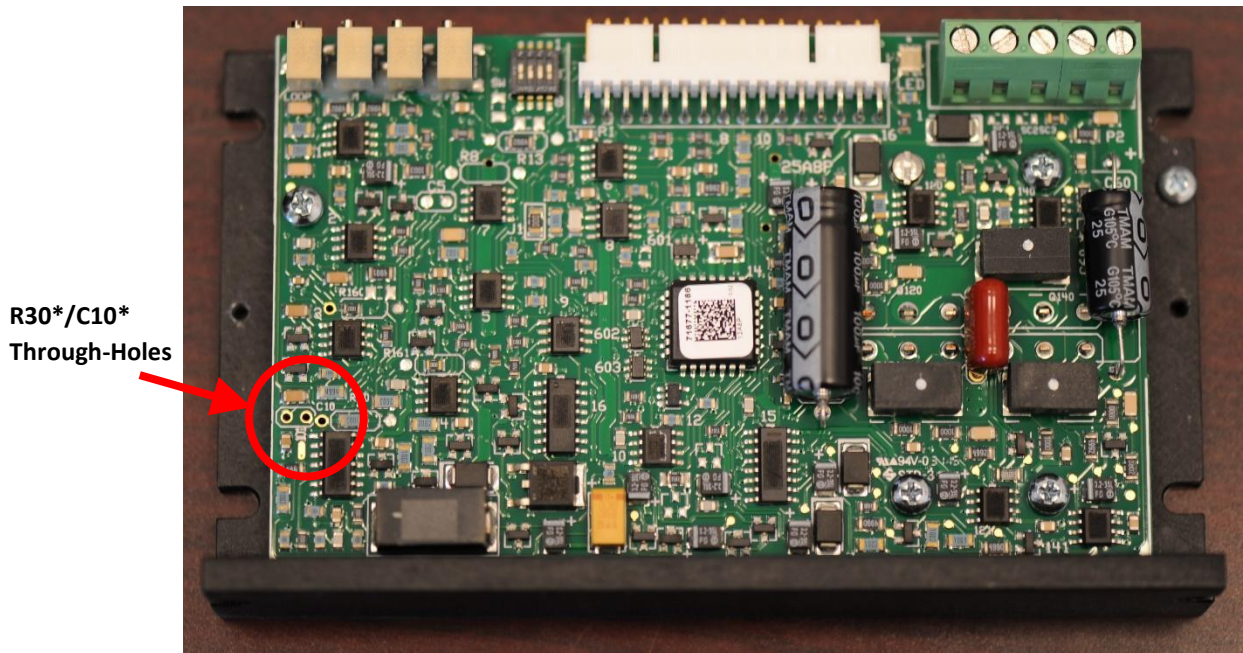
Figure 14.7. Inside of Analog Servo Drives with through-hole component call-out for additional tuning.

## 14.4. Results

Square wave input tests comprised the first major test of the system. These were conducted with only one servo drive plugged into the connection box at a time. This one servo drive was paired with each of the four actuators, one at a time, to produce the oscilloscope images depicted below. These results demonstrate that there are clear differences between the responses of the different coils. These tests were repeated for each servo drive, verifying that the differences were indeed within the coils and not the drives. Each drive produced the same result for each coils. During the tests, only one actuator was powered at a time. The laminated rotor mass was inserted within the stator in its normal operating position for the tests. Two signals are displayed on the oscilloscope images. The first is a clean, square wave input signal provided to the servo drive powering the coil of interest. The second is the current signal recorded by a Hall-effect current sensor in series with powered coil. This sensor displays a voltage signal of 400 mV per 1 Amp measured. This voltage is the signal displayed on the scope, and is superimposed over the square wave input. The apparent high frequency noise present in this signal is actually a predictable, high frequency (over 40 kHz) chirp that is believed to come from the MOSFET switching frequency of the servo drives. Attempts at adjusting the shape of the signal using the "REF IN GAIN" and "CURR LIMIT" potentiometers did not significantly impact the shape of the current output signal.

69

Later it was found that the system's current output was almost perfectly able to follow a sine wave input with a DC offset (such that the current in the coils would never switch direction). Since this test was much more representative of the actual operating conditions of the system, this was a promising result, and it was decided to move forward with PID control testing.

It was also found that the servo drives were not able to respond to input voltages below about 0.4 V. Below this input voltage, no current was produced in the coils. Once the input voltage was increased above this level, a current signal gradually became visible that matched the input signal. For accurate control, it is important that the input signal provided to the servo drives never drops below this offset voltage after startup.
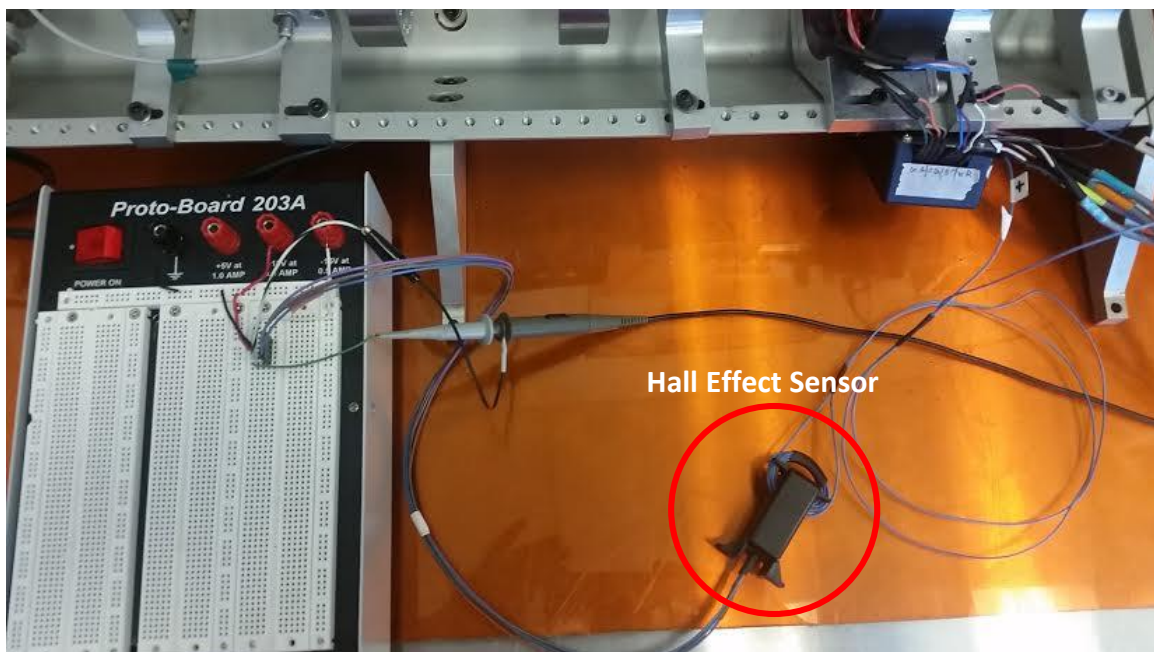
Figure 14.8. Hall effect current sensor attachment to the AMB/Servo Drive connection box.
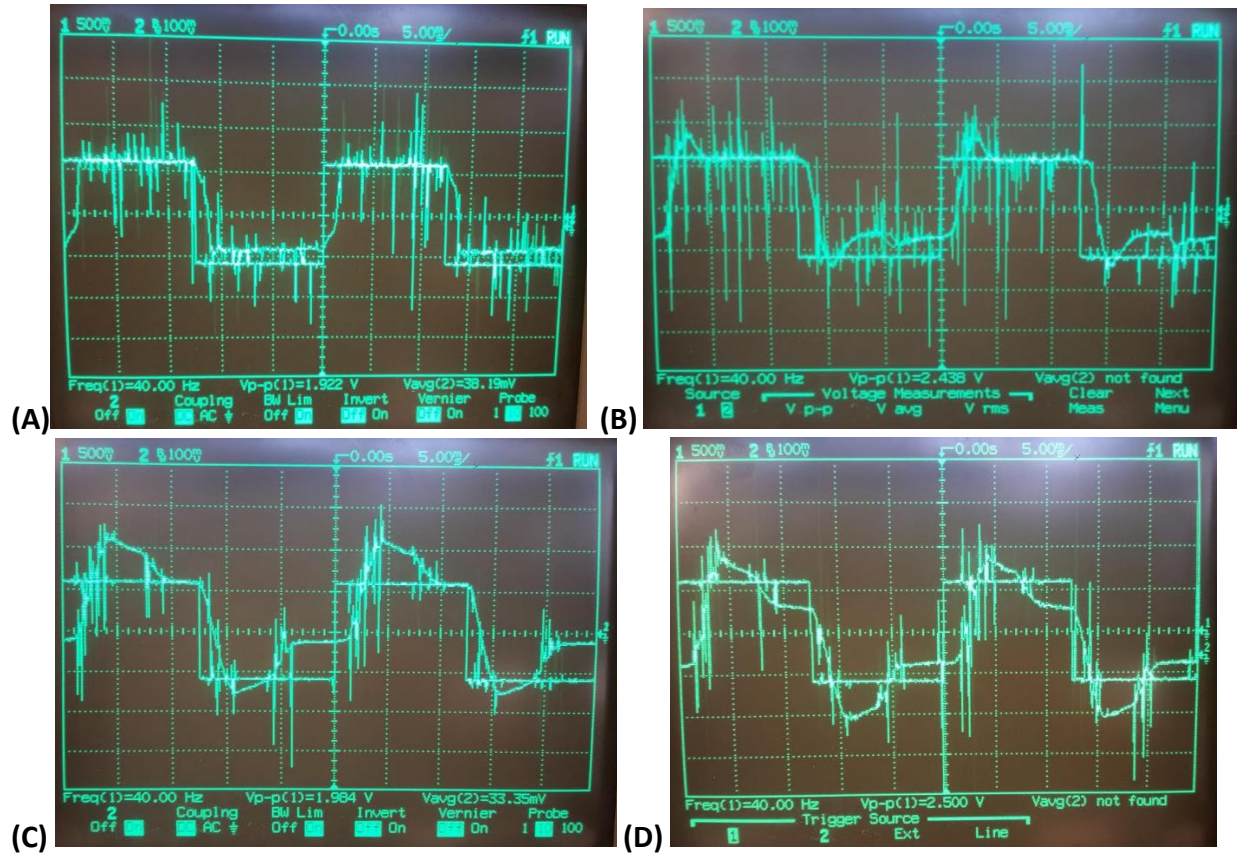
Figure 14.9. Actuator responses for colored wire configurations: **(A)** Red/White, **(B)** Green/Brown, **(C)** Blue/Purple, and **(D)** Gray/Orange.

15. LabVIEW Real-Time Simulation
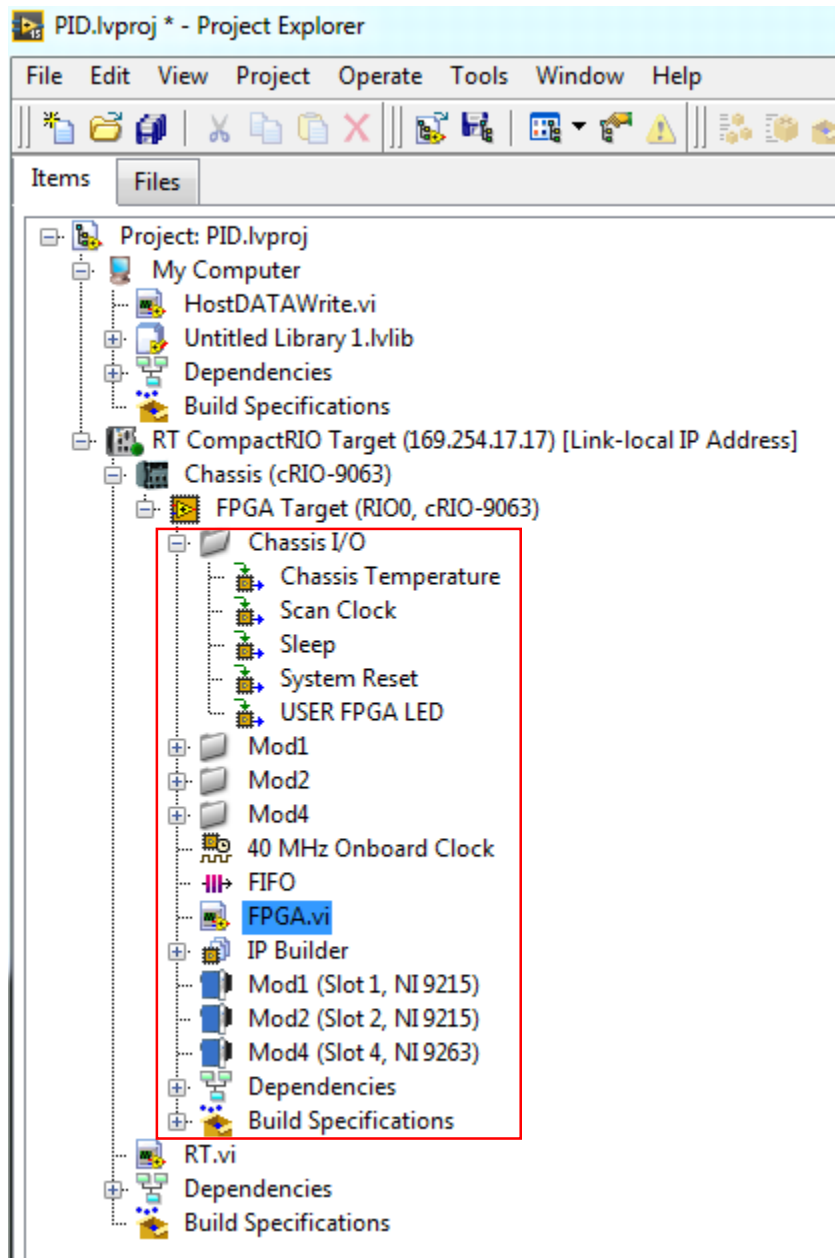
Figure 15.1. LabVIEW project tree. The core of the program is boxed in red. The visual interface tab is located directly below this box (RT.vi).
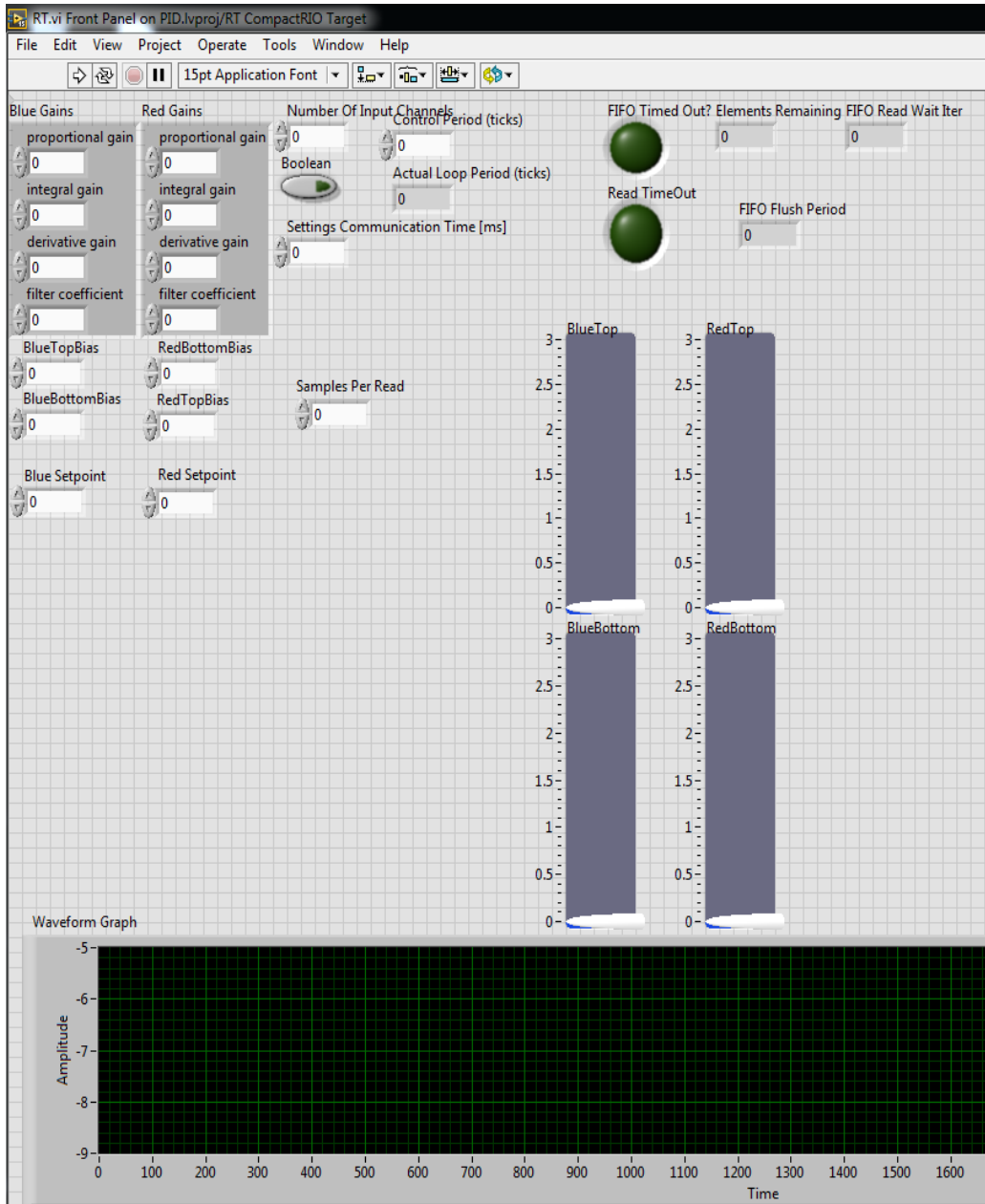
Figure 15.2. Visual interface of the LabVIEW PID control. From this window, inputs to the controller can be monitored through the "waveform graph" and the control voltages being applied to the servo drives can be viewed with the four slider bars. Controller gains (Ki, Kp, Kd, filter coefficient), voltage biases (which translate to bias currents), and voltage setpoints (representing the position probes' voltage outputs when the shaft is centered) can all be adjusted from this pane in real time, while the AMB is running.

Figure 15.3. LabVIEW block diagram for the PID control program. Note that the four hardware inputs labeled "Mod1" and "Mod2" are currently unused. For more details, contact Cameron Naugle who was a graduate student working for Dr. Wu at the time of the project.

16. Testing and System Identification
16.1. Test Results

Upon connecting the wires of the pole pairs making up each coil actuator, continuity checks were conducted with a direct voltage input from a power supply, demonstrating that these electromagnets were indeed capable of attracting the rotor mass. There did not appear to be any interruptions in the magnetic coils and each coil was measured to have a resistance of about 1.3 Ohms.

Once the device was assembled, the eddy current proximity sensors were positioned to each display about -7 Volts with the shaft at its center position. -5 Volts is reportedly the recommended sensor zero position for the Bently kits, but -7 Volts was chosen so that at the maximum and minimum displacements of the rotor allowed by the stator, the sensors would still be within their linear range. These sensor center voltages were then input as the "blue setpoint" and "red setpoint" in the LabVIEW control visual interface. These color designations refer to the colored tape identifying the proximity probes.

When testing the PID control setup, both active feedback and levitation configurations were attempted. For active feedback, two support bushings were used at either end of rotor shaft, and the AMB assembly was placed between them. For levitation, the outboard support bushing was removed, with the AMB attempting to replace it. Full levitation was never attained, but should be possible. There was simply not enough time available to work through the procedure of achieving it.

However, active feedback was successfully achieved. As shown in the figures below, the two eddy current probe position signals were first displayed with the shaft rotating at 1,000 RPM and the AMB off. The AMB was then powered on to resist the oscillations of the shaft with proportional control only (KI and KD set to zero). When this was done, the AMB significantly reduced the amplitude of the shaft oscillations. An abundance of high frequency noise was also produced when turning on the AMB, possibly due to the servo drive switching frequency interfering with the eddy current sensors. Even with the noise, the dominant eddy current probe signal is still clearly visible and clearly attenuated from the previous readings with the AMB off. These oscilloscope plots were recorded with the same scaling and at the same 1,000 RPM rotational speed.
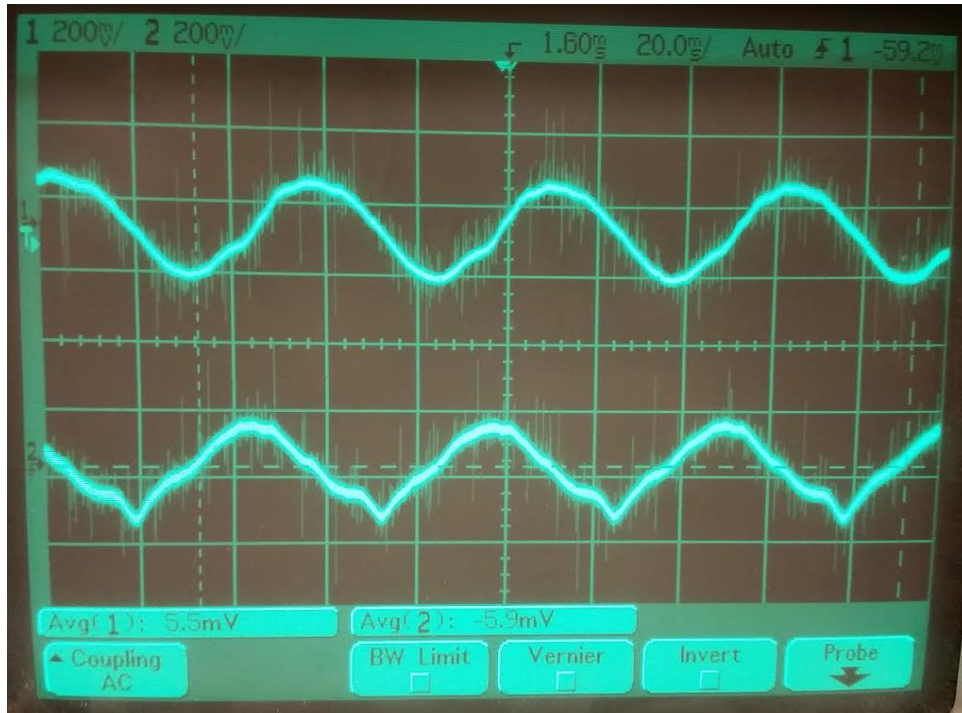
Figure 16.1. Position probe outputs at 1,000 RPM with AMB powered off.

Figure 16.2. Position probe outputs at 1,000 RPM with AMB applying active feedback.

16.2. Observations

During testing, a variety of observations were made. Regarding the control settings, only proportional gain was used in the PID loops. A proportional gain of 0.1 was used at startup. The device was found to be very sensitive to changes to the proportional gain and bias voltages. To accommodate this, the proportional gain and bias values were incremented very slowly, with all biases starting at 0 V upon startup. Very small step increments of about 0.01 V are recommended for adjusting each of these values when ramping up to full operation. In some instances, sparks appearing to originate from the actuator coils were observed when the servo drive power supply switch was flicked on with a control signal already being applied. It is hypothesized that these sparks may be the result of arcing between the stator and sections of magnet wire where the enamel may have been scratched off.

While experimenting, the proportional gain was never allowed to exceed 1. While the system was running at a stable operation providing active feedback, the derivative gain was experimented with. It was allowed to reach about 1 before it produced too much instability. Whenever integral gain was turned on, the system rapidly became unstable. During active feedback testing, the laminated rotor mass occasionally stuck to the inside of the stator when control values were being experimented with. This demonstrated that the touchdown bearing designed was not sufficient. However, when this occurred, the touchdown bearing did allow adjustments to the control values to free the rotor mass rather than having to power down the whole system.

17. Recommendations

A number of recommendations for future inheritors of this project have been stated within other appropriate sections of the report. This section will focus upon additional recommendations not previously mentioned.

First, it is important to note that full testing of the AMB did not begin until the week prior to the project expo. For this reason, much remains to be explored regarding the capabilities of the device. The surface has truly only been scratched.

After a literature review and full familiarization with this report and the existing hardware, a variety of potential avenues exist for further characterization and improvement of the system. To begin, a more robust controls analysis and transfer function characterization of system components is in order. This will allow for more educated controller tuning. This may include a more advanced rotordynamics analysis using transfer matrices rather than assuming a lumped mass model. Modal analysis of the rotor shaft would also be valuable and could be incorporated into the controls to account for the sensors being located away from the center of the laminated rotor mass. It may also be worth considering different configurations of the eddy current sensors. For example, with a new mounting method, it could be possible to place the sensors on opposite sides (axially) of the rotor mass. A variety of alternatives exist.

As previously mentioned, a redesign of the touchdown bushing would be a valuable investment for improving the safety and longevity of the device. Such a redesign might involve a technique for holding the rotor shaft and gradually releasing it (once the system has been fully powered up) for attempts at levitation. Further start up procedures relating to both the controls and hardware should also explored, particularly in the case of attempting levitation. Part of this may include modifying the LabVIEW visual interface to produce a more gradual ramp up step size for the various control values.

Jigger Jumonville, the Cal Poly turbomachinery professor, would be a valuable resource for further insights and possibilities for the project. In hindsight, it would have been extremely useful to have contacted him earlier in the project.

It may be useful to build more Hall-effect current probes for simultaneously measuring the current in multiple coils. Additional probes can be found in the mechatronics closet (accessible through rooms 116 and 118 in building 192). .

It should also be noted that while improvements to the device are certainly possible through subsequent senior projects, the large amount of front end research required to understand magnetic bearings may make improvements much more conducive to a graduate level project. This is especially true considering the utility that higher level coursework would serve in attempting to address many of the recommendations made.

18. References

1. Farmakopoulos M., Papadopoulos C., Nikolakopoulos P., and A. Tzes (2013). A Control Model of Active Magnetic Bearings. University of Patras, Greece.
2. H. Bleuler, M. Cole, P. Keogh, R. Larsonneur, E. Maslen, R. Nordmann, Y. Okada, G. Schweitzer, A. Traxler, 2009 Magnetic Bearings:2. Theory, Design, and Application to Rotating Machinery. *Springer-Verlag Berlin Heidelberg*. 535 p. ISBN 978-3-642-00496-4.
3. Hwang Hun Jeong, So Nam Yun and Joo Ho Yang (2012). Control of Magnetic Bearing System, Performance Evaluation of Bearings, Dr. Rakesh Sehgal (Ed.), ISBN: 978-953-51-0786-6, InTech, DOI: 10.5772/51185. Available from: http://www.intechopen.com/books/performance-evaluation-of-bearings/control-of-magnetic-bearing-system. Ch.8
4. Wikipedia (Magnetic Bearing).
5. Ungar, Eugene, and Kenneth Stroud. *A New Approach to Defining Human Touch Temperature Standards*. Houston: NASA, n.d. Print.
6. Yoon, Se Young, Zongli Yin, and Paul E. Allaire. *Control of Surge in Centrifugal Compressors by Active Magnetic Bearings*. London: Springer, 2013. Print.
7. Lijesh, K.P., and Harish Harani. "Optimization of Eight Pole Radial Active Magnetic Bearing." *Journal of Tribology* (2015): n. pag. Print.
8. "Wire Gauges - Current Ratings." *The Engineering Toolbox*. N.p., n.d. Web. 15 Nov. 2015. <http://www.engineeringtoolbox.com/wire-gauges-d_419.html>.
9. "Silicon Steel (Electrical Steel)." *Proto Laminations Inc.* N.p., n.d. Web. 15 Nov. 2015. <http://www.protolam.com/page7.html>.
10. *Lamination Steels Third Edition*. N.p.: Electric Motor Education and Research Foundation, 2007. Print.
11. Budynas, Richard, and Keith Nisbett. *Shigley's Mechanical Engineering Design (PDF)*. 10th ed. N.p.: n.p., n.d. Print.
12. Advanced Motion Controls. "12A8 Analog Servo Drive." *Downloadable Resources-Data Sheet.* <http://www.a-m-c.com/support/downloadable_resources.html>
13. Advanced Motion Controls. "PS16 Series Unregulated Power Supplies." *Downloadable Resources-Data Sheet.* <http://www.a-m-c.com/support/downloadable_resources.html>
14. Advanced Motion Controls. "Analog Panel Mount Servo Drives- Installation of Analog Panel Mount Servo Drives." *Downloadable Resources.* <http://www.a-m-c.com/support/downloadable_resources.html>
15. Advanced Motion Controls. "AN-011- Analog Drive Configuration and Setup." *Downloadable Resources.* <http://www.a-m-c.com/support/downloadable_resources.html>

16. Advanced Motion Controls. "AN-015- Current Loop Tuning Procedure." *Downloadable Resources.* <http://www.a-m-c.com/support/downloadable_resources.html>

17. Advanced Motion Controls. "AN-016- Analog Drive Current Limits." *Downloadable Resources.* <http://www.a-m-c.com/support/downloadable_resources.html>

18. National Instruments. "NI cRIO-9063." <http://sine.ni.com/nips/cds/view/p/lang/en/nid/213090>

19. National Instruments. "NI 9215." <http://sine.ni.com/nips/cds/view/p/lang/en/nid/208793>

20. National Instruments. "NI 9263." <http://sine.ni.com/nips/cds/view/p/lang/en/nid/208806>

21. GE Bently Nevada. "Bently Nevada 3300 XL Series Proximitor System." <https://www.gemeasurement.com/sensors-probes-transducers/proximity-probes/bently-nevada-3300-xl-series-proximitor-system>

19. Appendices

Appendix A
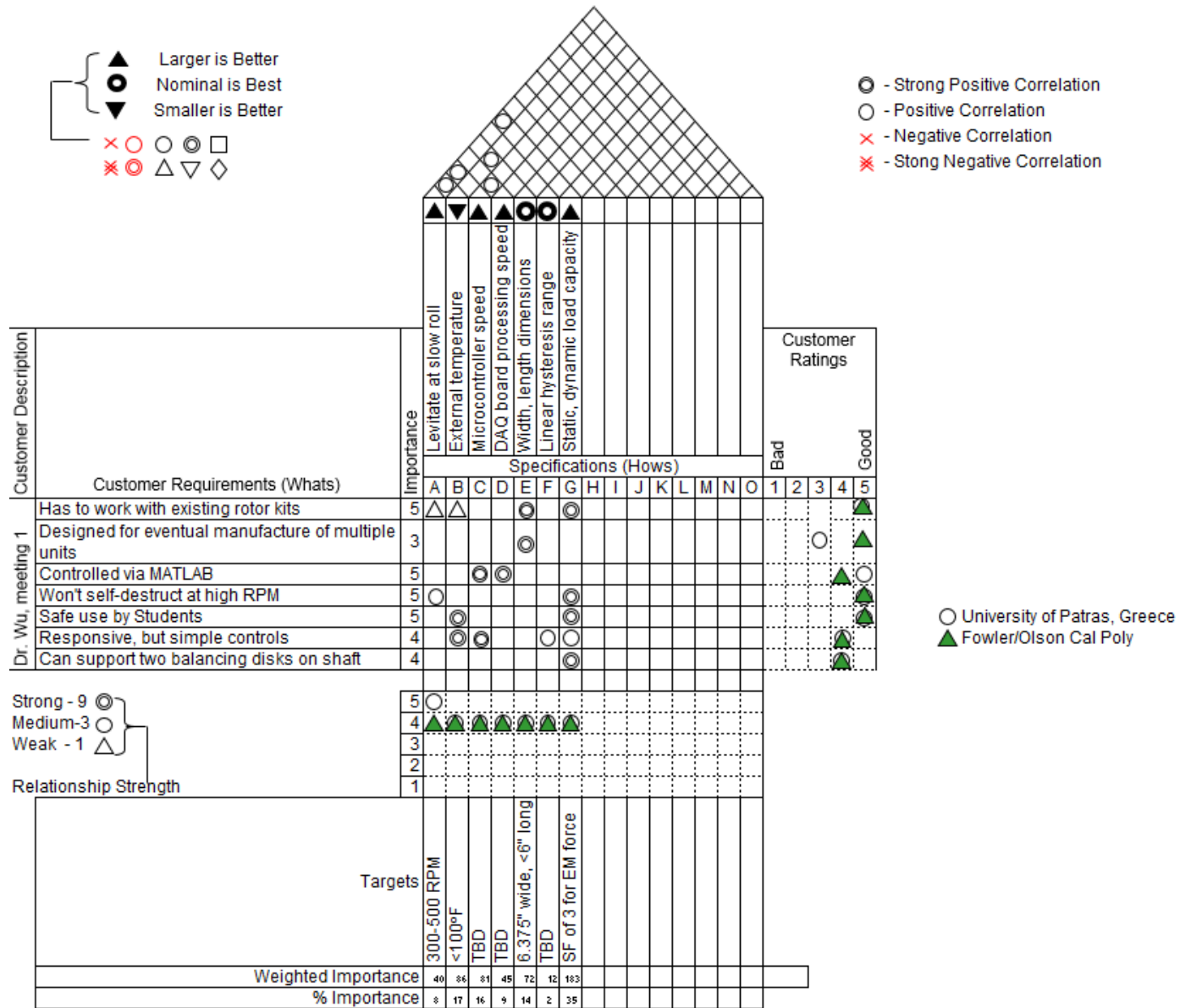
<u>Appendix B</u>

Codes and Standards

1.   **ISO 9000 series:** Standardized procedures that should be followed by any company or established to be recognized as a certified institution.

2.   **ISO 14839 1:** Mechanical Vibration- Vibration of rotating machinery equipped with active magnetic bearings- Part 1: Vocabulary.

3.   **ISO 14839 2:** Mechanical Vibration- Vibration of rotating machinery equipped with active magnetic bearings- Part 2: Evaluation of Vibration.

4.   **ISO 14839 3:** Mechanical Vibration- Vibration of rotating machinery equipped with active magnetic bearings- Part 3: Evaluation of Stability Margin.

5.   **ISO 14839 4:** Mechanical Vibration- Vibration of rotating machinery equipped with active magnetic bearings- Part 4: Technical Guidelines.

Two Plane Model

Wipe the Slate

```
clc
clear all
close all
```

Import Test Data

Bearing 1 data1 = csvread('BrgVert1&2.csv');

```
data2 = csvread('IRPM.csv');
% data3 = csvread('OHor.csv');
data4 = csvread('OVer.csv');
data5 = csvread('IRPM.csv');
% data6 = csvread('IHor.csv');
data7 = csvread('IVer.csv');
```

Rotor

System Parameters

```
L1 = .197; %m, length to first mass .150
L2 = .2; %m, length between masses .130
L3 = .233; %m, length from second mass to outboard bearing .175
L = L1+L2+L3; %m, total length between bearing supports
M_D = 0.8; %[kg] disk mass
```

```matlab
M_r = 0.5; %[kg] AMB rotor mass
ro_st = 7850; %[kg/m3] density of steel
Ds = .01; %[m]
A = pi/4*(Ds^2); %[m2] cross-section of main rotor
g = 9.81; %[m/sec2]
LD = .015; %[m] length of disk
R = sqrt(M_D/(pi*LD*ro_st)); %[m] radius of disk
M_shaft = A*ro_st*L;
M_static = M_D + M_r + M_shaft; % total mass of rotor
E = 200e+09; %N/m^2 modulus of elasticity of steel
I = pi/4*(Ds/2)^4; %m^4, area moment of inertia

% Static Load Capacity
Fin = (M_D*g*L3 + (A*g*ro_st*L)*(L/2) + M_D*g*(L3+L2))/L; %[N] Reaction force at inboard
Fout = (M_D*g*L1 + (A*g*ro_st*L)*(L/2) + M_D*g*(L1+L2) + M_r*g*L)/L; %[N] Reaction force at AMB

% Mass Matrix
M = [.8+.1*(L1+.5*L2)/L           0;...
        0           .8+.1*(L3+.5*L2)/L];     %kgram, mass matrix

% Choose K for tuning, Ka=stiffness of bearing A and Kb=stiffness of
% bearing B
Ka =290000;          %N/m
r = 100/100;
Kb = r*Ka;           %N/m

% Case 1. Rigid shaft, flexible bearings. Solved from geometry and FBD of case
C_b = 1/L^2.*[(L1^2)/Kb+((L2+L3)^2)/Ka,      L1*(L1+L2)/Kb+(L2+L3)*L3/Ka;...
              L1*(L1+L2)/Kb+(L2+L3)*L3/Ka,    ((L1+L2)^2)/Kb+(L3^2)/Ka]; % m/N

% Case 2. Flexible Shaft, Rigid Bearings. Solved from strength of materials
C_s = [(L1^2)*((L2+L3)^2)/3/E/I/L,      L1*L3*(L^2-L1^2-L3^2)/6/E/I/L;...
        L1*L3*(L^2-L1^2-L3^2)/6/E/I/L,     (L3^2)*((L1+L2)^2)/3/E/I/L]; % m/N

% Case 3. System Stiffness
K = inv(C_s + C_b);% N/m, total stiffness is the linear combination of the two stiffness
matricies
D = .0003.*K; % estimate of damping, parameter can be modified to match experimental data

% Natural Frequency prediction by Eigenvalue problem
v = eig(K,M)
wn = [sqrt(v(1))/2/pi*60, sqrt(v(2))/2/pi*60]
```

v =

  1.0e+05 *

```
   0.1403
   2.2253


wn =

   1.0e+03 *

   1.1310    4.5047
```

Test

```matlab
alpha = 3000/60/60*2*pi; %Rad/s^2
w0 = 0/60*2*pi; %Rad/s
Phi = [0, pi/8]; %rad, [(Phase angle at disk 1), (Phase angle at disk 2)]
a = [3*(.0000254), 3*(.0000254)]; %[m], eccentricity of Disk 1 and Disk 2 [.75*(.0000254),
.75*(.0000254)]
tspan = [0:1/600:200]; %1:1/535:200
y0 = [0 0 0 0]';
options = [];
[t,y] = ode45(@TwoPlaneODE,tspan,y0,options,K,D,M,alpha,w0,Phi,a);

% Stop = length(omega);
% for i = 1:Stop
%     F1x(i,1) = M(1,1)*e1*omega(i,1).^2*cos(omega(i,1)*t(i,1) + phi1);
%     F2x(i,1) = M(2,2)*e2*omega(i,1).^2*cos(omega(i,1)*t(i,1) + phi2);
%     F1y(i,1) = M(1,1)*e1*omega(i,1).^2*sin(omega(i,1)*t(i,1) + phi1) - M_D*g;
%     F2y(i,1) = M(2,2)*e2*omega(i,1).^2*sin(omega(i,1)*t(i,1) + phi2) - M_D*g;
%     Ftotx(i,1) = F1x(i,1) + F2x(i,1);
%     Ftoty(i,1) = F1y(i,1) + F2y(i,1);
%     F3x(i,1) = (F2x(i,1)*(L2+L1) + F1x(i,1)*L1)/L;
%     F3y(i,1) = (F2y(i,1)*(L2+L1) + F1y(i,1)*L1)/L;
% end

W_RPM = (alpha*t+w0)*60/2/pi;
[Amp1, loc1] = findpeaks(y(:,1));
[NegAmp1, Negloc1] = findpeaks(-y(:,1));
if length(Amp1) > length(NegAmp1)
    Amp1(length(NegAmp1)+1:length(Amp1)) = [];
    loc1(length(Negloc1)+1:length(loc1)) = [];
else
    NegAmp1(length(Amp1)+1:length(NegAmp1)) = [];
    Negloc1(length(loc1)+1:length(Negloc1)) = [];
end
Amp1 = Amp1+NegAmp1;
```

85

```matlab
if length(Negloc1)>length(loc1)
    w1 = W_RPM(Negloc1);
else
    w1 = W_RPM(loc1);
end
[Amp2, loc2] = findpeaks(y(:,3));
[NegAmp2, Negloc2] = findpeaks(-y(:,3));
if length(Amp2) > length(NegAmp2)
    Amp2(length(NegAmp2)+1:length(Amp2)) = [];
    loc2(length(Negloc2)+1:length(loc2)) = [];
else
    NegAmp2(length(Amp2)+1:length(NegAmp2)) = [];
    Negloc2(length(loc2)+1:length(Negloc2)) = [];
end
Amp2 = Amp2+NegAmp2;
w2 = W_RPM(loc2);

% Rotor Unbalance Force
w1_rads = w1*(2*pi/60);
w2_rads = w2*(2*pi/60);
AMP1 = Amp1*39370.1;
AMP2 = Amp2*39370.1;
ecc1 = .5*AMP1*.0000254;
ecc2 = .5*AMP2*.0000254;
F1 = M_D*ecc1.*w1_rads.^2;
F2 = M_D*ecc2.*w2_rads.^2;
FD1 = (F2.*L3 + F1(1:length(F2)).*(L3+L2))/L; %[N] Reaction force at inboard (1:length(F1))
FD2 = (F1(1:length(F2)).*L1 + F2.*(L1+L2))/L; %[N] Reaction force at AMB (1:length(F1))
FD1max = max(FD1);
FD2max = max(FD2);
F1Tot = (Fin + FD1);
F2Tot = (Fout + FD2);
F1Totmax = max(F1Tot)
F2Totmax = max(F2Tot)


% Magnetic Bearing
A_c = 2.975e-04; %cross section area of actuator
A_g = A_c*1.05; %cross section area of air gap
eps = 0.8; % leakage and fringing correction factor for radial bearing
Bmax = 0.88;
Vmax = 72;
N = 300; %number of coil turns 250
mu_o = 4*pi*10^(-7); %air permeability
g_o = .0005; %[m] nominal air gap
I_B = g_o*Bmax/(mu_o*N); %[Amps] bias current 1.4
Fmag = (eps*mu_o*N^2*I_B^2*A_c)/(4*g_o^2) %[N] generate magnetic force with I_B
Fstatic = 4*Fmag %[N] max generated magnetic force with 2*I_B
ki = (eps*mu_o*A_g*(N^2)*(I_B))/(g_o^2); %[N/m] current stiffness
```

```
K = 0.25*mu_o*N^2*A ; % Schweitzer Pg. 80
ki_A = 4*eps*K*I_B.*cosd(alpha)/(g_o)^2; % Schweiter Pg. 80
ks = (eps*mu_o*A_g*(N^2)*(I_B.^2))/(g_o^3); %[N/m] position stiffness
ku = ki; % Schweitzer Pg. 48, motion induced voltage stiffness
Lc1 = ki.^2/abs(ks); % Schweitzer Pg. 48
Lc2 = (mu_o*(N^2)*A_g)/(2*g_o); % Yoon Pg. 67, Control of Surge, also Schweitzer Pg. 77
MAXdidt = 2*g_o*Vmax/(mu_o*N^2*A_c); % max slew rate, neglecting iron reluctance and coil
resistance (eq. 3.39 in Yoon text).
MAXdFdt = 2*eps*I_B*vmax/g_o; % Max time rate of change of the magnetic force that can be applied
to the rotor  (eq. 3.40 in Yoon text)
VLc1 = MAXdidt*Lc1;
VLc2 = MAXdidt*Lc2;
wi1 = 6000*(2*pi/60); %[rad/sec]
wi2 = 2*wi1; %[rad/sec]
wi4 = 4*wi1; %[rad/sec]
i1 = 1; %[Amps]
i2 = .2; %[Amps]
i4 = .2; %[Amps]
Vtot = Lc2*(wi1*i1 + wi2*i2 + wi4*i4)

% FINAL = [w1 w1_rads F1Tot w2(1:length(F1Tot)) w2_rads(1:length(F1Tot)) F2Tot(1:length(F1Tot))];

% DS = cell2dataset(F2Tot);
```

F1Totmax =

   80.0837

F2Totmax =

   75.3884

Fmag =

   36.6668


Fstatic =

  146.6670

Vtot =

Plots

```
figure('Name','Inboard and Outboard Amplitude Response')
plot(w1,AMP1,'o b',w2,AMP2,'o r',data2(1,:),data4(1,:),'-k',data5(1,:),data7(1,:),'-g')
ylabel('Height [mils]')
xlabel('Omega [RPM]')
axis([300,10000,0,100])
legend('Sim Inboard','Sim Outboard','Exp Inboard','Exp Outboard','Location','east')

figure('Name','Inboard and Outboard Dynamic Force Reactions')
plot(w1(1:length(FD1)),FD1,'- b',w1(1:length(FD2)),FD2,'- r')
% ,data1(:,1),data1(:,2),'-k',data1(:,1),data1(:,3),'-g')
ylabel('FD [N]')
xlabel('Omega [RPM]')
% axis([300,10000,0,30])
legend('Inboard FD','Outboard FD','Location','southeast')

figure('Name','Inboard and Outboard Total Force Reactions')
plot(w1(1:length(F1Tot)),F1Tot,'- b',w1(1:length(F2Tot)),F2Tot,'- r')
% ,data1(:,1),data1(:,2),'-k',data1(:,1),data1(:,3),'-g')
ylabel('FTot [N]')
xlabel('Omega [RPM]')
% axis([300,10000,0,30])
legend('Inboard FD','Outboard FD','Location','southeast')
```

89
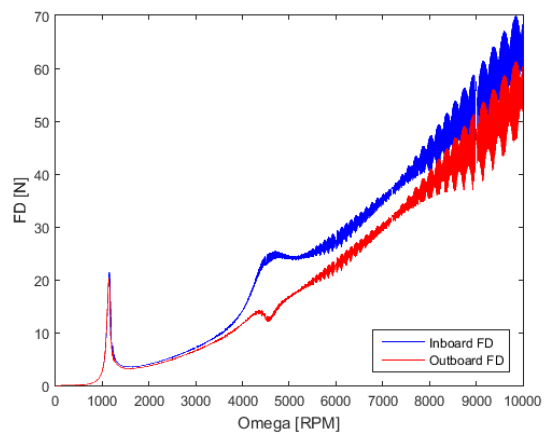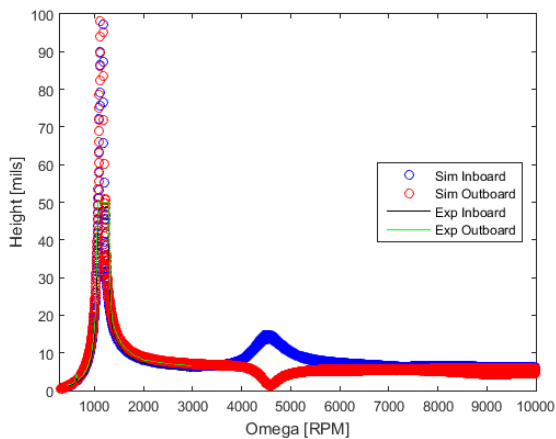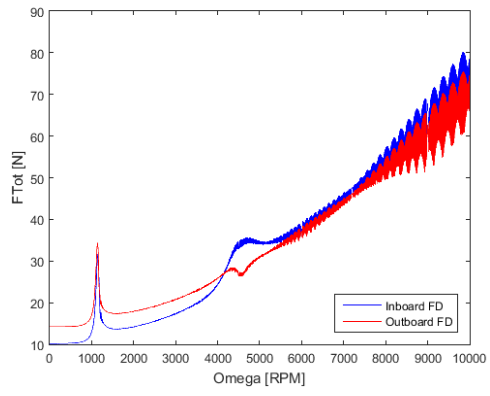
MagForceCalc_AWG22.m

Force, Geometry, and Electromagnetic Properties Calculations

11/13/15 Sean Fowler Garrett Olson

```
clc
clear all
```

Design Variables

```
N = 300; % number of coils
Npp = N/2; % number of coils per pole
Bmax = .88; % [Tesla] = [kg/A*s^2] flux value corresponding to the knee of the material's BH
curve
% Bknee = 1  [Tesla]
% http://dspace.mit.edu/bitstream/handle/1721.1/66486/6-061-spring-
2007/contents/assignments/steel_data.pdf
Vmax = 72; % [Volts] this is dependent on the amplifier chosen
```

Geometry Design Variables

```
s0 = 0.5*10^-3; % [m] nominal air gap
dcc = 0.668*10^-3; % [m] Gauge # 22.  copper wire + enamel diameter
% http://www.engineeringtoolbox.com/wire-gauges-d_419.html
nl = 4; % number of layers of copper wire on one pole
ppc = 2*10^-3;  % [m] stator pole length past the coil
% Dimensions below correspond to Fig. 3.18 (page 105 of Schweitzer pdf, 91
% of book)
b = 35*10^-3; % [m] core thickness
c = 8.5*10^-3; % [m] leg width
di = 23*10^-3; % [m] shaft diameter (rotor diameter that the rotor laminations are mounted over)
```

Calculated Geometric Variables

Dimensions below correspond to Fig. 3.18 (page 105 of Schweitzer pdf, 91 of book)

```
Acc = Npp*dcc^2*pi*.25; % [m^2] cross-sectional area of the coils on one pole
hc = Npp*dcc/nl; % [m] coil height of 1 layer
wc = nl*dcc; % [m] coil width
dr = di+2*c; % [m] laminated rotor OD
disp('Laminated rotor section diameter [cm]')
disp(dr*100)
d = dr+2*s0; % [m] core ID
A = c*b; % [m^2] "opposing area of an electromagnet" core pole
P = 2*c+2*b; % [m] perimeter of one core pole
da = d + 2*ppc + 2*hc + 2*c % [m] core OD

AAcc = (0.25*pi*(da-2*c)^2-0.25*pi*(d+2*ppc)^2-8*c*hc-8*5*dcc*hc)/8;  % Available cross-sectional
area between poles for coil windings
if Acc > AAcc
    disp('WARNING: Not enough space for windings.')
end
pp = 8*c/(pi*d); % fraction of stator inner circumference that is material
disp('Fraction of stator inner circumference that is pole tip rather than air:')
disp(pp)
pa = 1-pp; % fraction of stator inner circumference that is air
agbp = pa*pi*(d+2*ppc)/8; % air gap between pole windings

if 2*wc + 2*dcc > agbp
    disp('WARNING: Air gap between poles is too small to accomodate copper coils')
    disp('Air gap between copper coils of adjacent poles [mm]:')
    disp(1000*(agbp-2*wc-2*dcc))
end
```

```
Laminated rotor section diameter [cm]
     4


da =

    0.1121

Fraction of stator inner circumference that is pole tip rather than air:
    0.5279
```

Constants

```matlab
% Mshaft = 0.33; % [kg] mass of shaft only
% Mdisk = 0.8; % [kg] mass of one disk
% Mlam = 0.4; % [kg] mass of laminated rotor section
% Mtot = Mshaft + 2*Mdisk + Mlam; % [kg] total rotor mass
Fworst = 76.73;    % [N} From experiments, Cameron Naugle's code (Dr. Wu's grad student)
eps = 0.8; % leakage and fringing correction factor for radial bearing
           % included in Ch.3 of 'Control of Surge in Centrifugal
           % Compressors by Active Magnetic Bearings' book
u0 = 4*pi*10^(-7); % [N/A^2] permeability of free space
alpha = deg2rad(22.5); % [rad] for radial bearing with 4 pole pairs
```

Heat Transfer Constants

```matlab
Vss = c*b*hc; % volume of silicon steel surrounded by 1 copper coil
Vcu = wc*hc*b*2+wc*hc*c*2; % volume of copper of 1 coil
rho_ss = 7700; % [kg/m^3] density of silicon steel
rho_cu = 8933; % [kg/m^3] density of pure copper (Heat Transfer textbook)
cp_ss = 486; % [J/kg*K]heat capacity of silicon steel
% http://pe.org.pl/articles/2011/9b/14.pdf
cp_cu = 385; % [J/kg*K] heat capacity of pure copper (Heat Transfer textbook)
m_pole = rho_ss*Vss; % mass of silicon steel surrounded by 1 copper coil
m_cu = rho_cu*Vcu; % mass of copper of 1 coil
dT = 16.7; % [K] degrees Kelvin change from room temp. (70F) to 100F.
```

Calculated Values

```
i0 = s0*Bmax/(u0*N); % [A] bias current (ib = i0) = one half current needed to reach Bknee
B = u0*N*i0/(2*s0);    % [T] nominal flux density in core

ix = i0; % [A] perturbation current. ix must be < i0. Here it is set to i0 for
         % worst case.
x = 0.358*10^-3; % [m] rotor displacement (set to nominal air gap for worst case)

K = eps*0.25*u0*N^2*A ;            % Schweitzer equation (3.26)
ki = 4*K*i0*cos(alpha)/(s0)^2;     % Schweitzer equation (3.28)
ks = -4*K*i0^2*cos(alpha)/(s0)^3;  % Schweitzer equation (3.29)

FgenMAX = ki*ix-ks*x               % Schweitzer equation (3.27)
disp('[N]')
disp('Safety factor on max load, neglecting slew rate complications:')
SF = FgenMAX/Fworst

MAXdidt = 2*s0*Vmax/(u0*N^2*A); % max slew rate, neglecting iron reluctance and coil resistance
(eq. 3.39 in Yoon text).
MAXdFdt = 2*eps*i0*Vmax/s0; % Max time rate of change of the magnetic force that can be applied
to the rotor  (eq. 3.40 in Yoon text)
```

```
FgenMAX =

  232.5225

[N]
Safety factor on max load, neglecting slew rate complications:

SF =

   3.0304
```

Copper Wire Losses

```
L = (Npp+1)*P ; % copper wire length for a pole
res = 0.0171*10^-6 ; % [Ohm*m^2/m] resistivity of copper magnet wire
% http://www.elektrisola.com/us/conductor-materials/copper.html
R = 4*L*res/(pi*dcc^2); % [Ohms] resistance of one pole coil.
PLc1 = i0^2*R ; % [Watts] Approximate power loss within 1 copper coil
disp('Total power loss [Watts] due to copper resistance:')
```

```
    disp(PLc1*8)

    % Check for current overload based on recommended max current density for
    % copper wire of 6 A/mm^2

    bias_current_density = i0/((dcc*1000)^2*pi*0.25);
    max_current_density = (ix+i0)/((dcc*1000)^2*pi*0.25)

    if bias_current_density > 6
        disp('WARNING: the bias current density is above recommended')
    end

    if max_current_density > 6
        disp('WARNING: the max current density is above recommended')

    end
```

```
Total power loss [Watts] due to copper resistance:
    6.9853


max_current_density =

    6.6605

WARNING: the max current density is above recommended
```

Heat Transfer Calculations

Assume: 1. negligible radiation heat transfer 2. negligible convection heat transfer to surrounding still air 3. negligible heat transfer to stator material not surrounded by copper wires 4. heat dissipated evenly between copper and steel, come to the same so that they come to the same temperature simultaneously NOTE: These assumptions have limited basis in reality but should provide a worst case, or minimum amount of time to reach 100 degrees F.

```
qcu = m_cu*cp_cu*dT;
qss = m_pole*cp_ss*dT;
t = (qcu + qss)/PLc1; % [s] minimum time to reach 100F
disp('Time [min] for a pole to reach 100F')
disp(t/60)

T1 = 21.11; % [degC] = to 70F
T2 = 29.44; % [degC] = to 85F
T3 = 37.78; % [degC] = to 100F
```

94

```
h_conv = 10; % [W/m^2*K]
q_conv =  8*(h_conv*hc*b*(T3-T1) + h_conv*hc*c*(T3-T1)); % [W]

k_cond = 2.5; % [W/m*K]
q_cond = 8*(k_cond*c*b*(T3-T1)/hc); % [W]

q_tot = q_cond+q_conv
```

Time [min] for a pole to reach 100F
   15.2739

q_tot =

    5.4127

Plots

```
omega = [0:25:1050]; % [rad/s] shaft rotation frequency from 0 to about 10,000 rpm
dFdtBound = MAXdFdt./omega; % bound on Fmax due to slew rate and max time rate of change of
magnetic force
FgenMAX = FgenMAX.*ones(length(omega));

loglog(omega, dFdtBound, 'g', omega, FgenMAX, 'b')
xlabel('Frequency [rad/s]')
ylabel('Load Capacity [N]')
grid on
axis([0 1000, 100, 1500])
legend('(Max dF/dt)/w', 'Fmax')
```
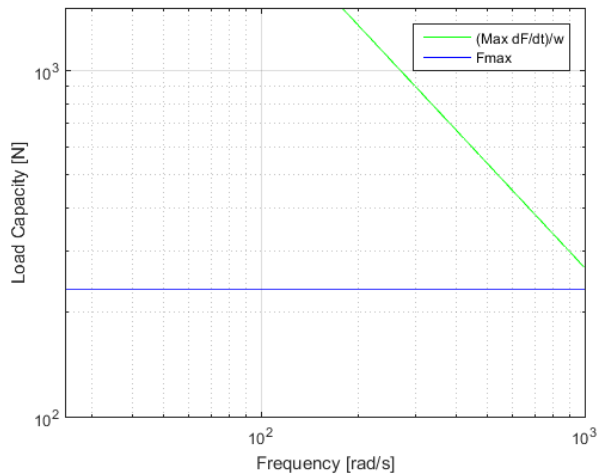
Parallel Coils Study

disp('PARALLEL COILS STUDY:')

```matlab
i0pcs = 1; % [A]
Npcs = 300; % windings
Npppcs = Npcs/2; % windings for 1 pole

Lpcs = (Npppcs+1)*P ; % copper wire length for a pole
Rpcs = 4*Lpcs*res/(pi*dcc^2); % [Ohms] resistance of one pole coil.
PLc1pcs = i0pcs^2*Rpcs;

Kpcs = eps*0.25*u0*Npcs^2*A ;            % Schweitzer equation (3.26)
kipcs = 4*Kpcs*i0pcs*cos(alpha)/(s0)^2;     % Schweitzer equation (3.28)
kspcs = -4*Kpcs*i0pcs^2*cos(alpha)/(s0)^3;   % Schweitzer equation (3.29)

FgenMAXpcs = kipcs*i0pcs-kspcs*x  ;
SFpcs = FgenMAXpcs/Fworst;
%%%%%%%%%%%%%%%%%%%%%%%%%%%%%%%%%%%%%%%%%%%%%%%%%%%%%%%
npw = 3; % number of parallel windings on a pole
Npcs2 = Npcs/npw; % windings
Npppcs2 = Npcs2/2; % number of windings in one parallel winding on one pole
i0pcs2 = i0pcs/npw; % current through one parallel winding

Lpcs2 = (Npppcs2+1)*P ; % copper wire length for a parallel winding on a pole
Rpcs2 = 4*Lpcs2*res/(pi*dcc^2); % [Ohms] resistance of one pole parallel coil.
PLc1pcs2 = i0pcs2^2*Rpcs2;
Ptotpcs2 = npw*PLc1pcs2;
```

96

```
Kpcs2 = eps*0.25*u0*Npcs2^2*A ;                % Schweitzer equation (3.26)
kipcs2 = 4*Kpcs2*i0pcs2*cos(alpha)/(s0)^2;      % Schweitzer equation (3.28)
kspcs2 = -4*Kpcs2*i0pcs2^2*cos(alpha)/(s0)^3;   % Schweitzer equation (3.29)


FgenMAXpcs2 = npw*(kipcs2*i0pcs2-kspcs2*x) ;
SFpcs2 = FgenMAXpcs2/Fworst;



% Result: Using parallel windings makes too large of an impact on the force
% output. It does significantly reduce losses though.  The more effective
% approach is to just increase the number of coils while reducing current.
```

Published with MATLAB® R2015a

Appendix E

AMB Amplifier

Wipe the Slate

```
clc
clear all
close all
```

Ampflifier Circuit Parameters

```
R1 = 50000;
R2 = 20000;
R4 = 5000;
R5 = 10000;
R6 = 500000;
R7 = 500000;
C7 = .05e-06;
Rpot3 = 1; %6000
Rpot2 = 1;
RA = 10000; %[Ohm]
Ra = 20000; %[Ohm] max without Rb
Rb = 10; %[Ohm] 500,000 max
RB = Ra*Rb/(Ra+Rb); %[Ohm]
% RB = 20000; %[Ohm]
Ca = 0.01e-06; %[F]
Cb = 0.00e-06; %[F] 0.8e-06, 0
CB = Ca + Cb; %[F]
```

```
L = 35.3e-03; %[H] with N=150, L=8-10 mH
R = 0.641; %[Ohm]
RC = 1; %[Ohm] 1, 10000
RD = 10000; %[Ohm]
```

Open Current Loop

```
a1 = RB*CB;
a0 = 1;
b1 = RA*L*CB;
b0 = CB*RA*(R+RC);
numGH_ol = [a1 a0]; %Numerator
denGH_ol = [b1 b0]; %Denominator
% GH = tf(numGH,denGH);
% GHzpk = zpk(GH);
```

Closed Current Loop

```
c1 = RB*CB*RD;
c0 = RD;
d2 = RA*L*CB*RD;
d1 = CB*(RA*RB*RC+RA*RD*(R+RC));
d0 = RA*RC;
numGH_cl = [c1 c0]; %Numerator
denGH_cl = [d2 d1 d0]; %Denominator
```

Gamp

```
C2 = RB*CB*RD*L;
C1 = RD*L + RD*RB*CB*R;
C0 = RD*R;
D2 = RA*L*CB*RD;
D1 = CB*(RA*RB*RC+RA*RD*(R+RC)-RB*RD^2);
D0 = RA*RC - RD^2;
```

Korean Amplifier

```
A1 = 3000;
A0 = 210000;
B2 = 1;
B1 = 3600;
B0 = 210000;

timeSim = 3; %[sec]
% Tp = .001; %peak time
% Ts = .001; %settling time
% pos = 5; %percentage overshoot
% z = -log(pos/100)/sqrt(pi^2+(log(pos/100)^2)); %zeta, damping ratio
% w_lp = pi/(Tp*sqrt(1-z^2)); %[rad/sec] low-pass frequency with Tp
% w_lp = 4/(Ts*z); %[rad/sec] low-pass frequency with Ts

% sim('AMP')
% open_system('AMP')
```

Plots

figure('Name','Amp Response') plot(tout(:,1),simout(:,1),'k',tout(:,1),simout2(:,1),'b',[0,5],[-1,-1],'r')
ylabel('Response') xlabel('Time [sec]') axis([0.96,1.2,-1.6,0]) legend('Korean Response','Servo
Drive','Location','northeast')

```
% figure('Name','Amp Response')
% plot(tout(:,1),simout(:,1),'k',tout(:,1),simout3(:,1),'b')
% % ,[0,5],[-1,-1],'r')
% ylabel('Response')
% xlabel('Time [sec]')
% axis([0.96,1.2,-10,0])
% legend('Korean Response','Servo Drive','Location','northeast')
```

Published with MATLAB® R2015a

Appendix F

AMB Controls

Wipe the Slate

```
clc
clear all
close all
```

Amplifier

R = 6.2; %[ohms] L = 9.2*10^-3; %[mH] Ri = 10000; %[ohms] Rs = 2; %[ohms] Rf = Ri*Rs; %[ohms] Rd = 2.75*10^5; %[ohms] Cf = 3.55*10^-9; %[muf]

Ampflifier Circuit Parameters

```
R1 = 50000;
R2 = 20000;
R4 = 5000;
R5 = 10000;
R6 = 500000;
R7 = 500000;
C7 = .05e-06;
Rpot3 = 1; %6000
Rpot2 = 1;
RA = 10000; %[Ohm]
Ra = 20000; %[Ohm] max without Rb
Rb = 10; %[Ohm] 500,000 max
RB = Ra*Rb/(Ra+Rb); %[Ohm]
% RB = 20000; %[Ohm]
Ca = 0.01e-06; %[F]
Cb = 0.00e-06; %[F] 0.8e-06, 0
CB = Ca + Cb; %[F]
L = 35.3e-03; %[H] with N=150, L=8-10 mH
R = 0.641; %[Ohm]
RC = 1; %[Ohm] 1, 10000
RD = 10000; %[Ohm]
```

Open Current Loop

```
a1 = RB*CB;
a0 = 1;
b1 = RA*L*CB;
b0 = CB*RA*(R+RC);
numGH_ol = [a1 a0]; %Numerator
denGH_ol = [b1 b0]; %Denominator
% GH = tf(numGH,denGH);
% GHzpk = zpk(GH);
```

Closed Current Loop

```
c1 = RB*CB*RD;
c0 = RD;
d2 = RA*L*CB*RD;
d1 = CB*(RA*RB*RC+RA*RD*(R+RC));
d0 = RA*RC;
```

```
numGH_c1 = [c1 c0]; %Numerator
denGH_c1 = [d2 d1 d0]; %Denominator
```

Gamp

```
C2 = RB*CB*RD*L;
C1 = RD*L + RD*RB*CB*R;
C0 = RD*R;
D2 = RA*L*CB*RD;
D1 = CB*(RA*RB*RC+RA*RD*(R+RC)-RB*RD^2);
D0 = RA*RC - RD^2;
```

Korean Amplifier

```
A1 = 3000;
A0 = 210000;
B2 = 1;
B1 = 3600;
B0 = 210000;
```

AMB

```
m = 0.5; %[kg] modal mass of rotor inside AMB
d1 = .0315;%[m] inner diameter actuator path
d2 = .1045;%[m] outer diameter actuator path
h_act = .002+.0255 + (8.5e-03)/2;%[m] height of actuator pole path
N = 250; %number of coil turns 250
% I_B = 1.4; %[Amps] bias current 1.4
% Imax = 2*I_B; %[Amps] max current
g_o = .0005; %[m] nominal air gap
mu_o = 4*pi*10^(-7); %air permeability
mu = 5000; %permeability of core
d_cu = .037*100; %copper coil diameter
l_cu = (2*10.962)*100; %copper coil length 10.962

% Core
l_c = (pi*d1/8) + (pi*d2/8) + 2*h_act; %length of actuator path
A_c = 2.975e-04; %cross section area of actuator
R_c = l_c/(A_c*mu); %Actuator reluctance
```

```matlab
% Rotor Mass
% lr = ; %length of rotor mass path
% A_r = ; %cross section area of rotor mass
% R_r = lr/(A_r*mu); %Rotor mass reluctance

% Air gap
% lg = ; %length of air gap [will be changing, approximate at nominal air gap]
A_g = A_c*1.05; %cross section area of air gap
% R_g = lg/(A_g*mu); %Rotor mass reluctance

Lcu = (2.54*(d_cu^2)*N^2)/(18*d_cu + 40*l_cu)*10e-06; %[micro-H,(with cm)], Horowitz Pg. 28
R = 2*.0465; %copper resistance
b = 35*10^-3; % [m] core thickness
c = 8.5*10^-3; % [m] leg width
alpha = 22.5; % [deg] for radial bearing with 4 pole pairs
A = c*b; % [m^2] "opposing area of an electromagnet" core pole
eps = 0.8; % leakage and fringing correction factor for radial bearing
           % included in Ch.3 of 'Control of Surge in Centrifugal
           % Compressors by Active Magnetic Bearings' book
Bmax = 1.2;
% [2.038 1.7 1.7 1.702 1.7 1.7 1.498...
%        1.495 1.293 1.291]'; %M19 19mil Bmax for [0,50,50,10,150,200,300,400,600,1000]Hz
Bknee = 0.88;
I_B = g_o*Bknee./(mu_o*N);
ix = I_B; % [A] perturbation current. ix must be < i0. Here it is set to i0 for
          % worst case.
Imax = 2*I_B; %[Amps] max current
x = 0.358*10^-3; % [m] rotor displacement (set to nominal air gap for worst case)

% Stiffness Coefficients
ki = (eps*mu_o*A_g*(N^2)*(I_B))/(g_o^2); %[N/m] current stiffness
K = 0.25*mu_o*N^2*A ; % Schweitzer Pg. 80
ki_A = 4*eps*K*I_B.*cosd(alpha)/(g_o)^2; % Schweiter Pg. 80
ks = (eps*mu_o*A_g*(N^2)*(I_B.^2))/(g_o^3); %[N/m] position stiffness
ku = ki; % Schweitzer Pg. 48, motion induced voltage stiffness
M_eff = 0.5; %[kg]
FgenMAX = ki.*ix-ks.*x % Schweitzer equation (3.27)

Lc1 = ki_A.^2/abs(ks); % Schweitzer Pg. 48
Lc2 = (mu_o*(N^2)*A_g)/(2*g_o); % Yoon Pg. 67, Control of Surge, also Schweitzer Pg. 77
R = .36; %[Ohms] resistance of copper wire per actuator
Vc = 40;
Vmax = 80;
didt = (2*g_o*Vc)/(mu_o*N^2*A); %neglecting magnetic permeability and coil resistance
MAXdidt = (2*g_o*Vmax)/(mu_o*N^2*A) % max slew rate, neglecting iron reluctance and coil
resistance (eq. 3.39 in Yoon text).
MAXdFdt = 2*eps*I_B.*Vmax/g_o % Max time rate of change of the magnetic force that can be applied
to the rotor  (eq. 3.40 in Yoon text)
```

```
% Vc1 = didt*Lc1
% Vc2 = didt*Lc2
Vc1max = MAXdidt*Lc1;
Vc2max = MAXdidt*Lc2;
% VLc3 = MAXdidt*Lc3;
Psat = Bmax^2/(2*mu_o);
Fsat = 2*cosd(alpha)*Psat*A;
% ki_sat = (4*Fsat*I_B)/(Imax);
% Lc3 = (2*g_o*ki_sat)/(cosd(alpha)*I_B); % Schweitzer Pg. 338
```

```
FgenMAX =

   43.7361


MAXdidt =

   3.4238e+03


MAXdFdt =

   3.5854e+05
```

Feedback Proximity Sensor

```
Gprox = 7.87; %[Volts/m] gain 7870
% Gb = ; %[Volts] bias
```

Delay

```
T_delay = .0001; %[sec] 1-2 times sampling rate of 5-10kHz
s = tf('s');
sys = exp(-T_delay*s);
sysx = pade(sys,3)
```

```
sysx =

  -s^3 + 120000 s^2 - 6e09 s + 1.2e14
  ---------------------------------
```

```
  s^3 + 120000 s^2 + 6e09 s + 1.2e14

Continuous-time transfer function.
```

PID Control

```
KP = 1; %Proportional
KI = 0; %Integral
KD = 0; %Derivative
% G_PID = tf([KD KP KI],[1])
% A = 223872; %Amp Gain
Vin = 1.5;%Voltage Source
FDis = 15
```

```
FDis =

    15
```

Op Amp Tests

```
time_sim = 5; %[sec]
% Tp = .001; %peak time
% Ts = .001; %settling time
% pos = 5; %percentage overshoot
% z = -log(pos/100)/sqrt(pi^2+(log(pos/100)^2)); %zeta, damping ratio
% % w_lp = pi/(Tp*sqrt(1-z^2)); %[rad/sec] low-pass frequency with Tp
% w_lp = 4/(Ts*z); %[rad/sec] low-pass frequency with Ts
% numGH = [1.8844e07]; %Numerator
% denGH = poly([1 5990.54 1.8844e07]); %Denominator
% GH = tf(numGH,denGH);
% GHzpk = zpk(GH);
```

Control Loop

MATLAB

a1 = 2; a0 = 10000; b2 = .03; b1 = 30000; b0 = 1e08; T_amp = tf([a1 a0],[b2 b1 b0]) G_amp = tf([L*T_amp + R*T_amp],[1-T_amp*Rf]) G_AMP = tf([G_amp],[L (R+G_amp*Rf)]) T_AMB = tf([G_PID*G_AMP*ki],[m ku*ki*G_PID*G_AMP (Gprox*G_PID*G_AMP*ki+ks)])

Simulink

Op-Amp A = L*T_amp; B = R*T_amp; C = 1-T_amp;

```
% Discrete
% T_Hz = 2*10^6; %[Hz] sampling time
% T_s = inv(T_Hz); %[Hz] sampling time
% T_AMBd = tf([T_amp*ki],[m T_amp*ki*ku/G_amp T_amp*ki*Gprox+ks],'Input Delay',0.3);
% T_AMBdd = c2d(T_AMBd,T_s,'zoh')

% FDis = 60; %[N] disturbance force
% sim('AMBSystem')
% open_system('AMBSystem')
% sim('AMP')
% open_system('AMP')
% sim('DiscreteAMB')
% open_system('DiscreteAMB')
```

Plots

figure('Name','X-direction AMB Force vs. Omega') plot(omega_rpm,F3x) ylabel('Force [N]') xlabel('Omega [RPM]') % axis([300,3000,0,100]) % legend('Sim Inboard','Sim Outboard','Exp Inboard','Exp Outboard','Location','east')

figure('Name','Y-direction AMB Force vs. Omega') plot(omega_rpm,F3y) ylabel('Force [N]') xlabel('Omega [RPM]') % axis([300,3000,0,100]) % legend('Sim Inboard','Sim Outboard','Exp Inboard','Exp Outboard','Location','east')

```
% figure('Name','Actuator Response')
% plot(tout(:,1),simout2(:,1),'k')
% ylabel('Displacement [m]')
% xlabel('Time [sec]')
% % axis([0,3,0,.01])
```

```matlab
% figure('Name','Korean Amp Response')
% plot(tout(:,1),simout(:,1),'k',[0,5],[-1,-1],'b')
% ylabel('Displacement [m]')
% xlabel('Time [sec]')
% axis([0.98,1.2,-1.4,0])

% figure('Name','Amp Response')
% plot(tout(:,1),simout(:,1),'k')
% ylabel('Displacement [m]')
% xlabel('Time [sec]')
% axis([0.98,1.2,-0.95,0])

% figure('Name','Discrete')
% plot(tout(length(simout),1),simout(:,1),'k')
% ylabel('Displacement [m]')
% xlabel('Time [sec]')
% axis([0.98,1.2,0.95,1.05])
```

Published with MATLAB® R2015a

ADAMS Control

Wipe the Slate

clc clear all close all

AMB Parameters

```
M = 0.5; %[kg] modal mass of rotor inside AMB
N = 300; %number of coil turns 250
g_o = .0005; %[m] nominal air gap
x = 0.358*10^-3; % [m] rotor displacement (set to nominal air gap for worst case)
mu_o = 4*pi*10^(-7); %air permeability
% mu = 5000; %permeability of core
Bmax = 1.2;
Bknee = 0.88;
I_B = g_o*Bknee./(mu_o*N);
% I_B = 1.4; %[Amps] bias current
Imax = 2*I_B; %[Amps] max current
B = mu_o*N*I_B/(2*g_o);    % [T] nominal flux density in core
b = 35*10^-3; % [m] core thickness
c = 8.5*10^-3; % [m] leg width
alpha = 22.5; % [deg] for radial bearing with 4 pole pairs
```

```
A_c = c*b; % [m^2] "opposing area of an electromagnet" core pole
A_g = A_c*1.05; %cross section area of air gap
eps = 0.8; % leakage and fringing correction factor for radial bearing
           % included in Ch.3 of 'Control of Surge in Centrifugal
           % Compressors by Active Magnetic Bearings' book
```

Stiffness Equations

```
Ki = (eps*mu_o*A_g*(N^2)*(I_B))/(g_o^2); %[N/A] current stiffness
K = 0.25*mu_o*N^2*A_c ; % Schweitzer Pg. 80
Ki_A = 4*eps*K*I_B.*cosd(alpha)/(g_o)^2; % Schweiter Pg. 80
Ku = Ki; % Schweitzer Pg. 48, motion induced voltage stiffness
Ks = (eps*mu_o*A_g*(N^2)*(I_B.^2))/(g_o^3); %[N/m] position stiffness
```

Amplifier

```
R = 0.6410; %copper resistance%[ohms]
Lc1 = Ki_A.^2/abs(Ks); %[mH] Schweitzer Pg. 48
Lc2 = (mu_o*(N^2)*A_g)/(2*g_o); %[mH] Yoon Pg. 67, Control of Surge, also Schweitzer Pg. 77
```

Feedback Proximity Sensor

```
Gprox = 7.87; %[Volts/m] gain 7870
KYprox = Gprox;
KXprox = Gprox;
```

Ampflifier Circuit Parameters

```
R1 = 50000;
R2 = 20000;
R4 = 5000;
R5 = 10000;
R6 = 500000;
R7 = 500000;
C7 = .05e-06;
Rpot3 = 160; %6000
Rpot2 = 50;
RA = 10000; %[Ohm]
```

```
% Ra = 20000; %[Ohm] max without Rb
% Rb = 20000; %[Ohm] 500,000 max
% RB = Ra*Rb/(Ra+Rb); %[Ohm]
RB = 20000; %[Ohm]
Ca = 0.01e-06; %[F]
Cb = 0; %[F] 0.8e-06
CB = Ca + Cb; %[F]
L = 35.3e-03; %[H] with N=150, L=8-10 mH
R = 0.641; %[Ohm]
RC = 10000; %[Ohm] 1
RD = 10000; %[Ohm]

% %% Servo Drive
% c1 = R2*C2*Rf;
% c0 = Rf;
% d2 = R1*L*C2*Rf;
% d1 = C2*(R1*R2*Rs+R1*Rf*(R+Rs));
% d0 = R1*Rs;
% numGH_cl = [c1 c0]; %Numerator
% denGH_cl = [d2 d1 d0]; %Denominator
```

Closed Current Loop

```
c1 = RB*CB*RD;
c0 = RD;
d2 = RA*L*CB*RD;
d1 = CB*(RA*RB*RC+RA*RD*(R+RC));
d0 = RA*RC;
numGH_cl = [c1 c0]; %Numerator
denGH_cl = [d2 d1 d0]; %Denominator
```

Gamp

```
C2 = RB*CB*RD*L;
C1 = RD*L + RD*RB*CB*R;
C0 = RD*R;
D2 = RA*L*CB*RD;
D1 = CB*(RA*RB*RC+RA*RD*(R+RC)-RB*RD^2);
D0 = RA*RC - RD^2;
```

Korean Amplifier

```
A1 = 3000;
A0 = 210000;
B2 = 1;
B1 = 3600;
B0 = 210000;

% %% Delay
% T_delay = .0001; %[sec] 1-2 times sampling rate of 5-10kHz
% s = tf('s');
% sys = exp(-T_delay*s);
% sysx = pade(sys,3);
```

PID Control

```
KP = 1; %Proportional
KI = 0; %Integral
KD = 0; %Derivative

Vref = I_B;%Voltage Source
YTBias = .02;
YBBias = .02;
XLBias = .02;
XRBias = .02;

% Discrete
% T_Hz = 2*10^6; %[Hz] sampling time
% T_s = inv(T_Hz); %[Hz] sampling time
% T_AMBd = tf([T_amp*ki],[m T_amp*ki*ku/G_amp T_amp*ki*Gprox+ks],'Input Delay',0.3);
% T_AMBdd = c2d(T_AMBd,T_s,'zoh')

% timeSim = 5; %[sec]
% sim('AMBModel')
% open_system('AMBModel')
%
% %% Plots
% figure('Name','Amp Response')
% plot(tout(:,1),simout1(:,1),'k',[0,5],[1,1],'r')
% ylabel('Displacement [m]')
% xlabel('Time [sec]')
% axis([0.6,1.4,-.1,2])

% figure('Name','Amp Response')
```
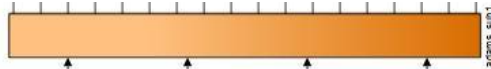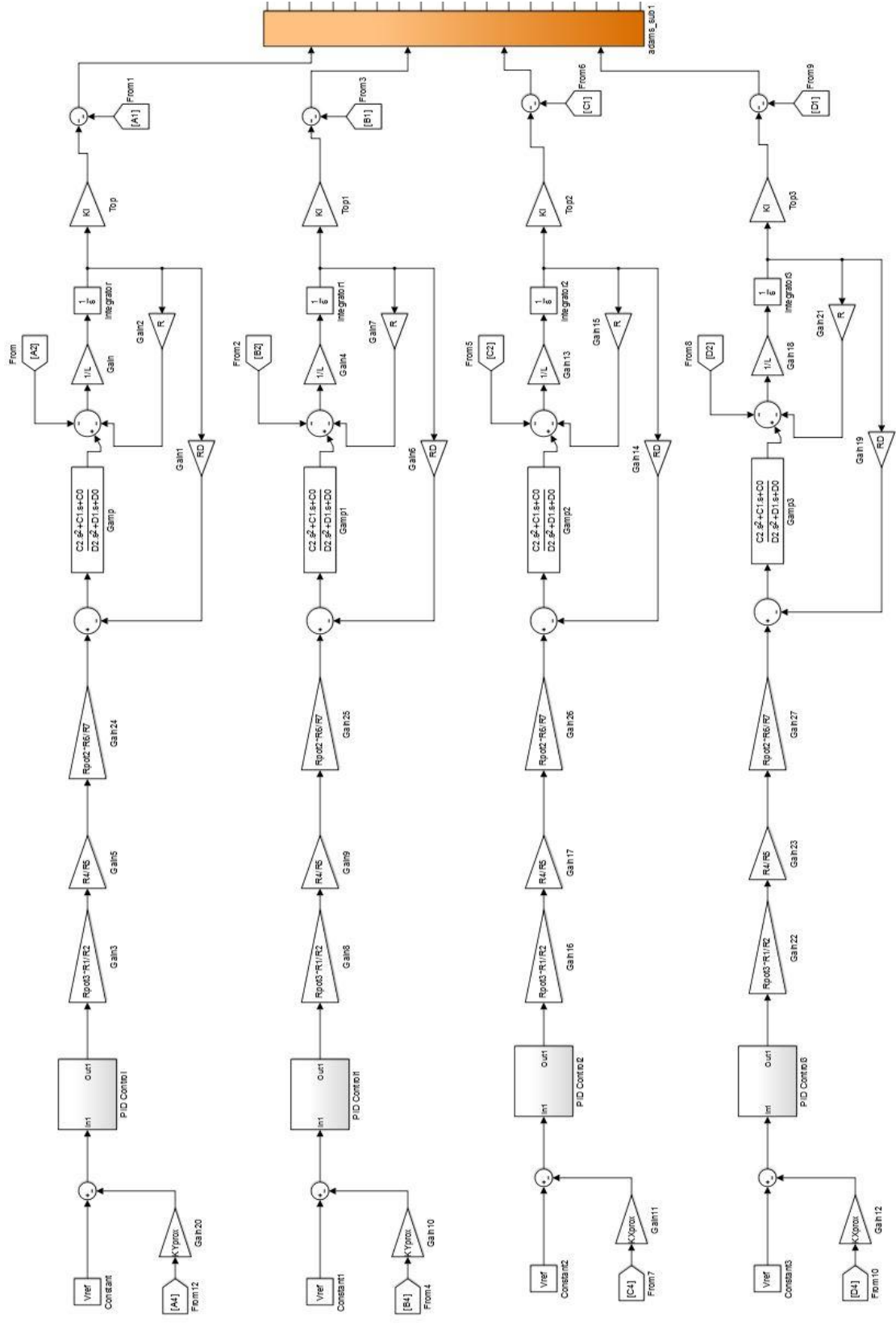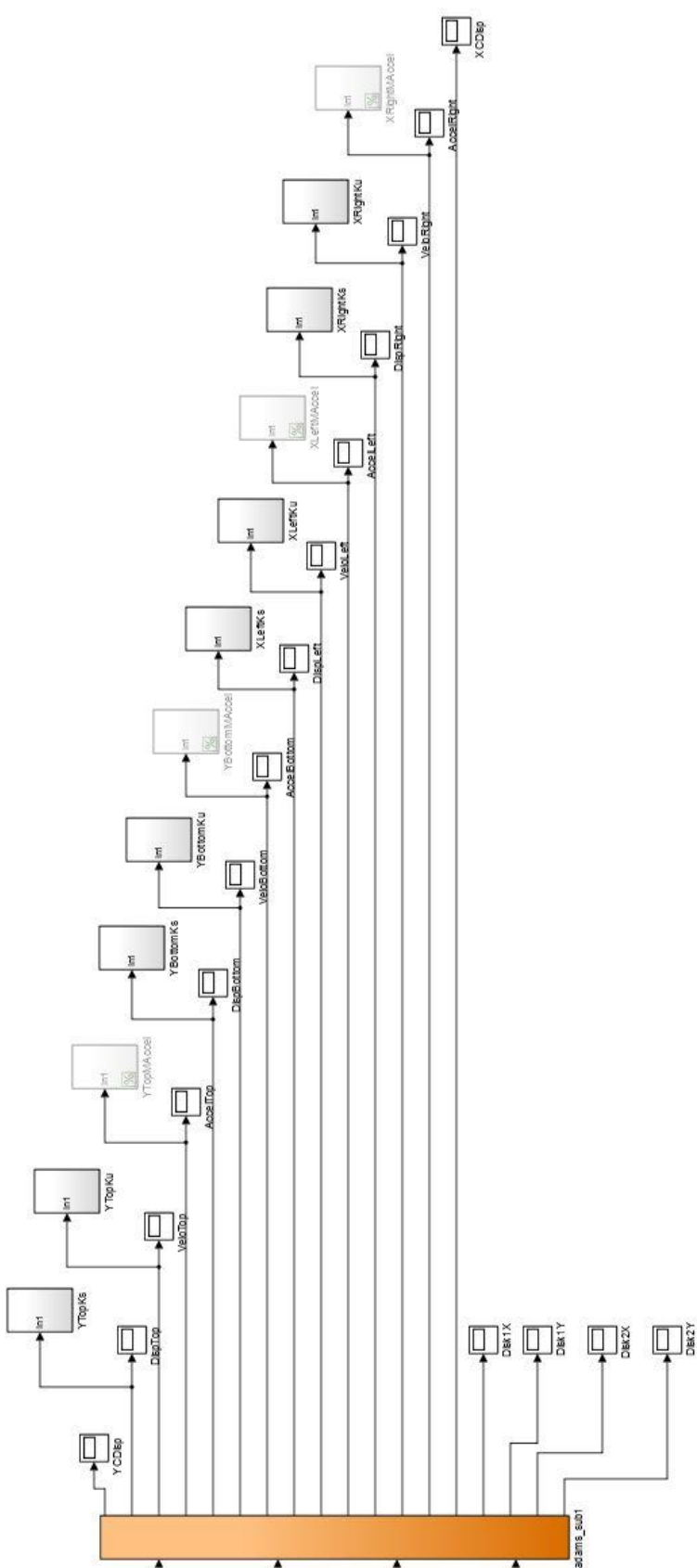
```
% plot(tout(:,1),simout2(:,1),'k')
% % ,[0,5],[1,1],'r')
% ylabel('Displacement [m]')
% xlabel('Time [sec]')
% % axis([0.6,1.4,-.1,1.1])
```

Published with MATLAB® R2015a

Potential Failure Mode and Effects Analysis: Active Magnetic Bearing

S - Severity

O - Occurrence

Item or Function	Potential Failure Mode	Potential Effects of Failure	S (0-10)	Potential Causes of Failure	O (0-10)	Current Design Controls	Recommended Actions
1) Suspends the RK4 Bently rotor kit shaft	1) Excess rotor shaft displacement	1) Interference leading to destruction of stationary peripheral parts	9	1) Excess unbalance of rotor disks	5	1) Rotor balanced to maintain max displacement of 40 mil-pp	1) Balance and calibrate rotor to minimum deflection on two support journal bearings
2) Reduces rotor vibration with active digital control	2) Excess of rotor expansion	2) Interference leading to destruction of stationary peripheral parts	9	2) Rotor is running beyond specified speed limit	1	2) 10,000 RPM max motor speed, 3,000-6000 RPM recommended speed	2) Initial tests at no roll, slow roll, and ramp up based on initial performance
3) Provides user with realtime data and interaction	3) Overload of bearing (over current of bearing coil)	3) Underperformance, loss of control of rotor	8	3) Load capacity under-estimated, copper wire design not sufficient	3	3) Safety factor of 3 based on total load capacity used to size performance parameters	3) Test at slow speeds, monitor current and flux density of rotor, test through critical speed
	4) Overheating of bearing	4) Melt components, effect flux density of stator	8	4) Not properly cooled, excessive inductance from copper wiring	5	4) Auxiliary fan to increase convection rate	4) Keep constant running fan next to bearing assembly during operation
	5) Overspeed of bearing	5) Unstable, lose control of rotor, damage inboard motor	10	5) User runs rotor beyond speed limit	1	5) Run motor at recommended speed, maintain run-time under 10 minutes	5) Operate rotor below 6000 RPM until several successful runs are confirmed
	6) Power supply defect	6) Loss of power, lose control of rotor	6	6) Power outage, faulty wiring, overload of power supply	1	6) Touchdown bearing to catch rotor while ramping down in speed	6) Spec power supply to be robust, separate power supplies for computer and op-amps
	7) Overheating of DSP and amplifiers	7) Decrease of performance, melt hardware components	6	7) Undersizing of hardware, excessive power through components	6	7) Output current of Amplifier spec. to safety factor 3 of max actuator current, separate power supplies for power amps and computer	7) Operate unit at low speed if excess rotation is occurring. This will cause higher current draw. Monitor and try to maintain low current for each amp
	8) Unstability of rotor	1) Interference leading to destruction of stationary peripheral parts	8	8) Digital system not calibrated properly, delays and lag time,	9	8) Touchdown bearing for frequent trial and error testing	8) Touchdown bearing with inner diameter at 1/2 air gap of AMB stator

Appendix I

	Invoice	POLARIS LASER LAMINATIONS, LLC.

Polaris Laser Laminations, LLC
2725 Norton Creek Drive, Unit B2
West Chicago, IL 60185
Phone: (888) 477-1969
Fax: (630) 444-0761
Email: lgirard@polarislaserlaminations.com

A Reliable Resource for Your Business

Date	Invoice #
3/18/2016	10937

PAID 03/18/2016

Bill To	Ship To
Sean Fowler Cal Poly Mechanical Engineering c/o Moncerratt Peralta 1 Grand Avenue San Luis Obispo, CA 93407	Sean Fowler c/o Cal Poly Mustang '60 Machine Shop 1 Grand Avenue San Luis Obispo, CA 93407

P.O. Number	Terms	Via	F.O.B.
Mocerratt E-Mail	Credit Card	UPS Ground PPD	Origin

Quantity	Description	Price Each	Amount
1	(G29)StatorCalPolyMagneticBearing.DWG, 29 ga M19 C5 to be supplied by Polaris. Units are in 1.378" high bonded stack. Bond with EB-548.	855.00	855.00
1	(G29)RotorCalPolyMagneticBearing.DWG, 29 ga M19 C5 to be supplied by Polaris. Units are in 1.535" high bonded stack. Bond with EB-548.	789.00	789.00
1	UPS Ground shipping charge.	27.01	27.01

Total	**$1,671.01**
Payments/Credits	**-$1,671.01**

Appendix J

National Instruments cRIO-9063 FPGA controller quote.

ALSO SEE the following downloadable documents from National Instruments (also included on the project Google Drive under DAQ>LabVIEW):

- NI LabVIEW for CompactRIO Developer's Guide
- User Manual NI cRIO-9063
- Specifications NI cRIO-9063

NATIONAL INSTRUMENTS

Cameron Naugle
California Polytechnic State University - San Luis Obispo
316 Leroy Ct.
SAN LUIS OBISPO, CA 93405
UNITED STATES

Quotation Date: 20-APR-2016
Quote Valid Until: 20-MAY-2016
Phone: (916) 5179331
Fax:
Contact No: 8549362

Quotation No. 2293678

Please indicate the above quote number when ordering for faster processing. Contact us at (800) 433-3488, or submit orders to orders@ni.com.

Line No.	Part Number	Description	Qty.	Unit Price	Discount	Amount
1	783830-01	cRIO-9063, 4-Slot Integrated 667 MHz Dual-Core Controller and Artix-7 FPGA Standard Delivery time: 12 - 20 business days ARO. *Country of Origin: Malaysia*	1	~~1,299.00~~ 1,169.10	10.00%	1,169.10
2	151733-02	Cable Assembly, Cat-5E Ethernet, Thin Profile, 2M Standard Delivery time: 10 - 15 business days ARO. *Country of Origin: China*	1	~~9.00~~ 8.10	10.00%	8.10
3	779473-01	NI 9901 Desktop Mounting Kit Standard Delivery time: 5 - 10 business days ARO. *Country of Origin: China*	1	~~53.00~~ 47.70	10.00%	47.70

Sub-Total:	$ 1,361.00	10.00%	$ 1,224.90
Shipping and Handling:			$ 20.65
Total:			$ 1,245.55

Currency quoted in: U. S. Dollars

Appendix K

Part Drawings
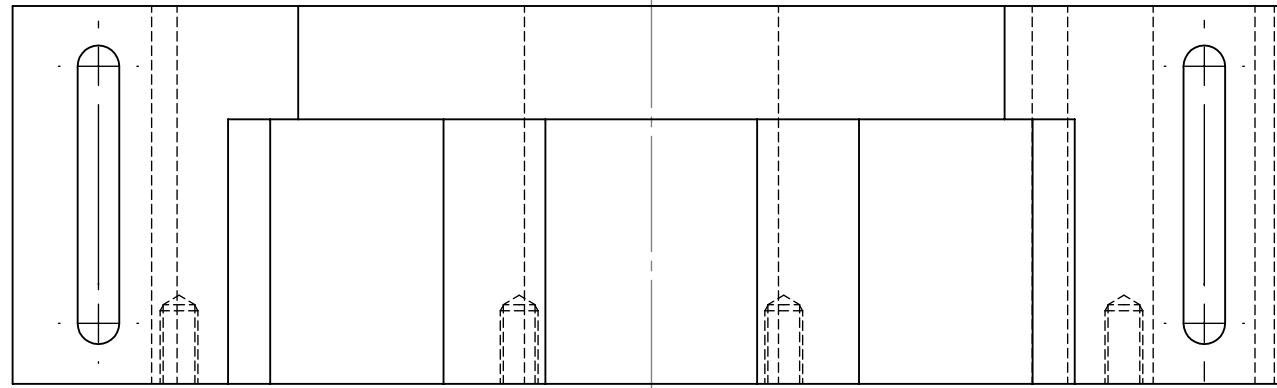
NOTES:

*DISCUSS PART WITH DESIGNER PRIOR TO MACHINING

*ALL DIMS INCLUDED ARE "CRITICAL"

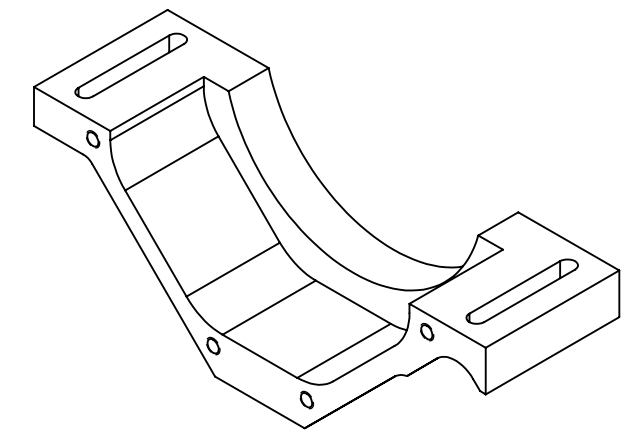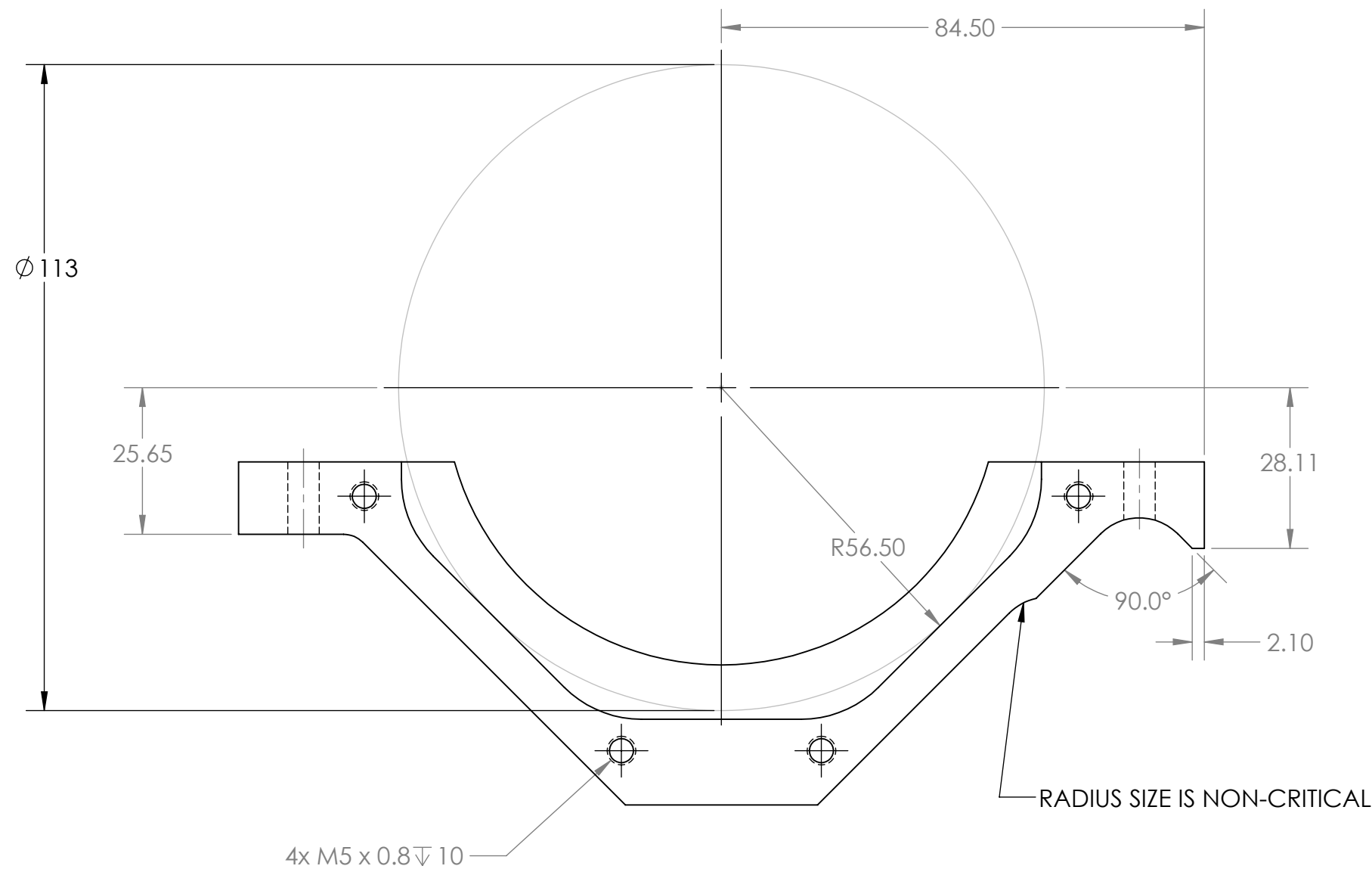UNLESS OTHERWISE SPECIFIED:
1. ALL DIMS. IN MILLIMETERS
2. TOLERANCES:
   X.XX ±0.05
   ANGLES = ±0.5°
3. MATERIAL: AL - 6061
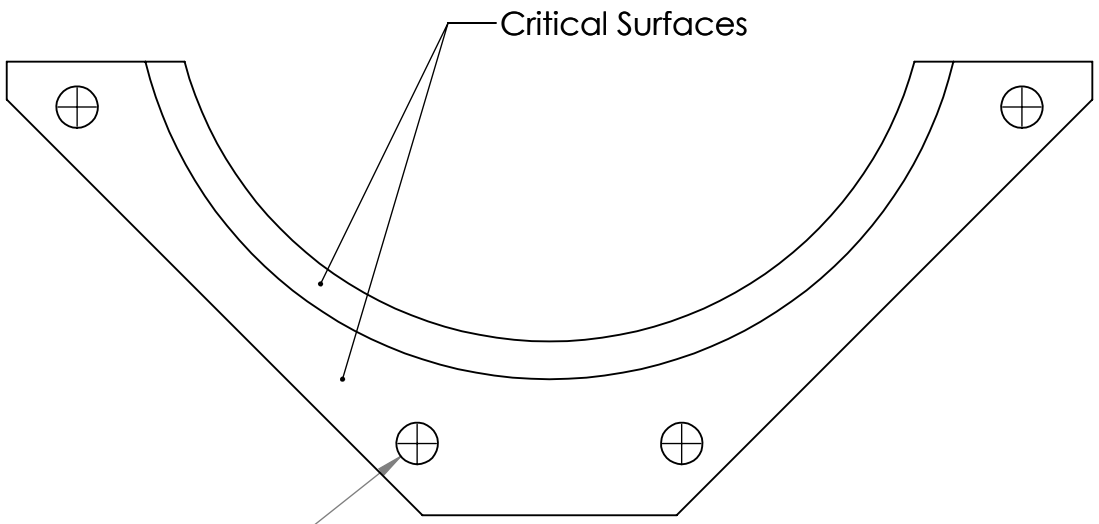4. QUANTITY: 1
5. STOCK SIZE: 10-12" x 3" x 2.5"

84.50

⌀ 113

25.65

28.11

R56.50

90.0°

2.10

4x M5 x 0.8 ⍌ 10

RADIUS SIZE IS NON-CRITICAL

ISO SCALE: 1:2

Cal Poly Mechanical Engineering	PHONE: 858-354-7763	Title: STATOR BASE		Drwn. By: SEAN FOWLER
ME 429 - WINTER 2016	sefowler@calpoly.edu	Date: 3/17/2016	Scale: 1:1	Chkd. By: GARRETT OLSON

Critical Surfaces

4 x ⌀ 5.2 THRU-ALL
(M5 Clearance Hole. Use #6 drill bit)

ISO SCALE 1:2

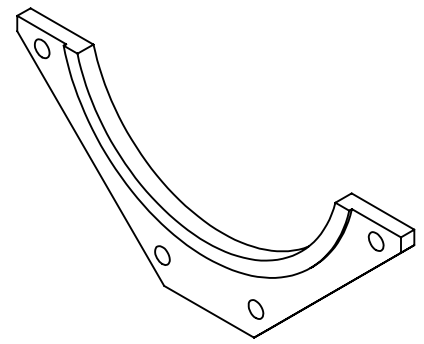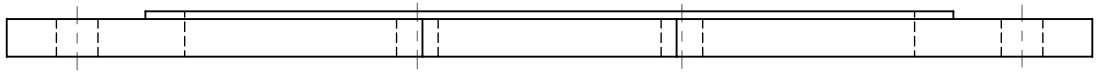| Cal Poly Mechanical Engineering	PHONE: 858-354-7763	Title: STATOR BASE COVER PLATE	Drwn. By: SEAN FOWLER
ME 429 - WINTER 2016	sefowler@calpoly.edu	Date: 3/17/2016	Scale: 1:1	Chkd. By: GARRETT OLSON

NOTES:
*DISCUSS PART WITH DESIGNER
 PRIOR TO MACHINING

UNLESS OTHERWISE SPECIFIED:
1. ALL DIMS. IN MILLIMETERS
2. TOLERANCES:
    X.XX ±0.10
    ANGLES = ±1°
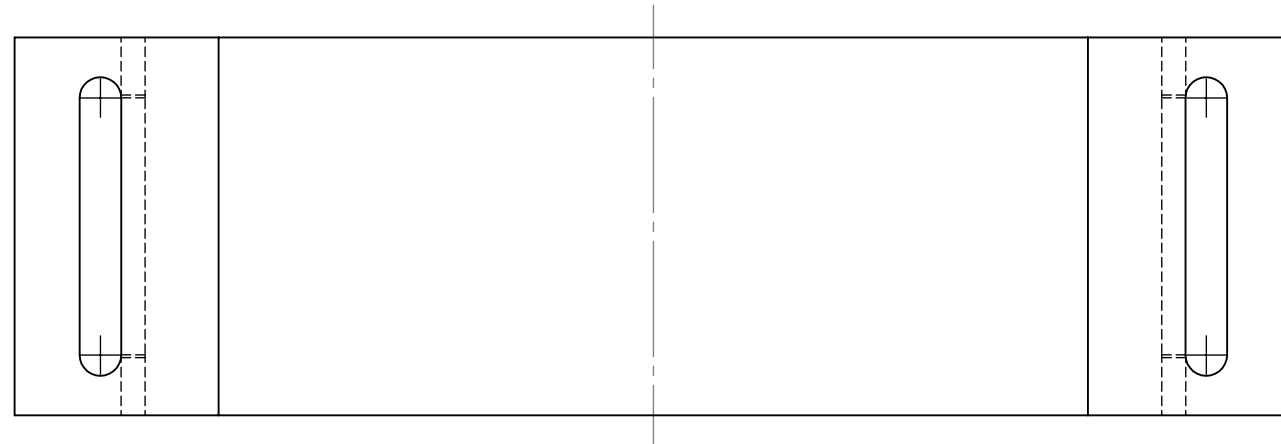3. MATERIAL: AL - 6061
4. QUANTITY: 1
5. STOCK SIZE: 10-12" x 3" x 2.5"
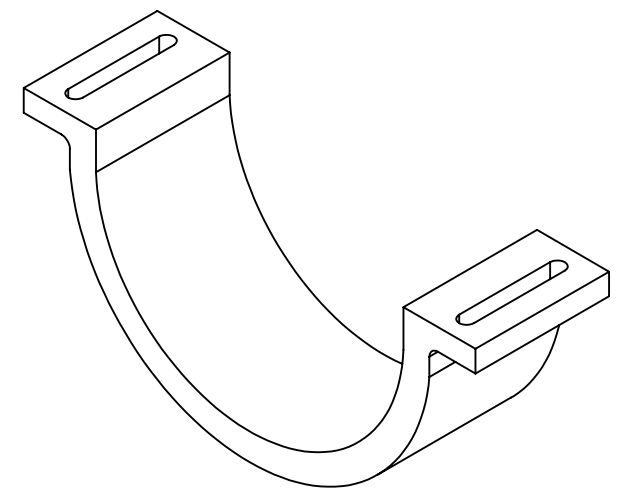
ISO SCALE 1:2
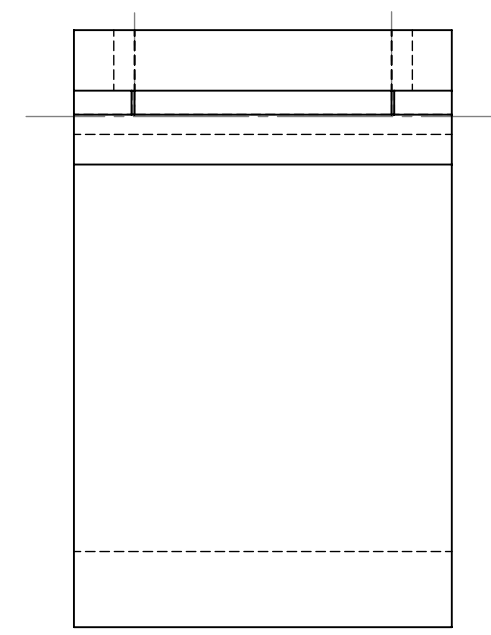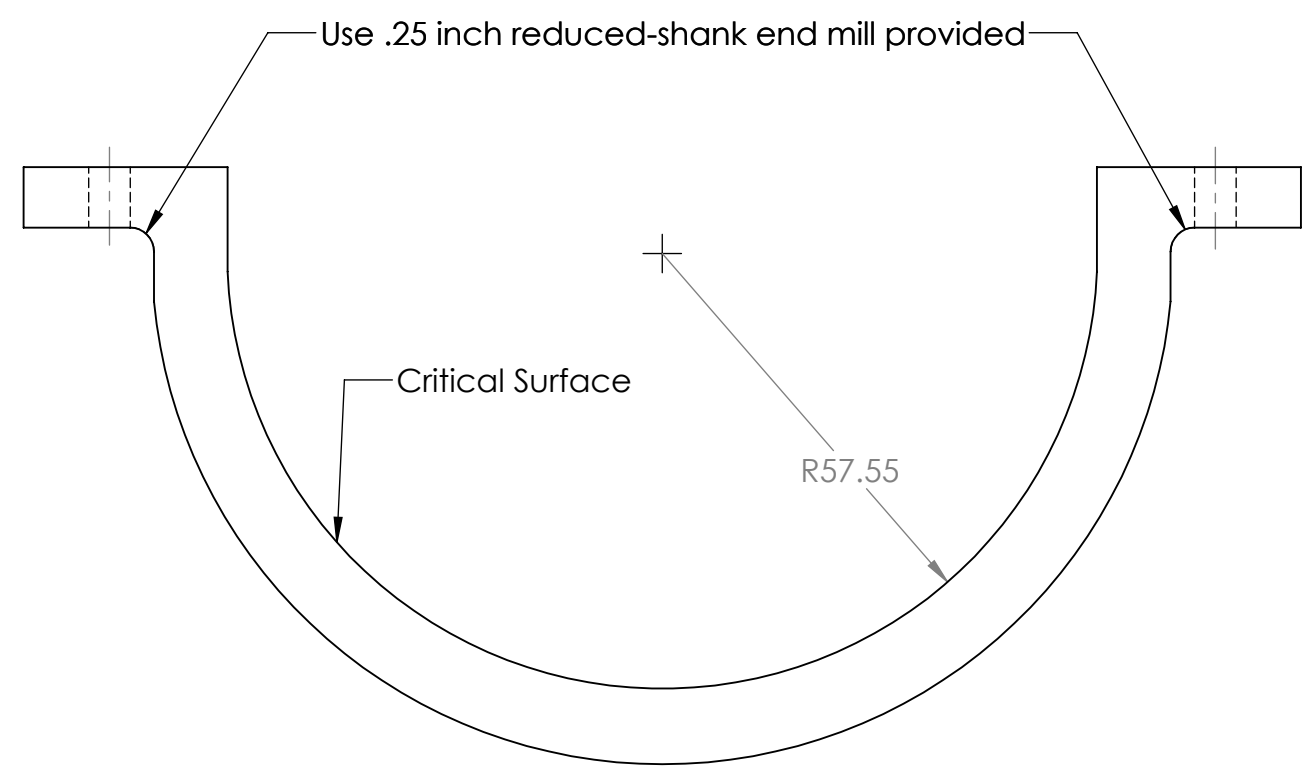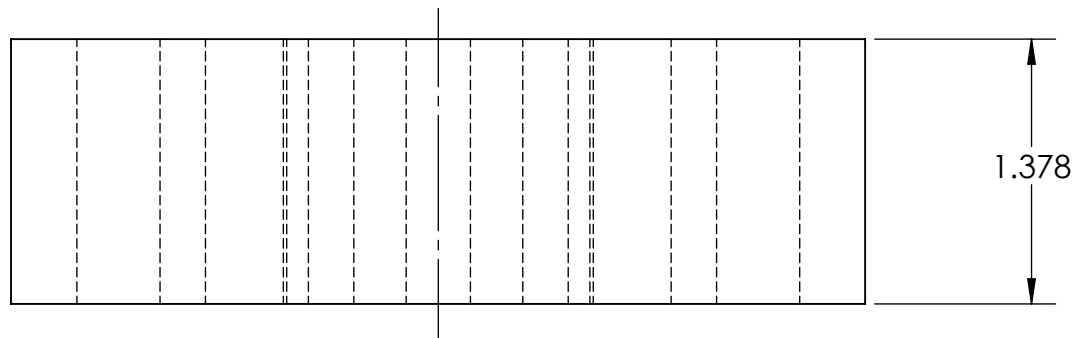
Use .25 inch reduced-shank end mill provided

Critical Surface

R57.55

1.378

⌀4.449

⌀1.614±.001

⌀3.780

8 x 45°

8 x .335

ISOMETRIC VIEW

1.378

$\emptyset$ .906

$\emptyset$ 1.575 ± .001
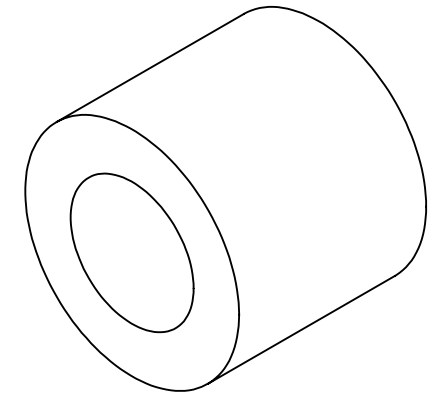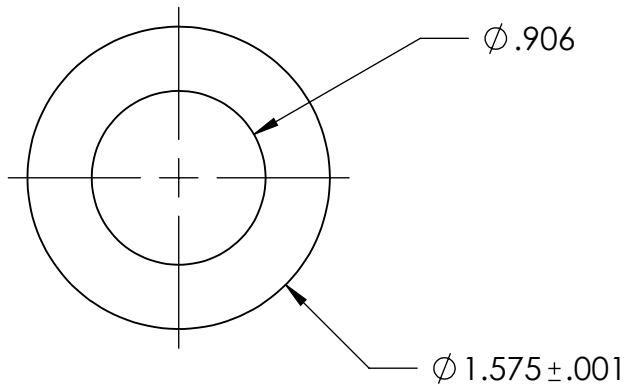
ISOMETRIC VIEW

Appendix L

Concept Sketch
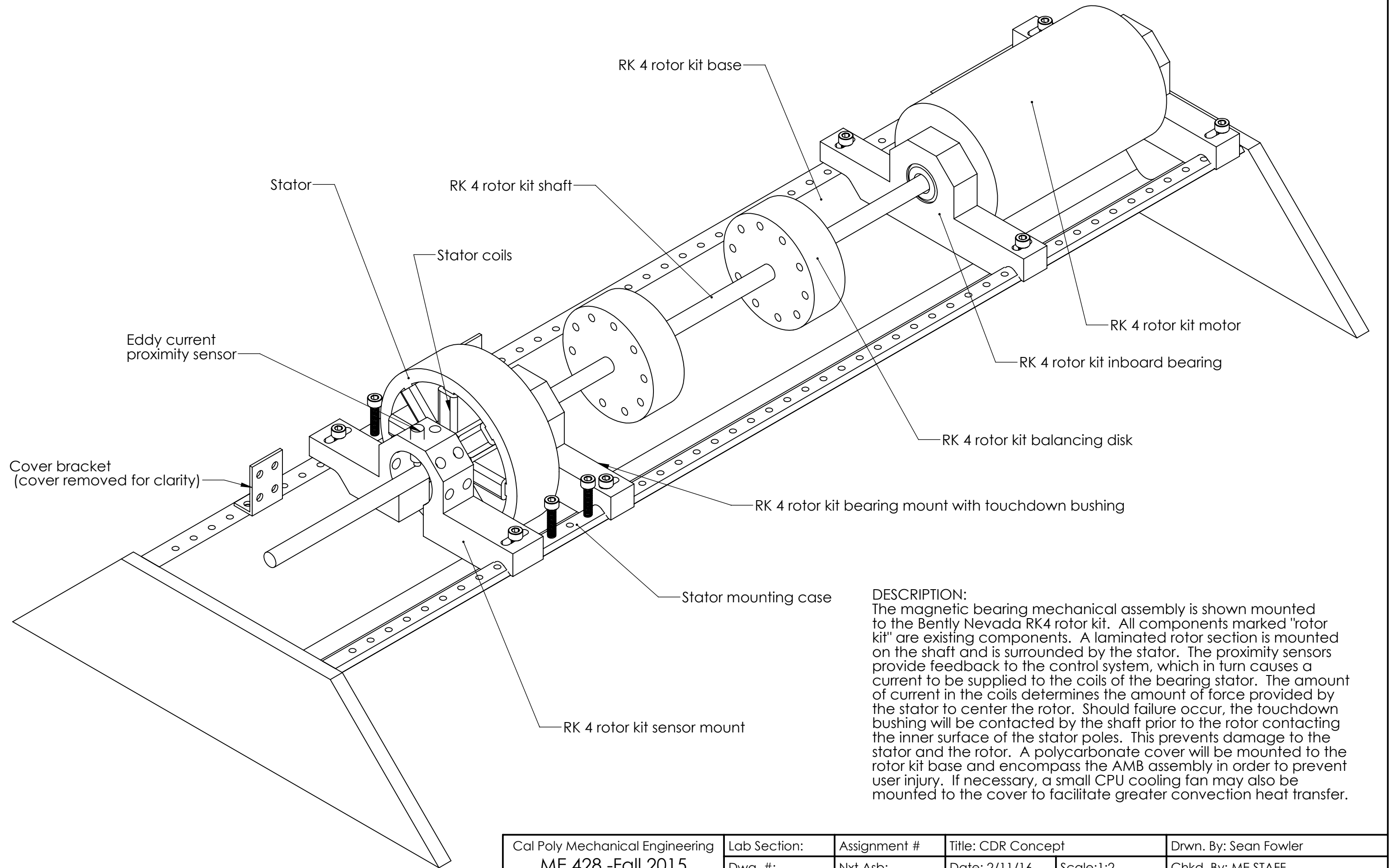
RK 4 rotor kit base

RK 4 rotor kit shaft

Stator

Stator coils

Eddy current
proximity sensor

RK 4 rotor kit motor

RK 4 rotor kit inboard bearing

Cover bracket
(cover removed for clarity)

RK 4 rotor kit balancing disk

RK 4 rotor kit bearing mount with touchdown bushing

Stator mounting case

RK 4 rotor kit sensor mount

DESCRIPTION:
The magnetic bearing mechanical assembly is shown mounted
to the Bently Nevada "rotor kit. All components marked "rotor
kit" are existing components. A laminated rotor section is mounted
on the shaft and is surrounded by the stator. The proximity sensors
provide feedback to the control system, which in turn causes a
current to be supplied to the coils of the bearing stator. The amount
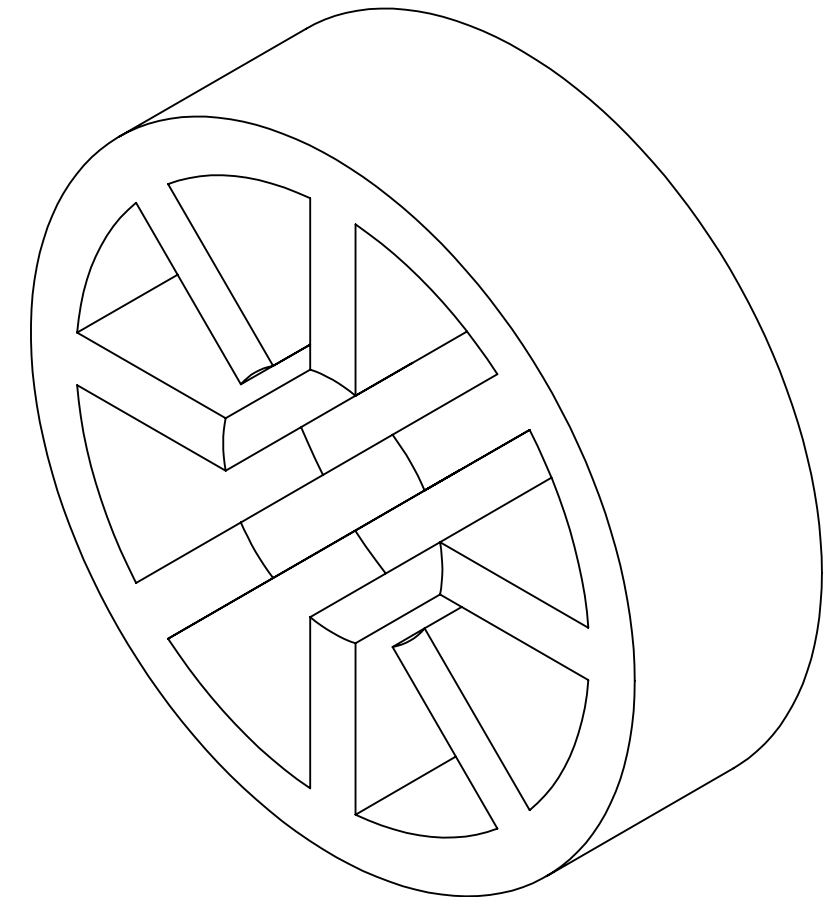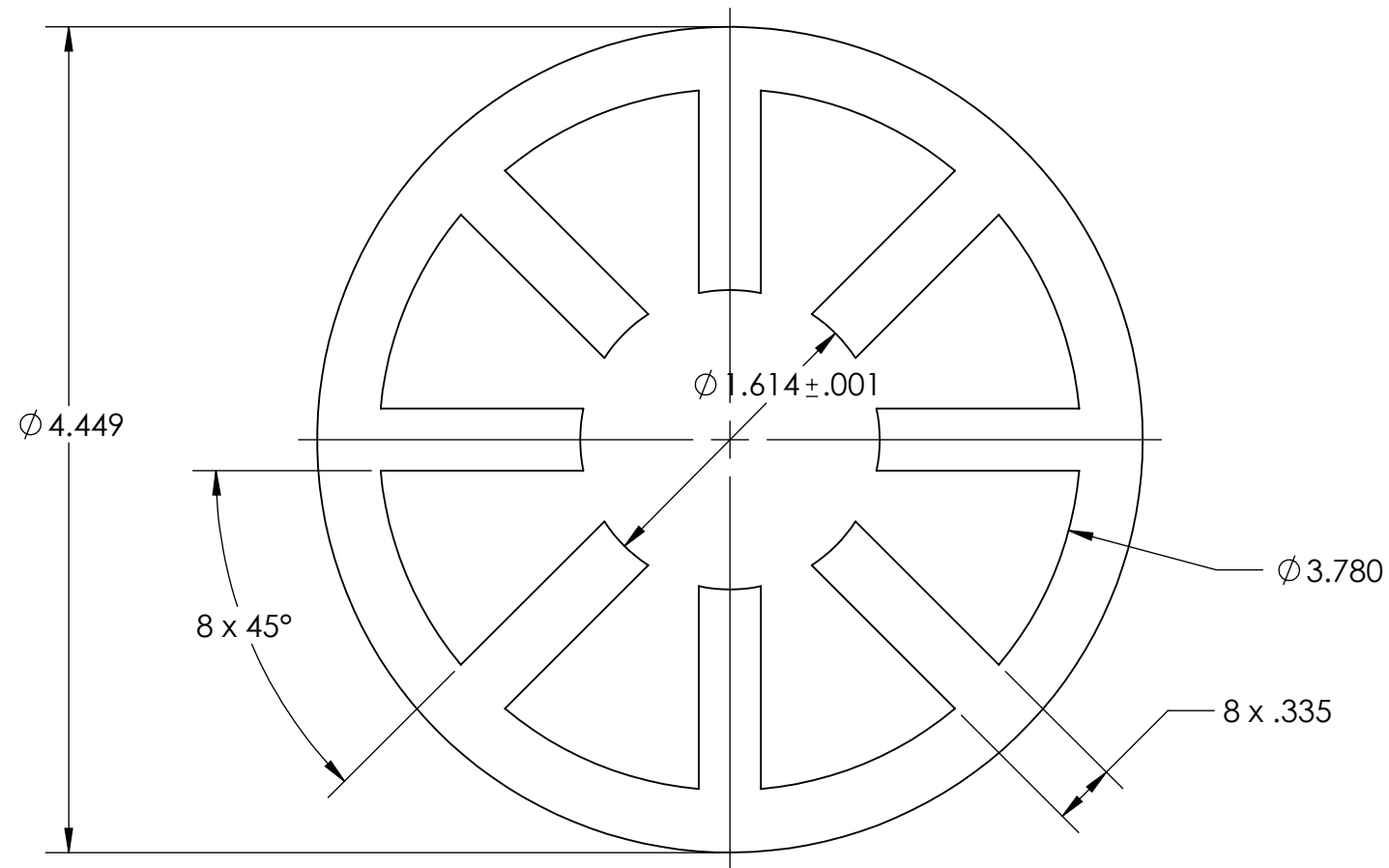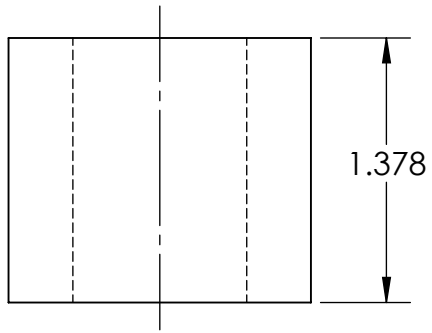of current in the coils determines the amount of force provided by
the stator to center the rotor. Should failure occur, the touchdown
bushing will be contacted by the shaft prior to the rotor contacting
the inner surface of the stator poles. This prevents damage to the
stator and the rotor. A polycarbonate cover will be mounted to the
rotor kit base and encompass the AMB assembly in order to prevent
user injury. If necessary, a small CPU cooling fan may also be
mounted to the cover to facilitate greater convection heat transfer.

Cal Poly Mechanical Engineering	Lab Section:	Assignment #	Title: CDR Concept		Drwn. By: Sean Fowler
ME 428 -Fall 2015	Dwg. #:	Nxt Asb:	Date: 2/11/16	Scale:1:2	Chkd. By: ME STAFF

Appendix M

Gantt Chart

ID	Task Mode	Task Name	Duration	Start	Finish
0		Mag Bearing Project	168 days?	Wed 10/28/15	Sat 6/11/16
1		ME 428	33 days	Wed 10/28/1	Fri 12/11/15
2		Working toward PDR	14 days	Wed 10/28/15	Mon 11/16/15
3		Turn in Gantt chart, sponsor feedback notes, concept	0 days	Fri 10/30/15	Fri 10/30/15
4		Magnetics analysis	14 days	Wed 10/28/15	Mon 11/16/15
5		PDR Report, Presentation	0 days	Mon 11/16/15	Mon 11/16/15
6		Working toward CDR (FALL)	19 days	Tue 11/17/15	Fri 12/11/15
7		Electronics Hardware Design			
8		End of Quarter Status Memo due	0 days	Mon 11/30/15	Mon 11/30/15
9		Winter Break	17 days	Sat 12/12/15	Sun 1/3/16
10		ME 429	56 days	Mon 1/4/16	Fri 3/18/16
11		Working toward CDR (WINTER)	22 days	Mon 1/4/16	Mon 2/1/16
12		Controls Design	21 days?	Mon 1/4/16	Sun 1/31/16
13		CDR report, presentation	0 days	Mon 2/1/16	Mon 2/1/16
14		Update plans and schedule based on sponsor feedback	1 day?	Tue 2/2/16	Tue 2/2/16
15		Working toward project update report to Dr. Wu	25 days	Tue 2/2/16	Mon 3/7/16
16		Manufacturing Plan	10 days?	Tue 2/2/16	Mon 2/15/16
17		Order Parts	3 days	Tue 2/16/16	Thu 2/18/16
18		Test Plan	5 days?	Fri 2/19/16	Thu 2/25/16
19		Turn in Project Update	0 days	Mon 3/7/16	Mon 3/7/16
20		Manufacturing and Test Review	0 days	Mon 3/7/16	Mon 3/7/16
21		Begin Manufacturing, Tests, systems Integration	10 days	Mon 3/7/16	Fri 3/18/16
22		Spring Break	7 days?	Sat 3/19/16	Sun 3/27/16
23		ME 430	55 days	Mon 3/28/16	Fri 6/10/16
24		Working toward Expo, Final Report	43 days	Mon 3/28/16	Wed 5/25/16
25		Mechanical/M Assembly	6 days?	Mon 3/28/16	Mon 4/4/16
26		Electronics integration	6 days?	Mon 4/4/16	Mon 4/11/16
27		Test1	6 days?	Mon 4/11/16	Mon 4/18/16
28		Troubleshoot	6 days?	Mon 4/18/16	Mon 4/25/16
29		Test2	6 days?	Mon 5/2/16	Mon 5/9/16
30		Design Expo	0 days	Wed 5/25/16	Wed 5/25/16
31		Design Report Due	0 days	Fri 5/27/16	Fri 5/27/16
32		Graduation	0 days	Sat 6/11/16	Sat 6/11/16

Project: Mag Bearing Project
Date: Mon 6/6/16

| Task | Milestone ◆ | Project Summary | Inactive Milestone | Manual Task | Manual Summary Rollup | Start-only | External Tasks | Deadline | Manual Progress |
| Split | Summary | Inactive Task | Inactive Summary | Duration-only | Manual Summary | Finish-only | External Milestone | Progress |